Advanced Materials '94

Edited by

M. Kamo

H. Kanda

Y. Matsui

T. Sekine

National Institute for Research in Inorganic Materials

Advanced Materials '94

Proceedings
of
The NIRIM International Symposium on
Advanced Materials '94
Tsukuba, Japan, March 13 – 17, 1994

Edited by

M. Kamo, H. Kanda, Y. Matsui and T. Sekine

National Institute for Research in Inorganic Materials

EXECUTIVE COMMITTEE

CONTENTS

COE Research Project in NIRIM

Shinobu Yamaoka

National Institute for Research in Inorganic Materials, Tsukuba, Japan

'COE' or 'Center of Excellence' Research Project began in 1993 under the auspices of Science and Technology Agency (STA) and NIRIM was selected as one of the first institutes to carry out the projects in the field of advanced materials using the extreme conditions of ultra high pressures and ultra high temperatures and advanced techniques of ultimate analysis. In order to promote the project, it has adopted such policies as invitation of excellent scientists from Japan and abroad to join the research, the Advisory Committee to assess the project, and the International Symposium to exchange the most recent information on advanced materials science.

1. Introduction

From FY 1993, 'COE' or 'Center of Excellence' Research Project began under the auspices of Science and Technology Agency (STA). The five year project aims to foster a national research institute to be a leading research institute composed of excellent researchers, research facilities and research support systems in order to generate challenging and interesting results in basic science. In FY 1993, NIRIM was selected as one of the initial COE organizations together with two other national institutes and aims to be a 'COE' in the research field of advanced materials using the extreme conditions of ultra high pressure and ultra high temperature and advanced techniques of ultimate analysis.

The three research fields of 'ultra high pressure', 'ultra high temperature' and 'ultimate analysis', which NIRIM has been actively engaged in for many years, were designated as COE research fields, and synthesis of high pressure materials are carried out by using ultra high pressure techniques, diamond and cBN films of highly functional properties are developed by vapor deposition methods under ultra high temperature plasma conditions, and analyses of structure and composition in an ultra small area down to nanometer scale are carried

out in the project.

In order to promote the project, it has adopted such policies as invitation of excellent scientists from Japan and abroad to join the research, the Advisory Committee to assess the project, and the International Symposium to exchange the most recent information on advanced materials science.

2. Research in the Field of 'Ultra High Pressure'

New denser materials are expected to be discovered at ultra high pressures because new and strong chemical bonds can be formed by decreasing atom-atom distances in a compound. Then, 'ultra high pressure' is an interesting research field of materials science. However, at present only diamond and cBN are used for practical applications among many compounds synthesized at very and ultra high pressures. One of the reasons is that the present advanced high pressure techniques are utilized mainly in the fields of earth science and solid-state physics but little in material science.

In the project, materials research is to be carried out over a wide pressure and temperature range with the following three themes.

(1) Development of ultra high pressure techniques
By introducing a diamond anvil cell with laser heating system or DAC/laser, the techniques to generate ultra high pressure of sub-tera Pascal (TPa) region and high temperature of several thousand degrees Celsius are developed. Besides, two types of shock compression apparatus, one is a two-stage light gas gun and the other is a laser-driven shock wave generator, are introduced to carry out synthesis experiments under shock compression of sub-TPa to TPa region.

(2) Search for new denser substances
By using the high pressure techniques mentioned above, unkown substances are searched widely in the various systems of elements, oxides, sulfides, nitrides, carbides, borides, etc. Because of limited amounts of samples obtained in a DAC/laser system and very fine grains obtained by shock apparatus, advanced analytical techniques must be developed to identify and characterize them. In this context, intimate relation with the research field of 'advanced techniques of ultimate analysis' is indispensable.

(3) Synthesis of materials for practical use

Synthesis research is carried out for practical applications of newly discovered substances in the research (2). At the same time, already-known high pressure substances such as diamond and cBN are investigated to improve their properties and functions as useful materials. For this purpose, a belt type high pressure apparatus with a large volume is developed to generate pressures of 20 GPa region.

3. Research in the Field of 'Ultra High Temperature'

In the research field of ultra high temperature, ultra high temperature techniques are developed to generate highly active plasmas and excited beams in order to synthesize "Super Diamond", which means high quality cBN film and single crystalline diamond film.

The program in this field is mainly supported by "Super Diamond" project, which is also five year project running parallel to the COE project. Because the detail of "Super Diamond" project is described elsewhere in this proceedings, the outline is briefly given below.

The research is carried out by developing the following two techniques. One is the development of ultra high temperature generation techniques, where various processing plasmas at pressures lower than 1 atm. are developed by using direct current, radio frequency and microwave discharge.

The other is the development of film fabrication techniques. This techniques is indispensable because high quality films must be fabricated in order to utilize the excellent properties of "Super Diamond". So, film fabrication techniques such as laser-assisted plasma CVD, ion beams, and radical beam epitaxy are developed.

4. Research in the Field of 'Ultimate Analysis'

In the research field of 'ultimate analysis', analytical techniques are developed to analyse the structure, composition, and bonding nature in the nano-scale regions of the surfaces, interfaces and grain boundaries of the advanced materials using the advanced beam techniques of electron and ion beams.

Ultimate analytical techniques are composed of three parts. One is development of local structure analytical techniques, where observation techniques are developed to dynamically view the local structure directly to identify various deficiencies in the advanced materials. Image processing techniques are introduced using an ultra-high voltage electron microscope with the highest resolution.

Another is the development of local composition analytical techniques, where analytical techniques are developed to investigate the local compositions of grain boundaries and interfaces of the advanced materials with high sensitivity and accuracy using an analytical electron microscope and a secondary ion mass spectroscope with the highest sensitivity.

The other is the development of advanced techniques of surface analysis, where surface analytical techniques are developed to enable highly accurate analysis of the atomic structure, lattice vibration and electron states of surfaces of the advanced materials using an ion scattering spectrometer and a high resolution electron energy loss spectrometer.

5. Management and support systems

To promote the COE program, the following research management and support systems are adopted.

The project is open to outside researchers. The project has such systems as long-term outside researchers from Japan and abroad, short-term overseas researchers, and visiting research staffs from domestic national institutes and universities, so that distinguished outside researchers can participate in the project.

In order to assess and advise the COE project, the Advisory Committee is established. The Advisory Committee is composed of outstanding domestic and overseas researchers. And also in order to disseminate the research accomplishments and exchange recent information, NIRIM International Symposium on the Advanced Materials is held every year.

Electron Holography and Its Applications to Observing Microscopic Structures and Flux Lines

Akira Tonomura

Advanced Research Laboratory, Hitachi, Ltd., Tonomura Electron Wavefront Project, ERATO, JRDC, Hatoyama, Saitama 350-03, Japan

ABSTRACT

Phase distribution in an electron wavefunction can be precisely measured to within 1/100th of the electron wavelength using both electron holography and a "coherent" field-emission electron beam. This technique allows for the ultra-fine measurement of material structures and electromagnetic field distributions on a microscopic scale. Flux lines in a superconducting thin film can be observed quantitatively by electron-holographic interference microscopy and dynamically by Lorentz microscopy.

INTRODUCTION

Electron beam intensity can be used to observe specimens in electron microscopy. The phase distribution of an electron beam can also be observed thanks to the development of the coherent field-emission electron beam [1]; Electron interference patterns can be directly observed on a fluorescent screen with the naked eye. Before this, interference patterns could only be recorded on film with conventional electron microscopes requiring a long exposure time. In addition, electron phases can be measured within an accuracy of 1/100th of a wavelength using electron holography[2]. Because of these developments, the structure of materials at atomic scales and the microscopic distributions of electromagnetic fields can be observed by precisely measuring phase distribution[3]. This paper introduces progressive work in electron interference experiments using electron holography.

ELECTRON HOLOGRAPHY

In the first step of holography, an interference pattern is formed between an object wave and a reference wave in a field-emission electron microscope, and recorded on film as a hologram. This hologram is subsequently illuminated by a collimated laser beam and an exact image is produced three-dimensionally in a diffracted beam. An additional image called a "conjugate image" is also produced in holography with the same amplitude in magnitude, but with the opposite sign.

An interference micrograph, or contour map of the wavefront, can be obtained by simply overlapping an optical plane wave with this reconstructed wave. If a conjugate image instead of a plane wave overlaps this wavefront, the phase difference becomes twice as large, as if the phase distribution were amplified two times. By repeating this technique, phase shifts can be detected as small as 1/100 of a wavelength. This phase-amplified interference electron microscopy provides information about the microscopic distribution of electromagnetic fields.

Optical reconstruction using a laser light is simple, but is off-line as a result of the time consumed in developing film. Therefore, on-line reconstruction techniques are being developed using computers and optical devices. An image can be numerically reconstructed from a hologram recorded on a charge-coupled device (CCD) attached to an electron microscpe. By doing this, an amplitude image, phase image, and interference image can be displayed. These images can be obtained in a fairly short time, depending on the performance of the computer used, but not yet in real-time.

A real-time method using a liquid crystal panel as a phase hologram has been developed[4];

The image signal of the hologram detected with a TV camera attached to the electron microscope is transferred to the liquid-crystal panel, where the intensity distribution is transformed into a phase shifting function for an illuminating light beam. The time resolution of 1/30 s is determined by the TV system. Dynamic phenomena therefore can be observed in real-time with this method.

APPLICATIONS

When a parallel electron beam is incident to electromagnetic fields, the electron beam is deflected, or phase shifted. The phase shift $\Delta S / \hbar$ is calculated from the Schrödinger equation as,

$$\Delta S / \hbar = (1 / \hbar) \oint (m\nu - eA) \cdot ds$$
$$= (1 / \hbar) \oint (\sqrt{2meV} - et \cdot A) ds, \tag{1}$$

where the integral is carried out along the route connecting two electron trajectories and t is the unit tangent vector of the electron trajectory. This equation shows that electromagnetic potentials (A, V) can be detected by measuring the phase shift in an electron beam, although what we detect is not the electromagnetic potentials themselves but their integrals along the electron beam trajectory.

(1) Specimen Thickness Distribution in Atomic Dimensions

An interference micrograph for a cleaved molybdenite thin film[2] amplified 24 times is shown in Fig. 1. The phase distribution here is displayed as deviations from regular fringes, i.e., an interferogram. Steps A, B, and C in the micrograph correspond to one, three, and five layers of atomic surface steps. The thickness change at step A is only 6.2 Å (one-half of the c-axis spacing), and produces a phase shift of $2\pi/50$.

In the transmission mode, surface topography can only be investigated by measuring thickness. In the reflection mode, thickness can be measured with a high degree of sensitivity because surface height differences are directly measured in units of extremely short electron wavelengths as geometrical path differences[5].
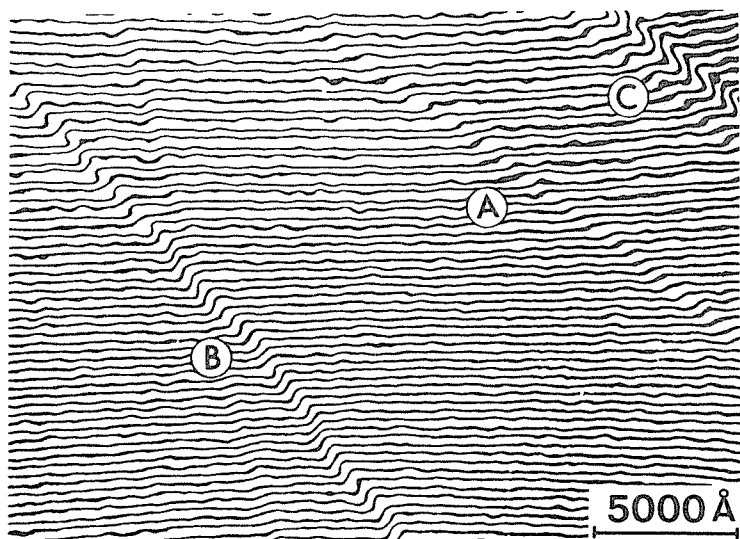
Fig. 1. Interference micrograph of molybdenite film (×24).

(2) Magnetic Field Observation

For a pure magnetic object, the phase difference between two electron beams passing through it is given by

$$\Delta S / \hbar = -(e / \hbar) \oint A \cdot ds = -(e / \hbar) \int B \cdot dS, \qquad (2)$$

where the first integral is carried out along a closed path along two electron trajectories, and the second integral is carried out over the surface determined by the two paths.

The following conclusions can be made from this equation[6].

(1) Contour fringes in the interference micrograph indicate magnetic
   lines of force, because the phase difference $\Delta S / \hbar$ vanishes   between
   two beams passing through arbitrary points along a magnetic line.
(2) A magnetic flux for h/e flows between adjacent two contour fringes.

An example of this is shown in Fig. 2. The specimen used here is a fine cobalt particle. When observed with an electron microscope which displays the intensity of the transmitted

electron beam, only a triangular outline can be seen. In this interference micrograph, however, two kinds of fringes appear. The fringes parallel to the three edges indicate that thickness increases linearly from the edges to 550 Å, and the fringes in the inner region where the thickness is uniform indicate the magnetic lines of force. Smoothly rotating magnetization can be observed at a glance even in such a fine particle.

The diameter of this particle is around 3000 Å. For smaller particles, magnetization is not closed inside, and the particle is uniformly magnetized. An example of a barium-ferrite particle[7] is shown in Fig. 3. Here, magnetic fields leak from the upper south pole of the particle and are then sucked up at the south pole. The particle therefore can be seen to have a single magnetic domain.

(3) Flux Lines in Superconductors

Flux lines in superconductors can be observed quantitatively by interference microscopy[8,9] and Lorentz microscopy[10] with our 350 kV holography electron microscope[11]. In the experiments we conducted, a superconductive thin film was tilted with respect to both the electron beam and the magnetic field.
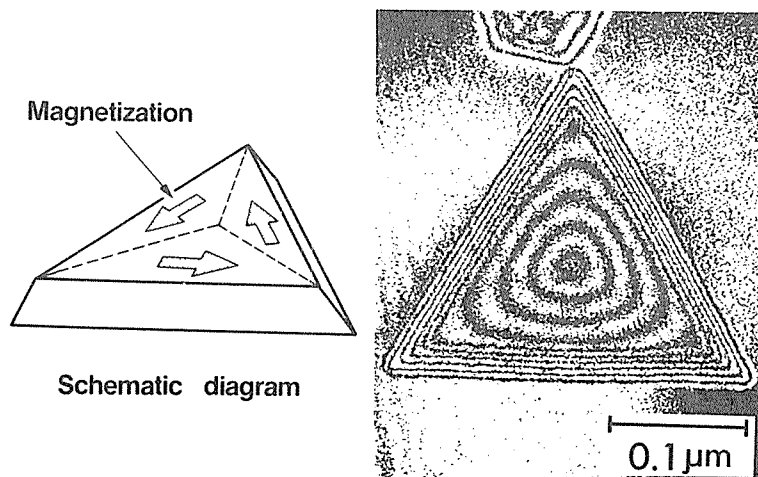
Fig. 2. Interference micrograph of Co particle.
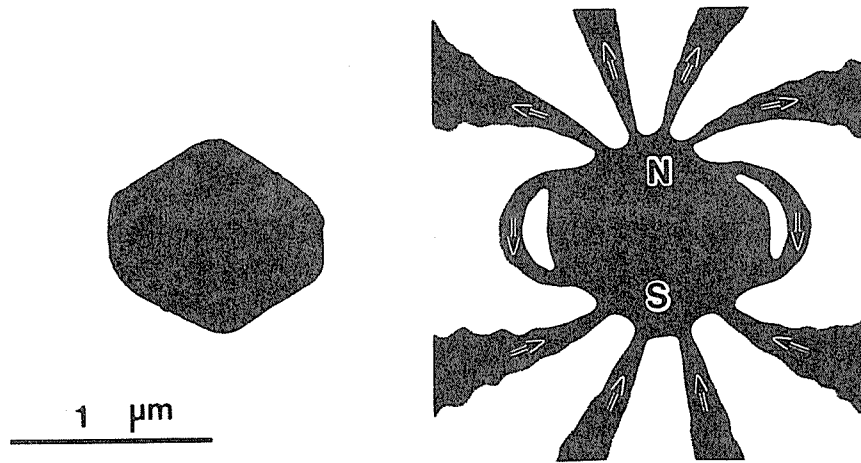
Fig. 3. Interference micrograph of barium-ferrite particle.

The experimental arrangement is shown in Fig. 4. A Nb thin film, set on a low-temperature stage, was tilted 45° to an incident beam of 300-kV electrons so that the electrons could be influenced by the flux-line magnetic fields. An external magnetic field of up to 150 gauss was applied horizontally. An example of a flux-line array in a single-crystalline Nb thin film[8] is shown in Fig. 5. In this interference micrograph, projected magnetic lines of force can be observed. They become dense in the localized regions indicated by circles in the photograph, which correspond to individual flux lines.

Although interference microscopy is highly resolved and quantitative, Lorentz microscopy is more convenient for observing the dynamic behavior of flux lines. In this experiment, the sample was first cooled down to 4.5K and the magnetic field B was gradually increased. As it increased, flux lines suddenly began to penetrate the film at $B = 32$ gauss, and the number increased as B was increased further. Their dynamic behavior was quite interesting. At first, only a few flux lines appeared here and there in a 15×10-μm^2 field of view. They oscillated around their own pinning centers and occasionally hopped from one center to another. These movements continued for as long as the flux lines were not closely packed ($B \leq 100$ gauss).
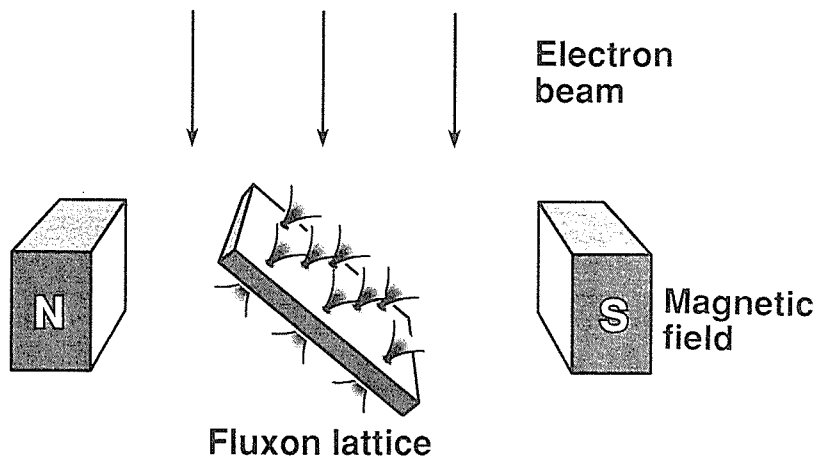
Fig.4. Schematic diagram for flux-line lattice observation.
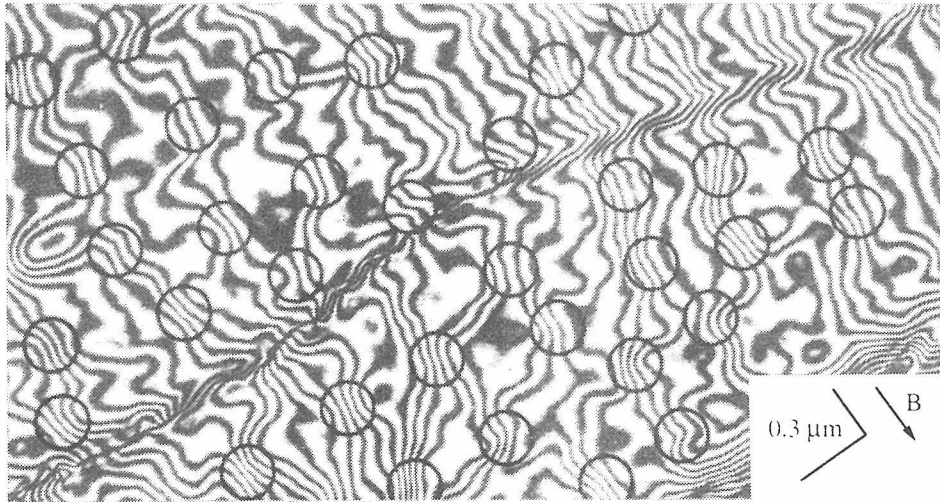
Fig. 5. Interference micrograph of a superconducting Nb film at
$B = 100$ gauss (Phase amplification ×16).

An equilibrium Lorentz micrograph at $B = 100$ gauss[10] is shown in Fig. 6. The film has a fairly uniform thickness in the region shown, but is bent along the black curves, called bend contours, caused by Bragg reflections at the atomic plane brought to a favorable angle by bending. Each spot showing a black and white contrast is an image of a single flux line. This contrast reversed, as expected, when the applied magnetic field was reversed. The tilt direction of the sample can be read from the line dividing the black and white parts of the spots. Because the black part is on the same side of all the spots, the polarities of all the flux lines seen in the region are the same. At a low B, i.e., up to 30 - 50 gauss, the flux lines are too sparse to form a lattice, even in equilibrium. At $B = 100$ gauss, the flux-line density is so high that they cannot form anything but a hexagonal lattice.
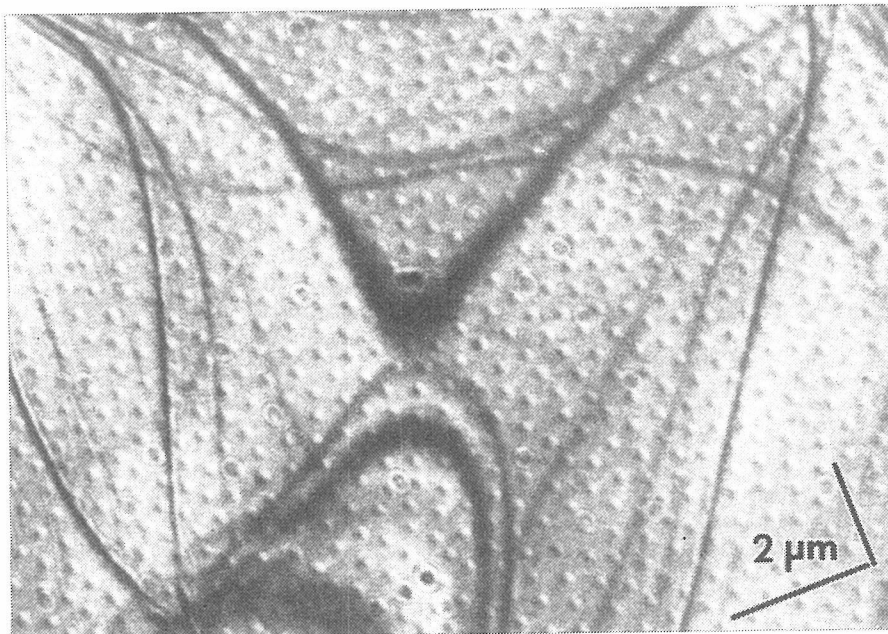
Fig. 6. Lorentz micrograph of a two-diamentional array
of flux lines in a superconducting Nb film.

A high-T_C superconductor has been investigated by means of Lorentz microscopy[12]. High-T_C superconductors are difficult to use practically, bacause the critical current vanishes at high temperatures and high magnetic-field regime even when the temperature is well below the critical temperature T_C. This phenomenon most probably arises from the behavior of flux lines but has not yet been proven concretely. Some researches believe that these flux lines melt like molecules in a liquid, and, as a result it is difficult to fix flux lines at some pinning sites[13]. Evidence for flux-line melting was provided by a Bitter BSCCO figure in which the flux-line image was blurred even at 15 K and 20 gauss (T_C = 85 K) [14]. Accordingly, the practical use temperature would not be T_C but rather the melting temperature T_m. Others, however, disagree with this, and attribute this phenomenon to weak pinning effects.

The flux lines were dynamically observed to test whether flux lines begin to move under such conditions. The observation was made under a fixed magnetic field B increasing the sample temperature from 4.5K to above T_C. A Lorentz micrograph at T = 4.5K and B = 20 gauss is shown in Fig. 7 (a). Flux lines are distributed at random. When the temperature was raised stepwise by a few K, flux lines moved. After a few minutes, flux lines arrived at an equilibrium state and became still. They did not melt even at 20K. The flux-line configuration changed between 40K to 50K. Flux lines form a regular lattice (c) above this transition region. The flux-line lattice persisted at higher temperatures though the image contrast gradually decreases and then disappears above 77K.
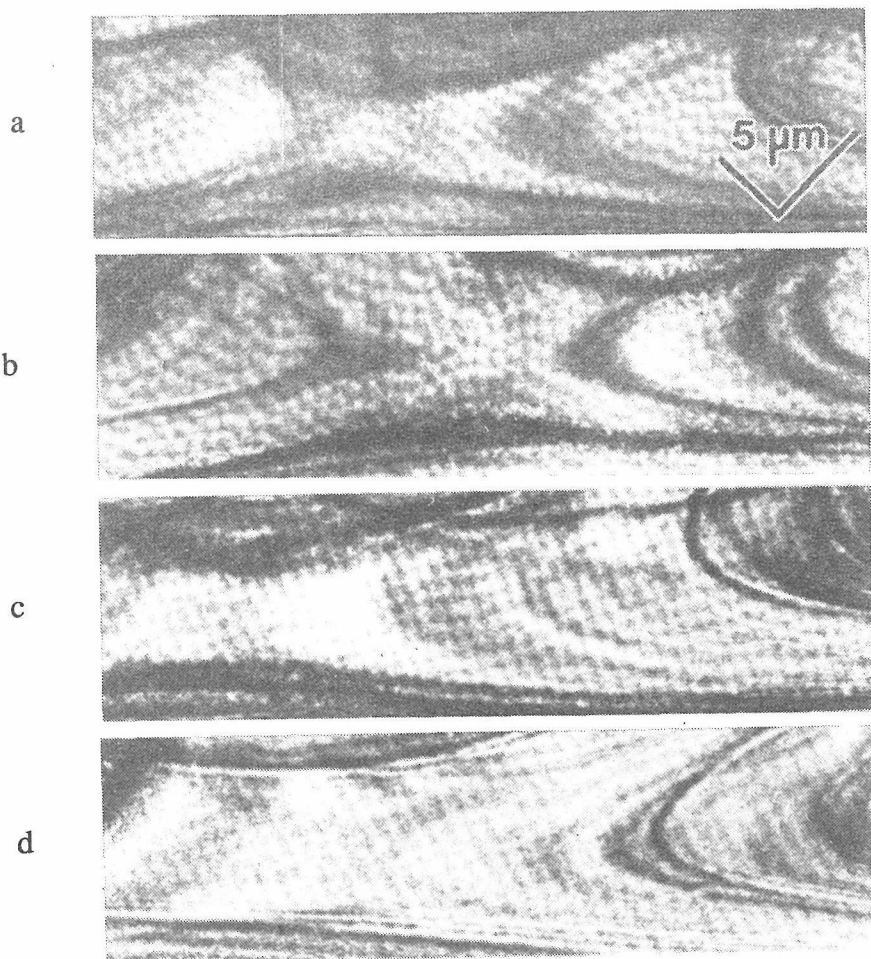
Fig. 7. Lorentz micrograph of a BSCCO (2212) film;
(a) T = 4.5 K, (b) T = 20 K, (c) T = 56 K. and
(d) T = 68 K.

CONCLUSION

The performance of electron interferometry has been improved thanks to the development of a coherent electron beam and electron holography: Phase distribution in an electron beam can be measured to within $2\pi/100$, and has opened a way to measure microscopic objects and fields with ultra-high precision. These developments allow for the direct observation of individual flux lines in a superconductor. Electron interferometry can be used to clarify the fundamental and practical applications of superconductivity, especially in the field of high-T_C superconductors.

REFERENCES

[1]   A. Tonomura et al., *J. Electron Microsc.* 28 1 (1979).
[2]   A. Tonomura et al., *Phys. Rev. Lett.* 54 60 (1985).
[3]   A. Tonomura, *Electron Holography*, (Springer Verlag, Heidelberg, 1993).
[4]   J. Chen et al., *Optics Letters* 18 1887 (1993).
[5]   N. Osakabe et al., *Phys. Rev. Lett.* 62 2969 (1989).
[6]   A. Tonomura et al., *Jpn. J. Appl. Phys.* 19 97 (1980).
[7]   T. Hirayama et al., *Appl. Phys. Lett.* 63 418 (1993).
[8]   J. Bonevich et al., *Phys. Rev. Lett.* 70 2952 (1993).
[9]   J. Bonevich et al., *Phys Rev.* B49 (1994).
[10] K. Harada et al., *Nature* 360 51 (1993).
[11] T. Kawasaki et al., *Jpn. J. Appl. Phys.* 29 508 (1990).
[12] K. Harada et al., *Phys. Rev. Lett.* 71 (1993) 3371.
[13] For example, see D. J. Bishop et al., *Science* 255 (1992) 165.
[14] R. N. Kleiman et al., *Phys. Rev. Lett.* 62 (1989) 2331.

Scanning Transmission Electron Microscopy and Its Applications to Diamond and Related Materials

L.M. Brown

Cavendish Laboratory, Madingley Rd., Cambridge, CB3 0HE, U.K.

ABSTRACT: STEM has proved to be efficacious in the analysis of various forms of carbon, because the electron energy-loss spectrum shows features which distinguish them. The fraction of sp^3 bonding can be estimated in diamond-like carbons, and correlated with growth conditions. In the case of diamond thin films, produced by CVD, amorphous layers at grain boundaries and surfaces can be observed, which helps explain some properties of the films. In natural type I diamonds, the location and chemical state of the nitrogen can be assessed.

INTRODUCTION: As demonstrated by Batson [1] and Muller et. al. [2] it is now possible to observe fine structure in electron energy loss spectra associated with structures less than 1nm in extent. It seems highly likely that the most immediate application of such techniques is to the nucleation, growth and structure of thin films, and to the chemistry of interfaces, particularly grain boundaries in metals.[3] The development of the instrumentation which permits such investigations owes much to many groups worldwide, starting with Crewe's original vision of an analytical microscope based on the field emission gun, and including the recent development by McMullan of efficient parallel detectors for electron spectrometers based on charge-coupled devices[4].

APPLICATION TO CARBON THIN FILMS: The distinction between various forms of carbon is clearly revealed in the corresponding electron energy-loss spectrum, as demonstrated in Fig. 1.[5]
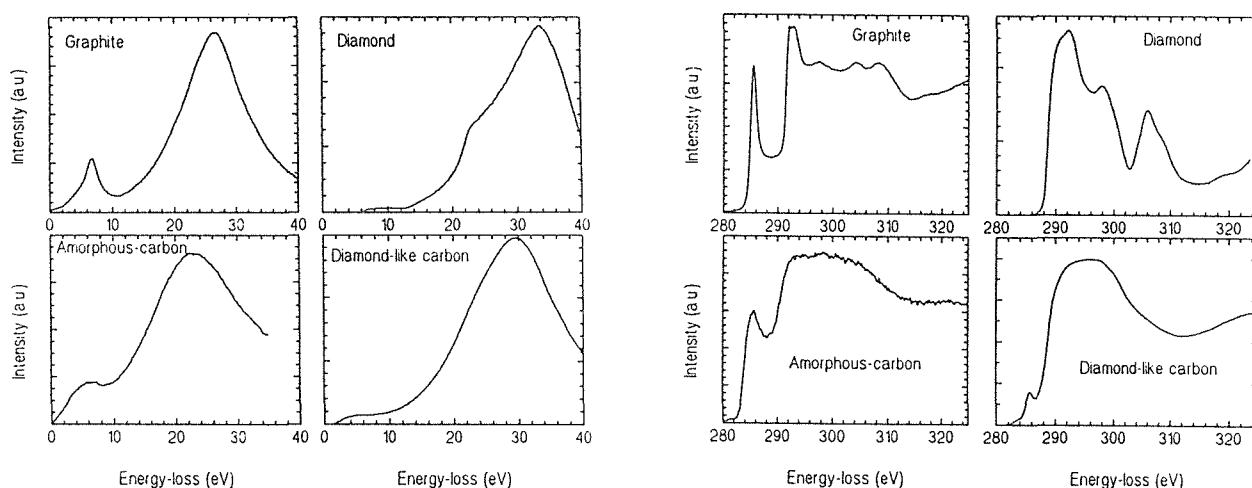
Fig. 1: Spectra for various forms of carbon, reproduced from Fallon[5] with kind permission. The low-loss spectra are on the left, the K-edge spectra on the right. The zero-loss peak has been removed, background has been subtracted, and the spectra have been deconvoluted to remove multiple scattering.

Key features in the low-loss spectra are the band gap, present for diamond and diamond-like carbon, but notably absent for graphite and amorphous carbon; and the energy corresponding to the main plasmon excitation, which increases systematically as the density increases from amorphous carbon through graphite and diamond-like carbon to crystalline diamond. The main plasmon excitation is assumed to be due to the four valence electrons whatever the nature of the bonding, and its energy is to a good approximation proportional to the square root of the density of these. In the carbon K-edge, we see a sharp line with a rising edge at about 285V loss, corresponding to excitation of the bound $1s^2$ electrons into π^* antibonding states; in diamond, however, there are no such states and the edge rises at about 289V due to excitation into the p-projected density of empty states in the tetrahedrally co-ordinated crystal. The K-edge permits a quantitative estimate of the degree of tetrahedral bonding as first proposed by Berger et. al.[6] and shown schematically in Fig. 2.
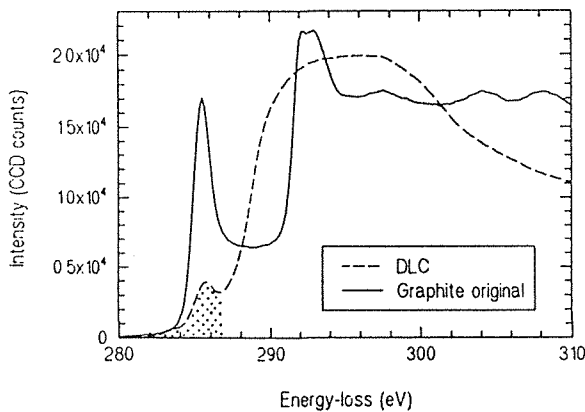
Fig.2. Comparison of the K-edge structure from graphite and diamond like carbon with 80% sp^3 bonding. The ratio of the shaded area to the total area, in this case between 280V and 300V,is the fraction of sp^2 bonding, x, and the fraction of sp^3 bonding is assumed to be 1 - x.

Using this method, Fallon[5,7] was able to produce a calibration curve for various carbons, shown in Fig. 3. This curve correlates the density as measured by the plasmon energy with the degree of sp^3 bonding as measured from the K-edge. What is noteworthy is diamond-like carbons can be fitted to a straight line, which ranges from some amorphous carbons which show only a small but significant proportion of sp^3 bonding through to diamond itself which is a calibration point at 100% sp^3 bonding. Various forms of carbon do not fall on this 'main sequence', especially crystalline graphite and the fullerenes, which show a higher density, and carbon containing some hydrogen, which shows a lower density: both these results can be rationalised in terms of the "frustration" of the perfect graphite structure which must increase the density to produce amorphous carbon, and the promotion of sp^3 bonding by hydrogen without an accompanying reduction in density.

Considerable care has gone into this curve. The graphite data derives from spectra taken with the beam perpendicular to the c-axis; theoretical caculations show that randomly oriented graphite should produce a point in the neighbourhood of 'defect graphite'. The hydrogenated carbon is a holey carbon film supplied for use in the electron microscope; the presence of hydrogen is inferred from the shape of the K-edge. The diamond-like carbons come from a variety of sources, but they are made by depositing onto a silicon substrate filtered ions from a carbon arc; the main variables in their production are the substrate bias potential and the arrangement and strength of the filtering fields. All spectra have been deconvoluted to remove multiple scattering effects before the analysis has been carried out; when this is done, the estimated bonding character is independent of the width of the energy window used to analyse the spectra. Further details can be found in Fallon's thesis[5]. A previous study by Cuomo et. al.[8] on diamond-like carbons produced by laser ablation shows the same correlation. Attempts to determine the proportion of sp^3 bonding from the low loss spectra, using an analysis based on application of the sum rule to the imaginary part of the dielectric function, as pioneered by Fink et. al.[9] seems to give less robust results, probably

because of difficulty in separating the contributions from the different families of electrons [5,8].
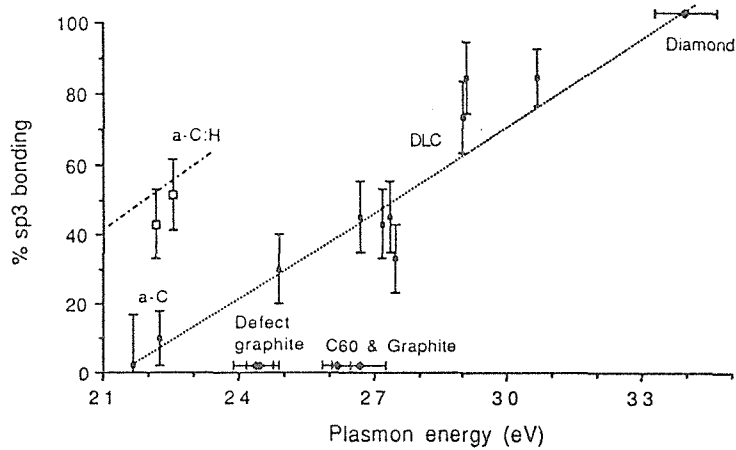
Fig. 3. Percent sp³ bonding as a function of the main plasmon energy, taken as the position of the large peak in the low loss spectra. Diamond and the diamond-like carbons form a sequence, from which other graphites and hydrogen-containing carbons depart. Reproduced from Fallon[5] with kind permission.

Independent assessment[10] of the highly tetrahedral DLC films has been carried out by neutron diffraction, and results in a very similar estimate of the degree of sp³ bonding, about 86% compared with the EELS result of 84%, subject to an uncertainty of about 5%. Thus one feels considerable confidence in the characterisation of these films by EELS.

A striking application of EELS to these problems has been the correlation established between the state of bonding in the DLC film and the bias voltage V applied to the substrate and the growing film.
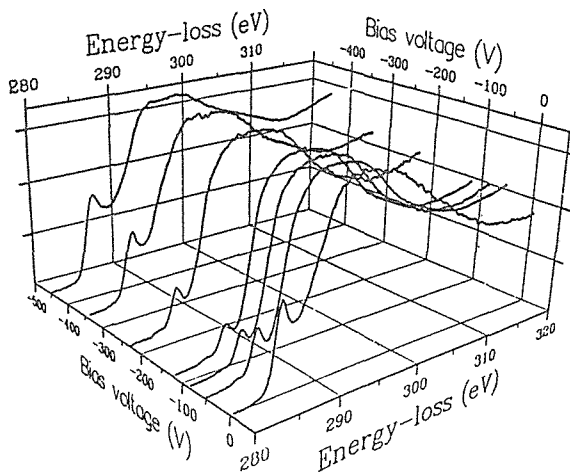
Fig.4. The carbon K-edge for DLC films deposited at various bias voltages. Reproduced by kind permission of the authors[11].

Fig.4. shows a series of carbon K-edges observed by Fallon et. al. for a range of bias voltages[11] from which it is clear that the fraction of sp³ bonding achieves a maximum value at about -140V, implying that the positive carbon ions from the arc require a certain kinetic energy to promote diamond-like bonding. Several other properties of the films such as resistivity and Young modulus also show a maximum at the same bias. This behaviour can be understood in terms of a 'subplantation' model, in which the diamond-like bonding is promoted by the high compressive stress created by an ion

- 14 -

which buries itself in a displacement spike just below the surface of the film; however, if the energy of the ion is too great, the local temperature rise is sufficient to allow local 'graphitisation' and destruction of the sp^3 bonding. These ideas have been promoted and extensively reviewed by Robertson[12]; they take for their starting point the thermodynamic equilibrium between diamond and graphite which forms the basis for understanding the production of natural and synthetic diamond at high pressures and temperatures, so no processes unique to the thin film growth environment are postulated.

A further application is to thin films of CVD diamond, which normally consist of grains which are separately nucleated, often multiply-twinned, crystals. Grain boundaries in such films are formed where the crystals impinge on one another during the growth process. In the grain boundary region, and over all the surfaces of such films, EELS reveals the presence of a thin non-diamond layer. Analysis[7] of the spectra results in a point on the calibration curve of Fig. 3 shown by the large filled circle at the lower left of the main sequence; it suggests that the film is amorphous carbon, not hydrogenated.
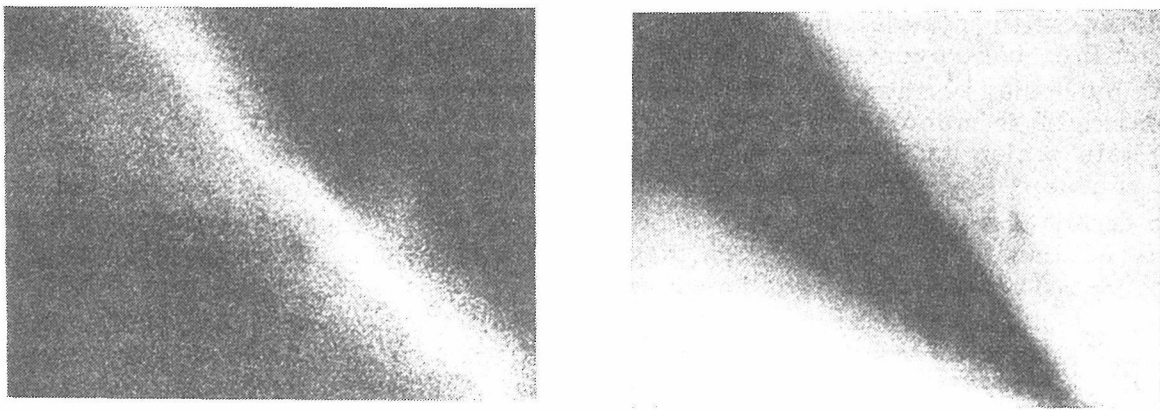
Fig.5. Energy filtered images of an intergranular region in CVD diamond. On the left, a window at 6V reveals a graphite-like carbon, whereas on the right a window at 34V reveals diamond. Width of each image: 50nm. Width of energy window: 2V. Reproduced from Fallon[5] by kind permission.

Fig.5. shows part of a series of energy-filtered images in the grain boundary region; most telling is the image at 6V loss, within the band-gap of diamond, but at the first peak of the amorphous carbon spectrum (Fig. 1). Such intensity cannot result from a diamond surface plasmon because the imaginary part of the dielectric function is zero, or very nearly zero, over the energy window used for the image.

An important question concerns the spatial resolution expected for such filtered images. A simple estimate based on the impact parameter is presented by Pennycook[13]: for losses around 6V and 10mr collection angles into the spectrometer, the spatial resolution should be about 6nm; but for a loss of 200V, 0.2nm is expected. Thus the thickness of the amorphous grain boundary layer cannot be estimated readily from images such as those in Fig. 5. Images using transmission electron microscopy suggest that such layers are very thin, perhaps 0.5nm in width.

Thus to achieve subnanometer resolution, losses at high energies must be utilised, and the recent work quoted earlier by Muller et. al.[2] reveals a complex interface between the silicon substrate and the CVD diamond; the layer on which the diamond grows is an amorphous carbon with characteristics similar to the grain boundary layers just described. This interfacial layer however is not present with a 250V negative bias - just as might be expected on the basis of a subplantation model. Also detected are an amorphous silica layer, and an amorphous silicon carbide layer, the latter only 3nm

thick. Although commercially available CVD diamond films are very perfect, they fall short of the perfection of single crystal diamond, in that they show a somewhat lower elastic modulus, somewhat higher ultraviolet absorption, and somewhat small thermal conductivity. It is possible that small amounts of amorphous carbon incorporated into boundaries cause these effects, and the possibility seems to exist to eliminate or at least control such intergranular layers.

The achievement of subnanometer resolution in analytical electron microscopy requires high stability both of the beam position and current, as well as the spectrometer, because long acquisition times are required, of the order of 1s per pixel of size 0.5nm. Muller et. al.[2] suggest that further improvements can be obtained by stabilising the beam with reference to annular dark field images of atomic columns. There seems little doubt that the immediate future will see a high level of activity in this area.

APPLICATION TO NATURAL DIAMOND: In natural diamond, EELS has mainly been used to analyse nitrogen. Nearly all diamonds contain small amounts of nitrogen, which is associated with platelet precipitates on cube planes. Until recently, there was considerable controversy concerning the composition of the platelets, but recent results by Bruley[13] show that the platelets themselves contain very little nitrogen, only a fraction of a monolayer: they certainly are not to be thought of as a 'nitrogen precipitate' which has been modelled as two monolayers. The nitrogen K-edge, with an onset at about 406V, shows fine structure which looks rather like an indistinct version of the carbon K-edge. These results have recently been confirmed[14] and extended for a variety of diamonds, none of which display more than half a monolayer of nitrogen in the platelet. The fine structure is shown in Fig. 6.
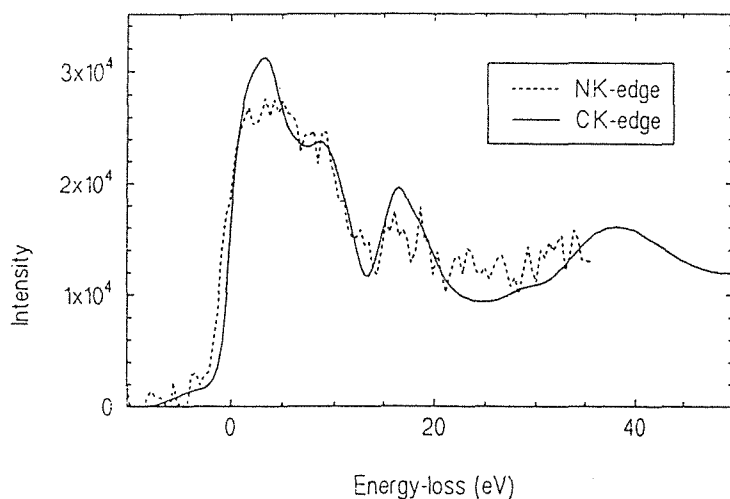
Fig.6. Structure after the nitrogen K edge (dotted line) compared with that after the diamond K-edge (full line).

When the nitrogen edge - very noisy, because the signal comes from only 50 nitrogen atoms - is compared with the carbon edge, it can be seen to have a similar shape, which suggests that the local environment around the nitrogen is similar to that around carbon in the diamond lattice. Calculations of the fine structure by Brydson et. al.[15] using multiple scattering theory show that the fine structure can be accounted for by single substitutional nitrogen, in which the local environment is distorted by the presence of a double bond, which destroys the tetrahedral symmetry and introduces local strain, causing the fine structure to be blurred. It has even proved possible to estimate the magnitude of the strain giving acceptable agreement with experiment, thus relating the structure of the nitrogen environment to a long line of more traditional experiments and theories based on the optical properties of nitrogen in diamond.

REFERENCES:
1. Batson, P. E., Nature 366, 727-728, 1993.
2. Muller, D. A., Tzou, Y., Raj, R., and Silcox, J., Nature 366, 725-727.
3. Brown, L. M., Nature 366, 721, 1993.
4. For recent technical details and references, see McMullan D., Fallon, P.J., Ito, Y., and McGibbon A.J., Electron Microscopy 92 (Eurem), Vol. 1, 103-104, Eds. A. Rios et. al., Universidad de Granada, Granada 1992.
5. Fallon, P. J., 1992, Thesis, University of Cambridge.
6. Berger, S. D., McKenzie, D. R., and Martin, P. J., Phil. Mag. Lett., 57, pp 95-128, 1988.
7. Fallon, P.J., and Brown, L.M., Diamond and Related Materials, 2, pp1004-1011, 1993.
8. Cuomo, J. J., Doyle, J. P., Bruley, J., and Liu J.C., Appl. Phys. Lett. 58 (5) pp 466-468, 1991.
9. Fink, J., Muller-Heinzerling T., Pfluger J., Bubenzer A., Koidl P., and Crecelius G., Solid State Communications 47 pp 687-691, 1983. See also the review article by Fink, J., Adv. in Electronics & Electron Physics, 75, pp121-232, 1989.
10. Gaskell, P. H., Saeed, A., Chieux, P., and McKenzie D. R., Phil. Mag. B, 66, pp155-169.
11. Fallon, P. J., Veerasamy, V. S., Davis, C. A., Robertson, J., Amaratunga, G. A. J., and Milne, W. I., Phys. Rev. B 48, pp4777-4782, 1993.
12. Robertson, J., Phil Trans R. Soc. Lond. A 342, pp277-286, 1993.
13. Bruley, J., Phil. Mag. Lett., 66, pp47-66, 1992.
14. Fallon, P. J., Brown, L. M., Barry, J. C., and Bruley, J., to be published.
15. Brydson, R., Brown, L. M., and Bruley, J., to be published.

Structural Characterization of High Tc Superconductors and Fullerene Related Materials by HREM.

G. Van Tendeloo, J. Van Landuyt and S. Amelinckx

EMAT, University of Antwerp (RUCA), Groenenborgerlaan 171, B-2020 Antwerp, Belgium

Abstract

We are presenting here a HREM analysis of two families of newly developed materials. First we deal with the Hg-based superconducting compounds which under pressure, show superconducting transition temperatures as high as 160K. Hg-compounds synthesized under ambiant pressure are also discussed. Rb_xC_{60}, unstable in air, has been studied for the first time by electron microscopy. A characterization by imaging and diffraction of helicoidal carbon nanotubesn grown under appropriate conditions is also reported.

Superconducting Hg-compounds

Several higher order members of the Hg-based superconducting family $HgBa_2Ca_{n-1}Cu_nO_{2n+2+\delta}$ have been synthesized. The critical temperature of these materials is known to increase from 94K for the n = 1 compound, to a maximum Tc of 133.5K for the n = 3 member; for larger n values Tc is decreasing [1]. Very recently it was shown that Tc increases steadily with pressure at a rate of more or less 1K/GPa, reaching Tc values as high as 164K and 155K for the Hg-1223 compound [2,3]. This strong pressure effect suggests that by the appropriate chemical doping, which would introduce a chemical pressure, Tc values of the order of 150K are possible at normal -external- pressure. Several substitutions in the Hg-plane as well as at the Ba- or the Ca-positions have been successfully synthesized; they have led to a series of new Hg-based superconducting compounds, which can be prepared under ambient pressure and which have a Tc up to 110K [4-8].

The structure of all members is similar; they contain rock salt like slabs $[(BaO)(HgO_\delta)(BaO)]$, alternating with perovskite slabs of the type $[(CuO_2)(Ca)]_{n-1}(CuO_2)$. The structure for the n =1, n = 2 and n = 3 compound is represented in fig. 1; for higher n-values an extra $[(CuO_2)(Ca)]$ slab is inserted, leaving the rest of the average structure unaltered. Samples corresponding to the nominal stoichiometry $HgBa_2Ca_{n-1}Cu_nO_{2n+2+\delta}$ as well as the derived structures were prepared according to details available in the literature[1,4-8].

Electron diffraction along several reciprocal zone axes confirm the P4/mmm symmetry for all n-values ranging from 2 to 7. [100] high resolution images for different members of the family are in agreement with the proposed structure of fig.1. The most common defect encountered, particularly for higher order members of the family, is the intergrowth of different n-members; such defects have been observed in a large number of homologous series, e.g. in the Bi- or Tl- superconducting series. Occasionally regular intergrowths of different n-members of the family over fairly large distances (several hundred Ångstrom) have been found [9].

A remarkable defect is shown in fig.2. Locally at the position indicated, we have four rocksalt layers rather than the usual sequence of three layers $[(BaO)(HgO_\delta)(BaO)]$. A single HgO_δ-layer is replaced by a double HgO_δ-layer. Neutron diffraction refinements of the different Hg-members show that the largest occupation factors for those oxygen atoms is at most 40%. Possible compounds such as Hg-22(n-1)n can however only be stabilized if the oxygen sites of the Hg layers are occupied by almost 100%. Very occasionally a rocksalt slab is seen to terminate in the middle of a crystal, changing hereby locally the composition of the material. These defects occur mainly in crystals with large n-values.

The present electron diffraction and electron microscopy observations in a series of Hg-based compounds of composition $HgBa_2Ca_{n-1}Cu_nO_{2n+2+\delta}$ for n values ranging from n = 1 to n = 7, have shown a high perfection with virtually no defects and no secondary phases for the members n = 1, n = 2 and n = 3 of the family. Higher n-members of the family are generally faulted, and it is rather the exception to find defect free crystals. A number of these defects are discussed here; particularly the occurrence of the double Hg-layer is surprising -in view of the

low oxygen content in these layers- but opens new perspectives for the synthesis of "2 2 n-1 n" type materials.

Pure mercury superconducting materials can only be obtained under high pressure. Based however on the Hg- compounds discussed above, a number of derived materials can be synthesized at ambient pressure when part of the Hg is replaced by other elements. For the superconducting materials based on the 1201 structure [10] we have succeeded to substitute Ba for Sr into the 1201 structure and to stabilize a $HgSr_2CuO_{4+\delta}$ type structure only however if part of the Sr is replaced by La and some of the Hg is replaced by other elements such as Pb or Pr [11]. The 1201 structure is very flexible and all these substitutions do not change the structure nor the symmetry. Only when Pr is substituted on the Hg sublattice in a ratio close to 1:1 ordering occurs between Hg and Pr along the [100] direction [11]. The diffraction patterns as well as the HREM images strongly resemble those corresponding to the Ortho II structure observed for the oxygen deficient $YBa_2Cu_3O_{7-\delta}$ material.

Similar to the 1201 materials; the 1212 structure allows a large number of substitutions without drastically changing its properties. The highest Tc reached for the Ba-based compounds is 110K [4], while for the Sr-based compounds it is worthwhile noting that e.g. the compound $Hg_{0.4}Pr_{0.6}Sr_{1-x}Pr_xCu_2O_{6+\delta}$ is superconducting below 85K and has excellent magnetic properties. Again ordering takes place between Hg and Pr along the [100] direction and two different superstructures are formed, as can be concluded from the diffraction patterns; HREM evidence of the ordering in the (Hg-Pr) plane is provided in fig.3.

Intergrowths of Hg-1201 with other superconducting materials have also been prepared [7]. Tl^{+III} and Hg^{+II} are very similar ions; structurally they can be intimitely mixed so as to form an intergrowth of Hg-1201 and Tl-2201; the resulting material is superconducting but at temperatures below the transition temperature of the individual compounds.
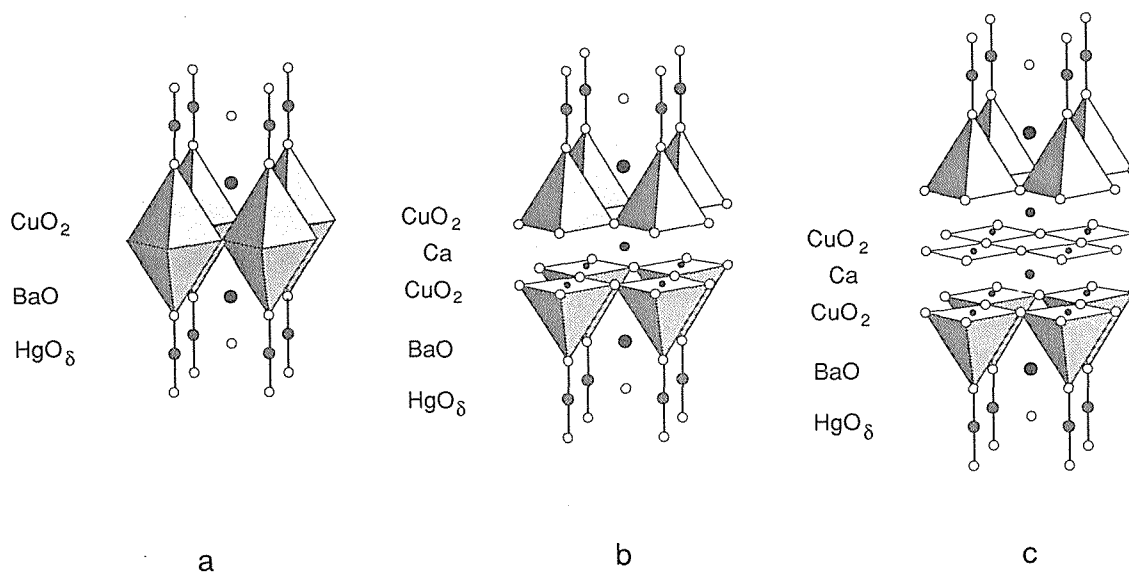
Fig.1: Schematic representation of two members of the structural family
$HgBa_2Ca_{n-1}Cu_nO_{2n+2+\delta}$
a) n = 1 or "1201" $HgBa_2CuO_{4+\delta}$
b) n = 2 or "1223" $HgBa_2CaCu_4O_{6+\delta}$
b) n = 3 or "1223" $HgBa_2Ca_2Cu_3O_{8+\delta}$
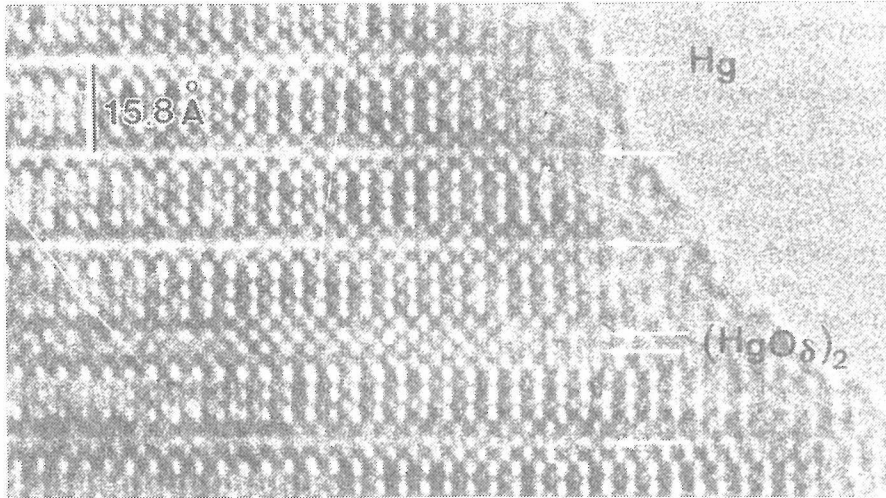
Fig.2: HREM of a defect in a Hg-1223 crystal, where a double layer of HgO_δ is present.
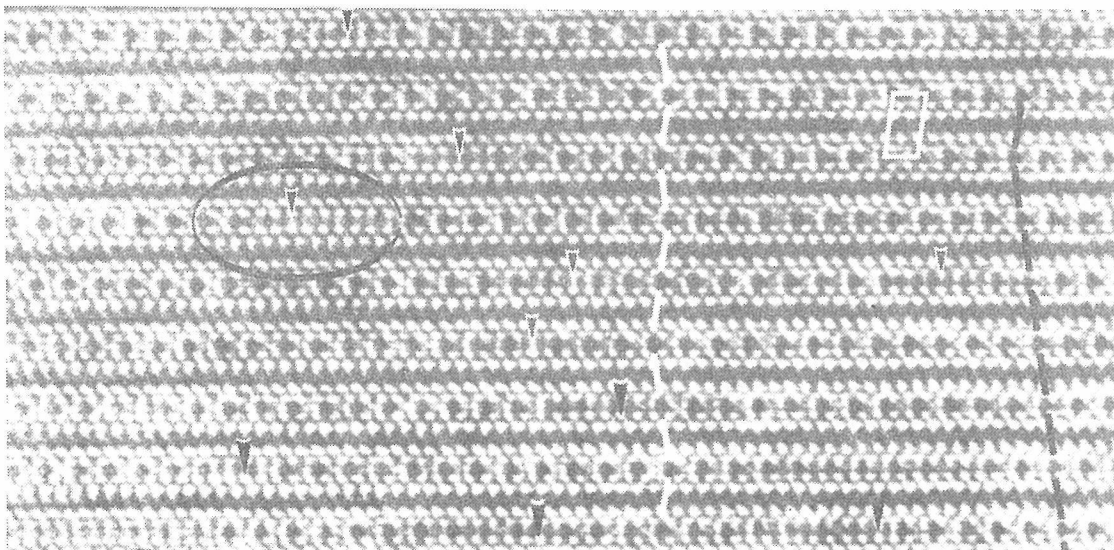
Fig. 3: HREM of a Hg-Pr superconducting compound, showing ordering between Hg and Pr which is only coherent over small distances.

Rb intercalated C_{60} material

The electron microscopic study of alkali metal fullerides is strongly hampered by the chemical reactivity of these compounds in air. In the normal ambient atmosphere the materials oxidize readily and the physical properties such as superconducting properties of A_3C_{60} are seriously affected [12]. The preparation of samples usable for electron microscopy can therefore only take place under a carefully controlled atmosphere. We have shown that samples of crystalline Rb_xC_{60} can successfully be prepared and studied inside a transmission electron microscope. The material was received from the chemical preparation laboratory (Dr. Werner, Frankfurt Germany) in an evacuated capillary tube of glass. For the preparation of the samples, use was made of double inflatable transparent plastic glove bags. The advantage of using a glove bag instead of a glove box is that the flexible bag facilitates to link the bag directly to the microscope so as to protect the specimen under a N_2 atmosphere during crushing, mounting and its insertion into the microscope.

The average grain size of the Rb_6C_{60} specimens was found to be very small (a few tens of nanometers in general) probably because of the mechanical stress induced by diffusion of Rb into the C_{60} crystals. Nevertheless satisfactory SAED patterns and HREM images, along different zone axes, could be obtained from a few grains. EDX spectra exhibit the occurrence of

rubidium and carbon while oxygen seems to be absent, as expected. The electron diffraction patterns of Rb_6C_{60} can be indexed on a body-centered cubic (*b.c.c.*) lattice with lattice parameter a = 11.56 Å, in agreement with the structure determined by X-ray diffraction [12]. The pristine host lattice of the C_{60} molecules is in fact face-centered cubic (*f.c.c.*) with a lattice parameter a_0 = 14.17 Å but it can also be described as body-centered tetragonal with a unit cell $a_0\sqrt{2}/2$ x $a_0\sqrt{2}/2$ x a_0 with a c/a ratio of $\sqrt{2}$. The filling of the octahedral interstices by rubidium atoms causes this tetragonal body-centered unit cell to flatten so as to become body-centered cubic with c/a = 1 . Stresses are therefore generated causing the disintegration of the C_{60} crystals so as to give rise to only fine particles (a few nm). For Rb_4C_{60} the structure becomes tetragonally distorted with c/a = 0.92 [13]. During heating (to 100 °C) and electron irradiation in the electron microscope, we observed a definite deviation from cubic symmetry towards a tetragonal symmetry, this is most probably related to an "in-situ" loss of Rb [14].

In the *b.c.c.* structure the molecules are arranged in close packed columns along the <111> direction; the rubidium clusters, too, project along three columns parallel to the <111> direction (fig.4a). In the [111] HREM image of fig.5, the centres of C_{60} columns show up as the largest bright dots while the rubidium columns are imaged as dark dots. Simulated images for different thicknesses and defocus values Δf are reproduced in the matrix of fig.4b. The correspondence of the simulated and observed images is quite striking, confirming the structure as proposed in [12,13].
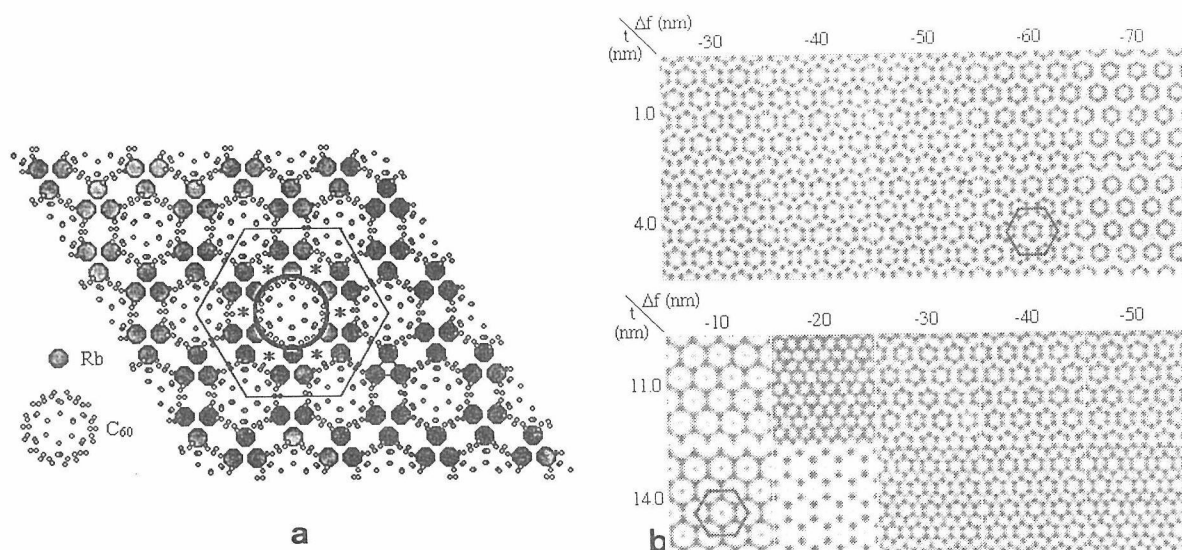
Fig.4: *(a) Projection of the b.c.c. structure along the [111] direction. A projecting C_{60} molecule is encircled which is surrounded by six C_{60} columns.*
(b) Computer simulated images for b.c.c. Rb_6C_{60} along the [111] direction. Foil thicknesses t and defocus values Δf are indicated. The hexagons outlined correspond to ones in fig.5
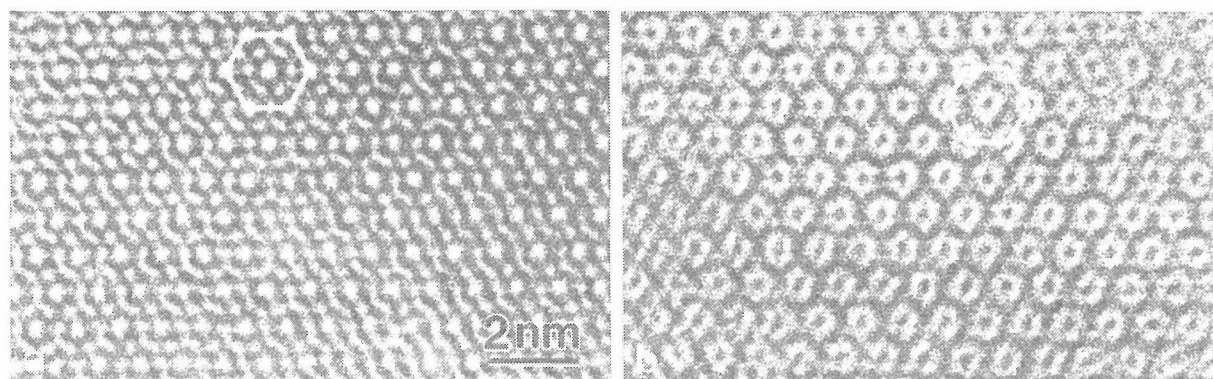
Fig.5: *[111] HREM images under different imaging conditions in (a) and (b), respectively.*

Helicoidal carbon nanotubes.

The aim of this study was to optimize the catalytic synthesis of very thin and long nanotubules similar to carbon-arc produced tubules [15] and which would not be covered by amorphous carbon. The use of silica with regular pore structure as a metal support favours the formation of stable and well dispersed Co metal particles. The particles had diameters in the 4 -15 nm range. The temperature (970 K) and reaction rate were chosen to produce well graphitized nanotubules. It was found that, after the C_2H_2 cracking, the heating of the products in a mixture of H_2 and N_2 at 873 K resulted in the gentle removal of residual amorphous carbon, leaving bare graphitic tubules. As shown in fig.6, multilayer, hollow tubules with inner and outer diameters of 3 - 7 nm and 15 - 20 nm, respectively, and up to 30 μm in length were obtained.

The electron diffraction pattern of a single turn of the helical tubule exhibits spotty arcs of 0002 and 0004 graphite reflections as well as diffuse arcs of $10\bar{1}0$ and $11\bar{2}0$ reflections (fig.7a). Such complex diffraction patterns can be analysed in detail [16]. The local graphite structure will in general be turbostratic. The 000l arc segments in diffraction patterns would be continuous for a circular helix, the brightness being the largest at the extremities and the smallest in the central part. However, for a periodically polygonized helix, the arcs should become "spotty", the spot density being the largest at both ends and the smallest in the central part. The observed arcs indeed show the latter feature (fig.7b), revealing the polygonal nature of the helix tubes. The inset of fig.6 shows that the angular bends observed in the helix are consistent with the spotty appearence of the 0002 arcs. The straight sections of the polygonally coiled fibers produce the same diffraction effects as the electric arc grown straight fibres first observed by Iijima [15] and analysed in detail in [17,18].

The angular bends strongly suggest that the catalyst-grown coiled tubules have a texture which has the same topology as the single sheet models of carbon helices derived from molecular-dynamics simulations [19]. These models relate the angular bends to the repeated occurrence along the helix of pairs of pentagon-heptagon carbon rings within the hexagonal graphene grid. If the distribution of such singularities is more or less periodic and become aligned in successive tubes as a result of epitaxial growth, the helix appears polygonal. If the singularities are more randomly distributed, the helix will look more circular.
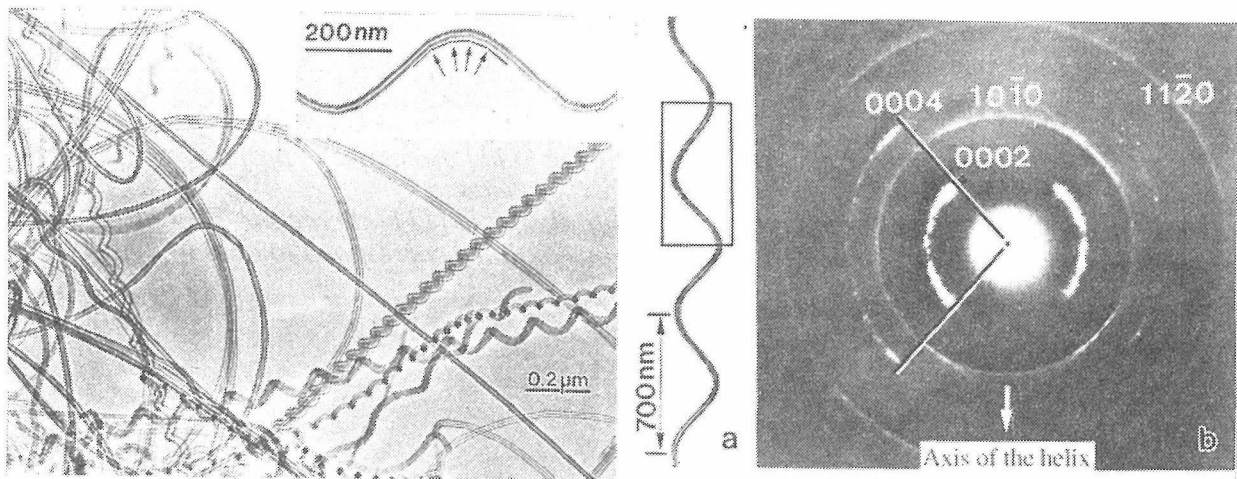
Fig.6 Differently shaped carbon fibers produced by thermal cracking of acetylene on a finely devided cobalt catalyst. Inset: magnified part of a helix exhibiting polygonization.

Fig.7: (a) Graphite helix used for the diffraction experiment.
(b) Selected-area electron diffraction pattern from the framed part in (a).

Crystal Structure Analysis by High-Resolution Electron Microscopy

Kenji Hiraga

Institute for Materials Research, Tohoku University, Katahira, Aoba-ku, Sendai 980, Japan

1. Introduction

Present electron microscopes have resolutions of higher than 0.2 nm, and so heavy atoms in simple crystal structures can be individually represented as separated dark spots. Therefore, high-resolution electron microscopy is a powerful tool for crystal structure analysis, if we carefully use it. In this paper, I review current studies of our group on two subjects. One is high-Tc superconductors based on the Perovskite-type structure. In this case, observed high-resolution images give us information not only for arrangements and accurate coordinates of cations, but also for positions of oxygen atoms[1-3]. Second subject is decagonal quasicrystals which produce sharp diffraction spots in spite of their aperiodic structures. In this case, high-resolution electron microscopy is an important tool for investigating their real structures, and makes it possible to determine local atomic arrangements in fundamental atom clusters and long-range arrangements of the atom clusters[4-7].

The high-resolution images presented in this paper were taken with a 400 kV electron microscope (JEM-4000EX) having a resolution of 0.17 nm.

2. High-Tc Superconductors

Figure 1(a) shows a high-resolution image of the $TlBa_2Ca_3Cu_4O_{11}$ superconductor, taken with the incident beam parallel to the b-axis. In this image, cations of Tl, Ba, Cu and Ca are represented as dark spots with different darkness and/or size which are nearly proportional to their atomic numbers. That is, from this image, we can directly determine an arrangement of the cations. Also, the dark spots in this image has information on positions of the cations. Fig. 1(b) shows a simulation image calculated under the Scherzer defocus of -45 nm and crystal thickness of 2 nm. The image reproduces well the observed image contrast of Fig. 1(a). The dark spots in the calculated image show accurate positions of cations. The z coordinates of cations, measured from the positions of the dark spots in Fig. 1(a) and Fig. 1(b), are consistent with those used in the calculation, which are values determined with X-ray diffraction, within an error of 0.01 nm. The error of 0.01 nm may be in a measuring error. This result shows that one can determine coordinates of cations from this type of images within an error of 0.01 nm.

Unfortunately, oxygen atoms can not be represented as dark spots in high-resolution images taken with the present microscope. However, information on oxygen atom positions is contained in the observed image of Fig. 1(a). Figs. 1(b) and 1(c) are images calculated from two types of structure models, in which octahedral positions on the Ca layers are occupied by vacancies in Fig. 1(b) and by oxygen atoms in Fig. 1(c). From the comparison between Figs. 1(b) and 1(c), one can easily notice that the vacant positions indicated by Ov show brighter contrast than the oxygen positions. Also, The observed image of Fig. 1(a) shows that oxygen
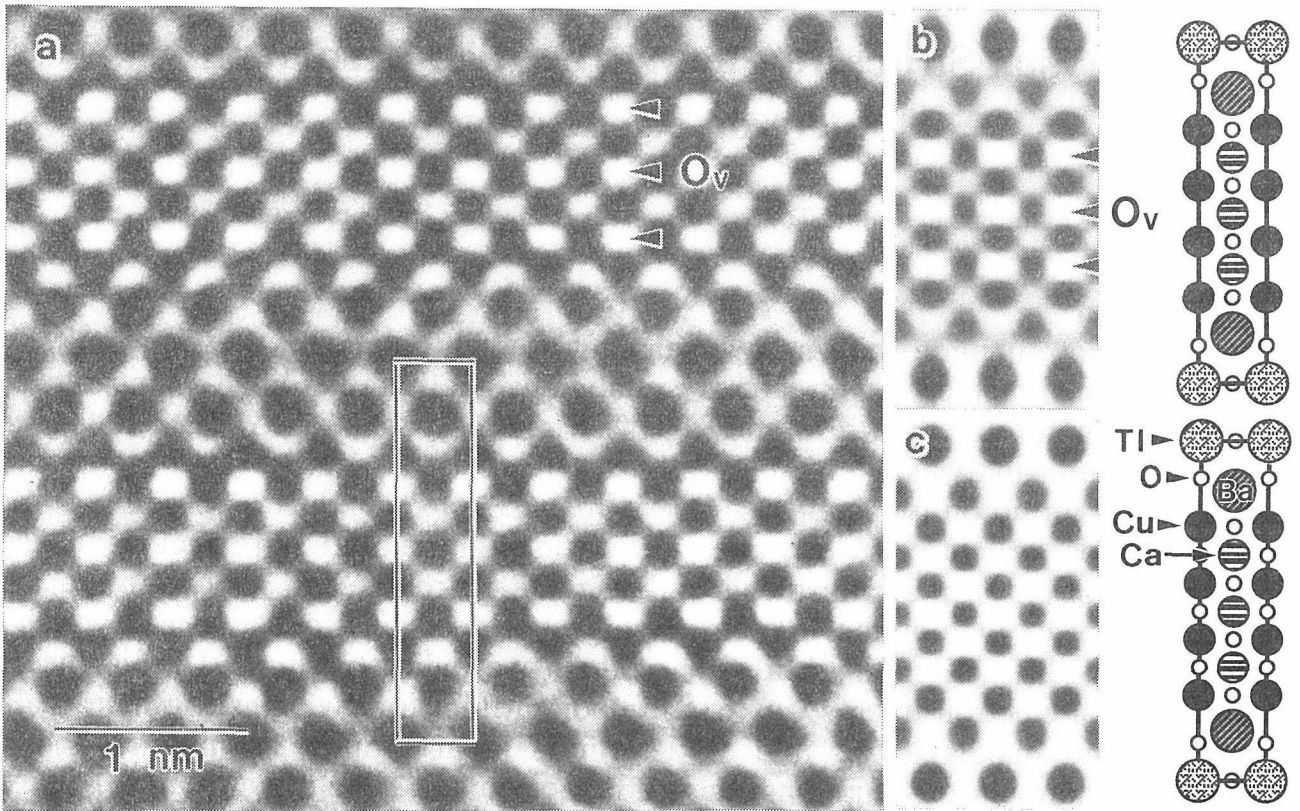
Fig. 1 (a): high-resolution image of $TlBa_2Ca_3Cu_4O_{11}$, and (b) and (c): calculated images of two models with vacancies and oxygen atoms on the Ca layers, under a defocus value of -45 nm and crystal thickness of 2 nm.

1.96 nm   2.74 nm
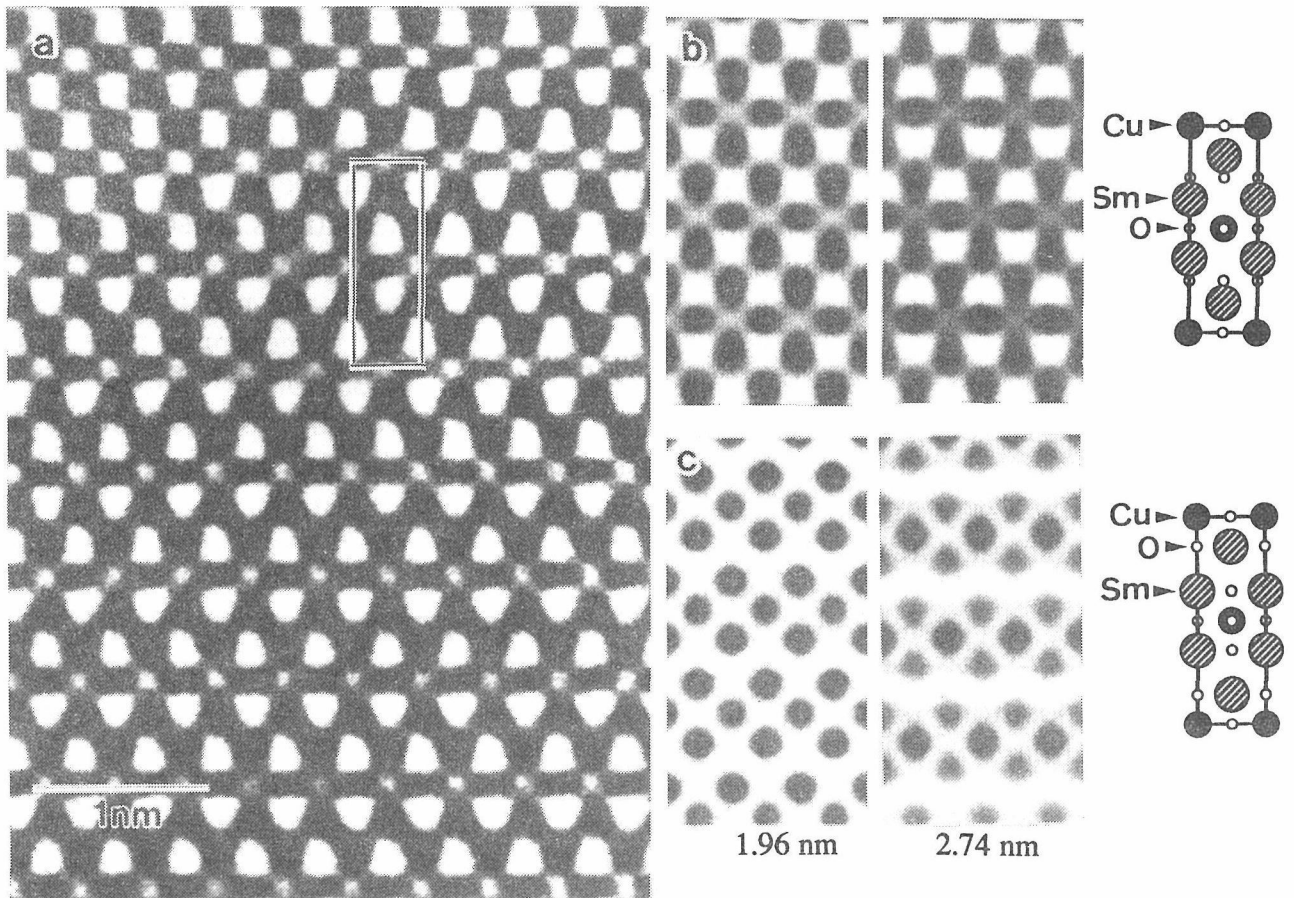
Fig. 2 (a): high-resolution imag of Sm_2CuO_4, and (b) and (c): calculated images of two models under a defocus value of -45 nm and crystal thichnesses of 1.96 nm and 2.74 nm.

positions on the Ca layers are vacant. That is, from the close examination of contrast of the bright regions in this type of images one can determine ordered arrangements of oxygen atoms located at positions between the cations

In addition to ordered arrangements of the oxygen atoms, this types of high-resolution images give us information for positions of oxygen atoms. Figs. 2(b) and 2(c) show high-resolution images calculated from two structure models for a Sm_2CuO_4 superconductor, in which oxygen atoms except for ones on the Cu layers are placed at tetrahedral and octahedral sites of surrounding cations, respectively. The difference between the two calculated images is noticeable, particularly in a thick crystal. An observed image of Fig. 2(a) shows a good correspondence to the calculated image of Fig. 2(b). That is to say, it can be concluded from the observed image that the oxygen atoms in the superconductor are located at the tetrahedral sites.

In conclusion, from high-resolution electron microscopy of the high-Tc superconductors, one can obtain valuable information for crystal structure analysis; i. e., arrangements and coordinates of cations, ordered arrangements of oxygen atoms and oxygen vacancies, and positions of oxygen atoms.

3. Decagonal Quasicrystal

Quasicrystals have aperiodic structures in spite of showing sharp spots in diffraction patterns. High-resolution electron microscopy is an important tool for investigating the aperiodic structures in real space. In this paper, I will show an example of structure analysis for decagonal quasicystals. The decagonal quasicrystals have a periodic structure along one axis (tenfold symmetry axis) and quasiperiodic (aperiodic) structures on the planes perpendicular to the tenfold axis. High-resolution images of the decagonal quasicrystals, taken with the incident beam parallel to the tenfold axis (periodic axis), are relatively easy to be interpreted, compared with those of icosahedral quasicrystals having three-dimensionally quasiperiodic structures, and one can determine quasiperiodic structures from the observed images directly. Recently, our group determined atomic arrangements in atom columns, which are structure units forming decagonal quasicrystalline structures, by the aid of diffraction method[4-7]. In this paper, I will show the structure analysis for the Al-Pd-Mn decagonal quasicrystal.

Figure 3(a) is a high-resolution image of the Al-Pd-Mn decagonal quasicrystal, taken with the incident beam parallel to the tenfold axis. The image may be taken from a thin crystal of about 5 nm in thickness, and so it faithfully reproduces projected potential of the sample along the incident beam. That is to say, the dark and bright regions in the image correspond to high- and low-potential regions, respectively. In the image, one can see small ring contrasts consisting of a dark ring surrounding a bright ring and a central dark dot. An arrangement of the ring contrasts in the image is schematically drawn in Fig. 3(b). The ring contrasts are joined by a definite linkage and form decagons. And all the decagons are joined with a definite linkage, namely by sharing two ring contrast, and so all the decagons show the same direction. The gaps in an arrangement of the decagons are perfectly filled up by star-shaped pentagons and hexagons, without any overlaps and without gaps, as can be seen in Fig. 3(b). That is to say, the structure of the Al-Pd-Mn
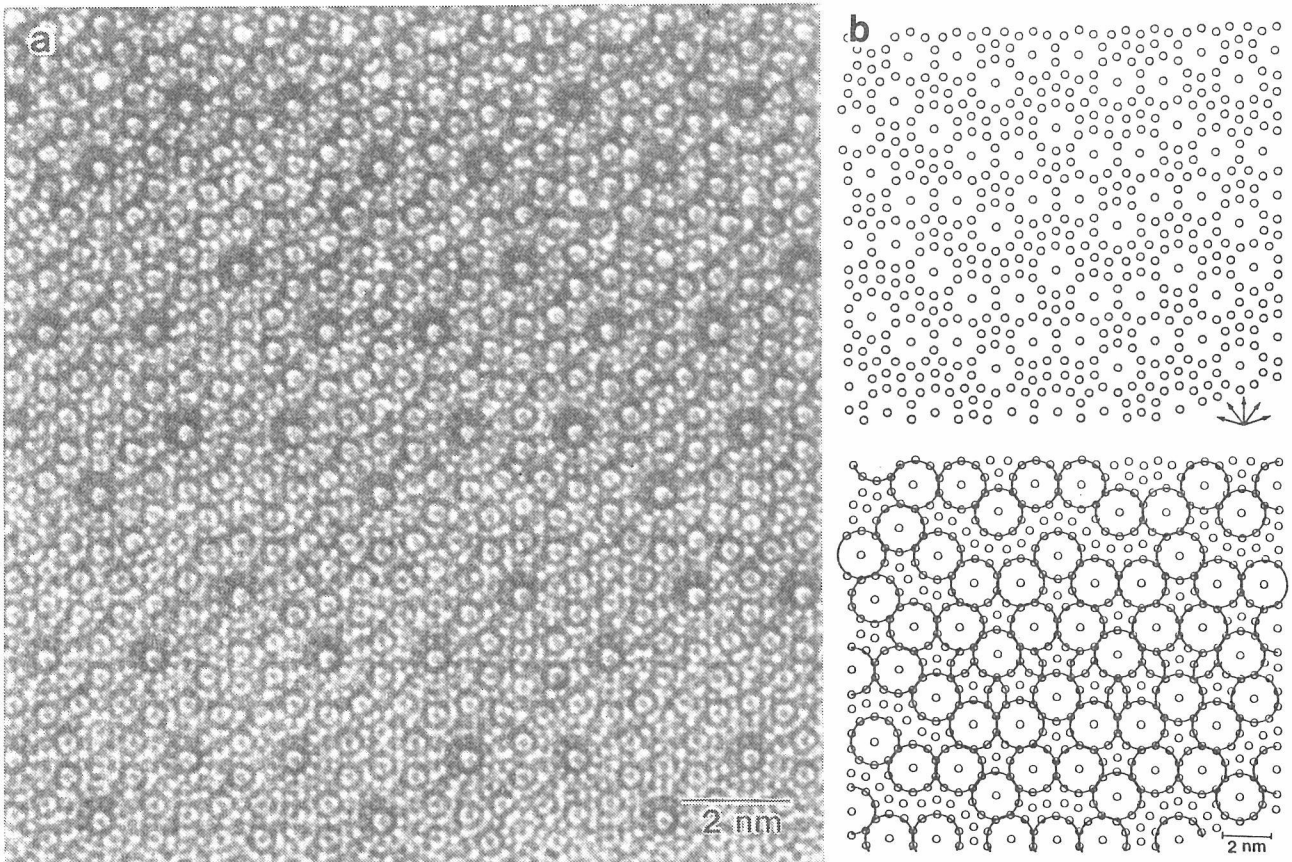
Fig. 3 (a): high-resolution image of the Al-Pd-Mn decagonal quasicrystal, and (b): an arrangement of atom columns (ring contrasts in the image) and an arrangement of atom clusters enclosed by circles.
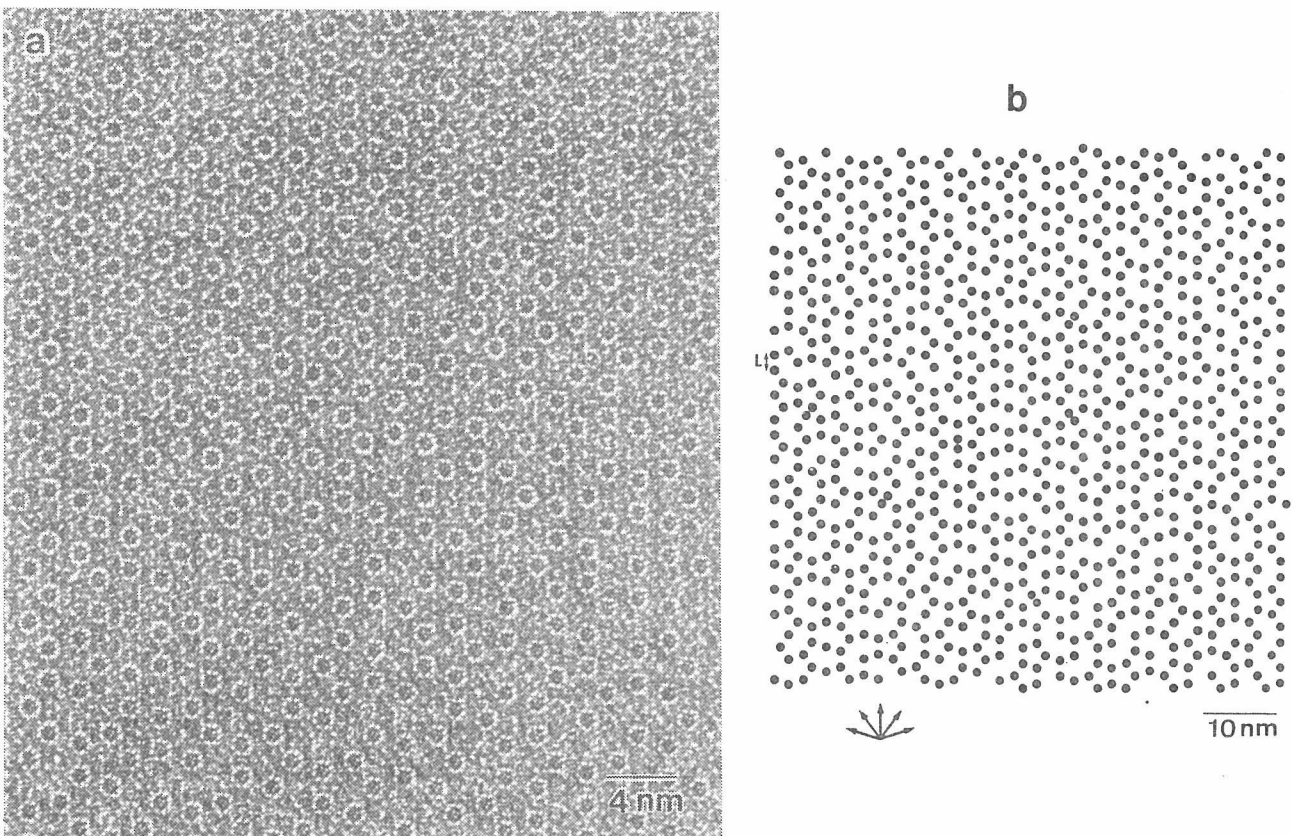
Fig. 4 (a): high-resolution lattice image of the Al-Pd-Mn decagonal quasicrystal, and (b): an arrangement of decagonal atom columns (bright rings in the image).

decagonal quasicrystal can be interpreted as a space-filling tiling using these three types of polygons, the decagon, star-shaped pentagon and hexagon. Thus the determination of atomic arrangements in the three polygons leads to a solution for the structure of the decagonal quasicrystal. Also, if we know an atomic arrangement in the atom column showing the ring contrast in the observed image, atomic arrangements in large parts of the three polygons except for the central part of the decagon can be uniquely determined, because the three polygons are formed by a definite linkage of the atom column. The atomic arrangement in the atom column showing the ring contrast was proposed by analogy with the structure of an Al_3Mn crystalline phase[6]. The atom column consists of stacking of pentagonal atom arrangements. A high-resolution image calculated from our structural model in the three polygons could reproduce the observed image contrast[7].

In the decagonal quasicrystal, the decagonal atom clusters are arranged with long-range correlation, which produces sharp diffraction spots. Fig. 4(a) is a high-resolution image taken from a relatively thick region (probably a few ten nm). The bright ring contrasts show the decagonal atom clusters, and so one can determine directly an arrangement of the decagonal atom clusters from the observed image. Fig. 4(b) is a schematical drawing of the arrangement of the atom clusters. In the drawing, one can see straight arrays of the atom clusters for long distances along the five directions. The straight arrays with long range correlation result in the sharp diffraction spots of the decagonal quasicrystal.

REFERENCES
1) K. Hiraga, D. Shindo, M. Hirabayashi, M. Kikuchi, K. Oh-ishi and Y. Syono: Jpn. J. Appl. Phys., 26 (1987) L1071.
2) K. Hiraga, D. Shindo, M. Hirabayashi, M. Kikuchi, N. Kobayashi and Y. Syono: Jpn. J. Appl. Phys., 27 (1987) L1848.
3) K. Hiraga, T. Oku, D. Shindo and M. Hirabayashi: J. Electron Microsc. Technique, 12 (1989) 228.
4) K. Hiraga: in Quasicrystals: The State of the Art (eds. D. P. Divincenzo and P. J. Steinhardt), World Sci. (1991) p95.
5) K. Hiraga, F. J. Lincoln and W. Sun: Mater. Trans. JIM, 32 (1991) 308.
6) K. Hiraga, M. Kaneko, Y. Matsuo and S. Hashimoto: Philo. Mag. B, 67 (1993).
7) K. Hiraga and W. Sun: Philo. Mag. Lett., 67 (1993) 117.

Recent Progress of Electron Spectroscopy for Quantification
– Shake-up Satellite Extracted from Au-4f XPS Spectrum –

*Hideki Yoshikawa * and Ryuichi Shimizu*
Department of Applied Physics, Osaka University, Japan
*Present, NEC Fundamental Research Laboratories, Japan

Abstract

Surface loss function has been derived from REELS-Spectra by extended Landau formulation, in which Landau's formula for inelastic scattering is combined with Monte Carlo analysis to include the contribution of elastic scattering. This approach has been applied for deriving the surface loss function of kV-electrons for gold, and verified by applying this surface loss function to the background subtraction of Au 4f XPS-spectrum.

The result has revealed that the source function of Au 4f is associated with two shake-up satellite peaks which attribute to the shake-up peaks through Au 6s→7s transition according to Harmann-Skillmann atomic orbital calculation based on Xα approximation.

Shake-up satellites of X-ray photo-electron spectroscopy(XPS) spectrum are to be associated with many electron phenomena, and have been extensively studied, particularly for free atom and molecules[1,2]. Even though these shake-up satellites only have tiny intensities of several percent[1] of the main peak, atomic state shake-up phenomena have quite often been quantitatively discussed since the system enables one to separate the shake-up spectra from the unfavorable satellites caused by the inelastic scattering of photo-electrons with other atoms[2]. For solid materials, the inelastic scattering spectrum(i.e., XPS background) is of larger intensity and is distributed continuously over a wide energy region. This makes it difficult to identify tiny peaks such as those of the shake-up satellites by separating them from the intense inelastic scattering spectrum. Some exceptions occur for the chemical compounds of transition metals and rare earth metals[3-5] which have intense shake-up satellites. In general, one has to subtract the inelastic scattering spectrum(background) precisely from the XPS spectrum.

The background subtraction of XPS has been widely used in quantitative surface chemical analysis[6] using the simple linear approximation or by Shirley's method[6]. However, these do not take into account the characteristic energy loss structure inherent to each material. Recently, Tougaard has proposed background subtraction

approach based on Landau's formula[7]. He has succeeded in describing the energy loss structure using the differential inelastic scattering cross-section obtained experimentally for each material. Thus, Tougaard's method has enabled one to obtain the original XPS spectrum(i.e., source function), including shake-up spectrum, by subtracting the background spectrum. Applying this approach to noble metals(Cu, Ag, Au), Tougaard has obtained asymmetric source function associated with the tails extending over ~40 eV. These he presumed to be described by the picture that the conduction electrons screen the core hole potential excited by a photon[8].

It is well known that the Doniach-Sunjic distribution[9] provides an asymmetric source function originating from this picture. However, this Doniach-Sunjic distribution does have an asymmetric tail and only up to several eV even for free electron metals[10]. This is one order of magnitude smaller than the source function derived by Tougaard. Furthermore, Hufner and Wertheim[11] have pointed out that the Doniach-Sunjic type asymmetric tail for Au 4f is very small by fitting the Doniach-Sunjic curve into experimental data. The marked tailing in the source function derived by Tougaard, therefore, is probably not associated with the Doniach-Sunjic process as he suggested, but is more probably due to the use of the differential inelastic scattering cross-section. Hence, whereas it is quite accurate for describing the energy loss processes in bulk, it is less applicable for the surface region as will be discussed later.

In the previously mentioned work[12], it was pointed out that the differential inelastic scattering cross-section derived from transmission electron energy loss spectroscopy(TEELS), as used by Tougaard, is not adequate to be applied directly to XPS for the following reason. XPS is primarily associated with those kV photo-electrons which transverse the surface region. These photo-electrons undergo not only bulk excitations but also more significantly surface excitations[12,13]. The XPS source function derived by the subtraction of the background should, therefore, depend significantly on the choice of the inelastic scattering differential cross-section.

In the present work, we attempt to derive original source function of Au 4f satellites by using an inelastic scattering cross-section which we consider to be more precise. We first , perform a reflection electron energy loss spectroscopy(REELS) measurement in order to derive the inelastic scattering differential cross-section. We focus on those 1 kV electrons that impinge on Au at the incident angle of 45° and come out of the surface where they are detected with an electrostatic analyzer set at the take-off angle of 45°. Since major part of those detected electrons undergo plural inelastic scattering events in this situation, we have applied Monte Carlo analysis to extract the inelastic scattering

differential cross-section from the REELS spectrum. This spectrum contains significant contributions of elastic scattering as well as of plural inelastic scattering.

The Monte Carlo analysis[12] based on dielectric response theory[14] allows us to derive the inelastic scattering differential cross-section from the REELS experiment leading to the energy loss function represented by the solid line in Fig.1. The dashed line in Fig.1 represents the energy loss function derived optically(i.e., optical loss function)which is similar to the TEELS data[15]. In comparison with the optical loss function Im[-1/ε], the present energy loss function is much enhanced in the low energy loss region and hence much closer to the surface energy loss function Im(-1/[ε+1])[12]. This suggests that contribution of the surface excitation is more significant for those kV electrons emitted through the surface region.
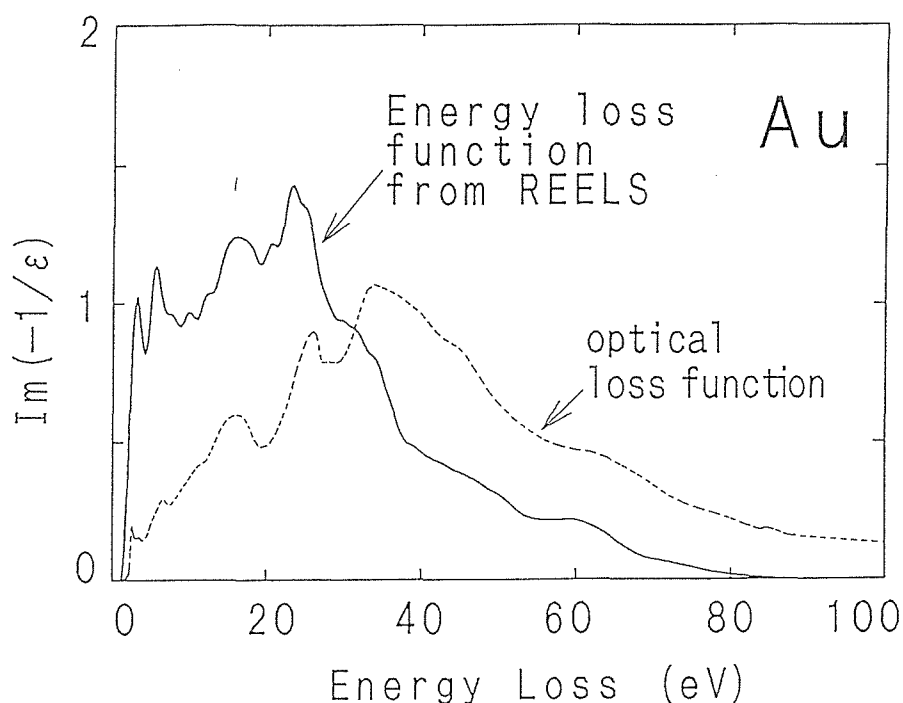
Figure 1   Energy loss function of Au derived by Monte Carlo analysis of the REELS-spectrum measured under the condition that 1 kV electrons impinge on Au at the incident angle of 45° and come out of the surface where they are detected with an electrostatic analyzer set at the take-off angle of 45°. The dashed line indicates the optical loss function.

Next, using this new energy loss function, we have performed Monte Carlo simulation of the formation of the background generated by Au 4f photo-electrons. Figure 2 shows the experimental Au 4f XPS spectrum excited by Al Kα. The background spectrum is magnified by fivefold relative to $4f_{7/2}$ peak. The experimental condition is depicted in the inset. More details of the experiment are described elsewhere[12].

The Au 4f XPS source functions extracted from the experimental data, shown in Fig.2, are represented by the curves *a* and *b* in Fig.3, which were obtained by Monte Carlo simulation using respectively, the optical loss function and the present energy loss function. These spectra are magnified by tenfold relative to the Au $4f_{7/2}$ peak. The source function using the optical loss function has a tail extending over ~50 eV which is very close to Tougaard's result derived using the TEELS data. The curve *b* in Fig.3 does show the tailing to be almost completely extracted.
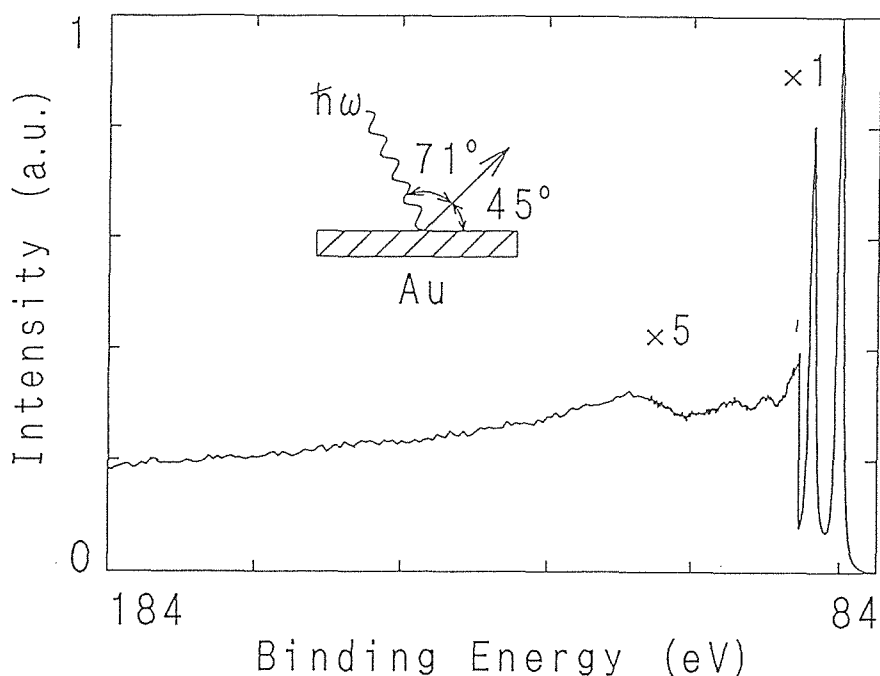
Figure 2   Experimental Au 4f XPS spectrum measured under the condition; angle of incidence of primary Al Kα X-rays is 71° and take-off angle of Photo-electrons 45°. The background spectrum is magnified by fivefold relative to $4f_{7/2}$ peak.

The result shown in Fig.3 indicates that the bulk energy loss function derived from optical or TEELS measurements overestimate intensity of the XPS source function by 55% compared to that of the source function derived from the present energy loss function. This shows how the choice of energy loss function can influence evaluation of signal intensities in the quantitative XPS.

Tiny satellites are still visible at the binding energy of 93.5 eV and 98 eV on curve b. With respect to another type of shake-up process, Penn[16] has suggested theoretically that the intrinsic plasmon loss is induced by another shake-up, different from the Doniach-Sunjic process.

We, therefore, tried to interpret the Au 4f satellites as derived from intrinsic plasmon or intrinsic interband transition, the energy structure of which could coincide with the loss peaks in the REELS spectrum. However, this proposition has turned out to be not effective in identifying the satellites peaks.
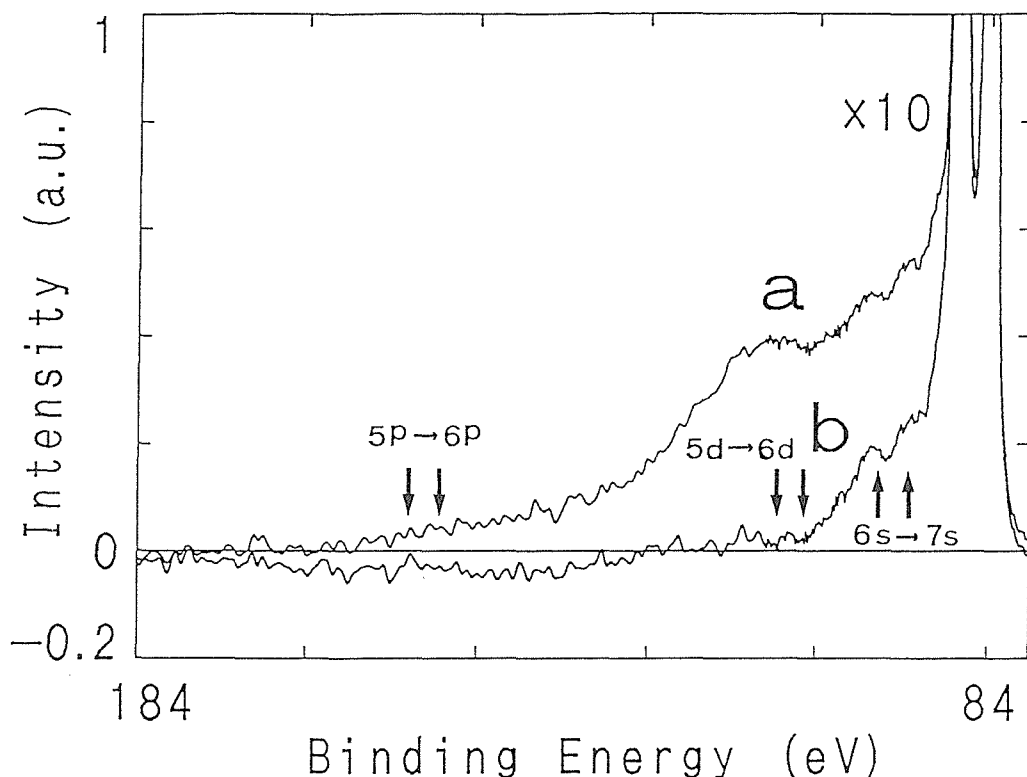
Figure 3   Au 4f XPS source functions extracted from the experimental data in Fig.2 by means of Monte Carlo analysis using the optical loss function (the dashed line in Fig.1), curve a and by the energy loss function (the solid line in Fig.1), curve b. The background spectra are magnified by tenfold relative to $4f_{7/2}$ peak. The arrows display the energy position of the shake-up satellites obtained by Harmann-Skillmann atomic orbital calculation according to the monopole transition; 6s→7s, 5d→6d and 5p→6p.

The plasmon peaks of REELS-spectrum, however, have turned out not to coincide with those of the XPS satellites. Therefore, we have performed Harmann-Skillmann atomic orbital calculation using the Xα-approximation to examine another possibility whether or not these satellites may derive from shake-up peaks caused by intra-atomic transitions. The result is represented by the arrows in Fig.3 corresponding to the monopole transitions; 6s→7s, 5d→6d and 5p→6p. It appears that the energy position of the transition of Au 6s→7s is in good agreement with the experiment. This is perhaps comparable with the result for Hg vapor where the maximum shake-up process is the transition, 6s→7s[17]. This

result may lead to the speculation that the shake-up process in an atomic state can occur even for a solid surface. A more complete investigations in both measurement and theoretical calculation are necessary to fully understand this shake-up process in the Au surface.

In conclusion, the XPS background subtraction approach using Monte Carlo analysis based on the use of the present surface energy loss function has enabled us not only to correct more effectively the background but also to reveal tiny satellites leading to a more comprehensive understanding of surface chemical analysis by XPS.

References
[1]   U.Gelius, J.Electron Spectrosc. Related Phemomena 5(1974)985.
[2]   K.Siegbahn, J.Electron Spectrosc. Related Phemomena 5(1974)3.
[3]   C.S.Fadley, 'Electron Spectroscopy: Theory, Techniques and
      Applications' Vol.2(Academic Press, 1978) eds. C.R.Brundle and
      A.D.Baker, pp.103-131.
[4]   T.Novakov, Phys. Rev. B3(1971)2693.
[5]   A.Rosencwaig, G.K.Wertheim and H.J.GuggenHaim, Phys, Rev. Lett.
      27(1971)479.
[6]   D.Briggs and M.P.Seah, 'Practical Surface Analysis by Auger and
      X-ray Photoelectron Spectroscopy(John Wiley & Sons Ltd. 1983).
[7]   L.Landau, J. Phys.(Moscow)8(1994)201.
[8]   S.Tougaard, Phys. Rev. B34(1986)6779.
[9]   S.Doniach and M.Sunjic, J. Phys. C3(1970)285.
[10] P.H.Citrin, G.K.Wertheim and Y.Baer, Phys. Rev. B16(1977)4256.
[11] S.Hufner and G.K.Wertheim, Phys. Rev. B15(1975)678.
[12] H.Yoshikawa, T.Tsukamoto and R.Shimizu, Scanning Electron
      Microscopy/1992 (Scanning International, Chicago, 1992) in
      press.
[13] W.J.Pardee, G.D.Mahan, D.E.Eastman, R.A.Pollak, L.Ley,
      F.R.McFeely, S.P.Kowalczyk and D.A.Shirley, Phys. Rev.
      B11(1975)3614.
[14] Z.-J.Ding and R.Shimizu, Surf. Sci. 222(1989)313.
[15] C.Wehenkel, J.Physique 36(1975)199.
[16] D.R.Penn, Phys. Rev. Lett. 38(1977)1429.
[17] S.Svensson, N.Martensson, E.BAsilier, P.A.Malmqvisi, U.Gelius
      and K.Siegbahn, J.Electron Spectrosc. Related Phenomena
      9(1976)51.

Recent Advances in Analytical Electron Microscopy and Its Application to Materials Science

D.B. Williams

Department of Materials Science & Engineering, Lehigh University, Bethlehem, PA, U.S.A.

1. Introduction

Analytical Electron Microscopy (AEM) comprises techniques that provide quantitative analytical information about thin specimens in the transmission electron microscope (TEM). The two principal techniques are X-ray Emission Spectrometry (XES) using energy dispersive x-ray spectrometers (EDS) and Electron Energy-Loss Spectrometry (EELS) using magnetic prism electron spectrometers. Both of these techniques can be used simultaneously to provide quantitative elemental, chemical and other information about the specimen on a scale of < 5 nm. Advances in the techniques of AEM have emphasized improvements in the spatial resolution of microanalysis. However, a consequence of the advances in instrument design to optimize spatial resolution is that the quality of the analytical signals degrades, thus compromising minimum detectability limits. Nevertheless, recent advances in both x-ray and electron spectrometry have resulted in the ability to detect the presence of a few atoms in the analyzed volume. This combination of nanometer-level spatial resolution and near atomic-level detectability promises to open many new avenues for materials research. Furthermore, both techniques are advancing to the stage where the analytical information can be presented in the form of a quantitative map of the particular signal being analyzed, and these maps complement the electron images that are produced in the conventional way in the TEM.

2. Advances in XES - Spatial Resolution and Minimum Detectability

a) Limits of Spatial Resolution

The spatial resolution of x-ray microanalysis is a measure of the smallest distance (R) between the centers of two analysis volumes from which independent x-ray microanalyses can be obtained. The definition of R has evolved over the last fifteen years as the AEM has improved and smaller analysis volumes have become attainable. It has long been recognized (Goldstein et al., 1977) that the analysis volume and hence R is governed by the beam-specimen interaction volume since the EDS in the AEM can detect x-rays generated anywhere within that volume. The interaction volume is a function of the beam diameter (d) and the beam broadening (b). The beam broadens primarily as a result of high angle elastic scatter of electrons within the specimen. To a first approximation, the broadening (b) is given by:-

$$b = 7.21 \times 10^5 (Z/E_0) \, (\rho/A)^{1/2} \, t^{3/2} \qquad 1$$

where Z is atomic number, A is atomic weight, E_0 is the beam energy in eV, ρ is the specimen density in gm/cm^3 and t is the specimen thickness in cm. Reed (1982), assuming that the beam intensity distribution is Gaussian, proposed that R be defined as:-

$$R = (d^2 + b^2)^{1/2} \qquad 2$$

Based on the Gaussian model and experimental measurements, Michael et al. (1990) proposed that Reed's definition of R be modified so as not to present the worst case (given by the exit beam diameter) but to define R at a plane midway through the thin foil:-

$$R = (d + R_{max})/2 \qquad 3$$

where R_{max} is given by equation 2.

Typical best values of R are in the range 3 - 10 nm for a field emission gun (FEG) AEM at 100 kV and 10 - 50 nm for 100 - 300 kV thermionic source instruments (Michael et al. 1990). Much of the development of AEMs has gone into attempting to improve the spatial resolution by minimizing d through the development of FEG electron sources and minimizing b through the use of higher accelerating voltages. Ideally, of course, the best spatial resolution should be achieved through a combination of both intermediate voltages and FEGs and several such instruments have been designed and built with these criteria in mind (e.g. Lyman et al., 1994).

Sophisticated Monte Carlo simulations using parallel supercomputers have shown that the definition of spatial resolution given by equation 3 is a reasonable approximation to experimentally-measured values. Usually, the specimen itself limits the spatial resolution, but Monte Carlo simulations suggest that, for the thinnest specimens, there is little to be gained by increasing voltages significantly above 100 kV as shown in figure 1 (Williams et al. 1992). While this result is surprising, it has not yet been proven experimentally. However, even where it is not possible to produce specimens much < 50 nm thick, the best reported experimental spatial resolution is still <~ 5 nm, which has already been achieved with a 100 kV FEG as shown in figure 2. So while 300 kV FEG AEMs may improve these numbers slightly, it is clear that the limit of spatial resolution is being approached and there is little room for improvement.

b) Improvements in Minimum Detectability

Minimum detectability and spatial resolution are inversely related. An improvement in resolution is balanced by a worsening of the minimum mass fraction (MMF), all other factors being equal. This is because the way to improve spatial resolution is to reduce the analyzed volume and consequently the characteristic x-ray signal intensity is reduced, thus making it statistically more difficult to detect signal from small fractions of a given element. In addition, increasing the accelerating voltage also results in less ionizations per unit volume, further lowering the generated x-ray intensity. The minimum mass fraction is defined as:-

$$MMF = (P \cdot P/B \cdot \tau)^{-1/2} \qquad\qquad 4$$

where P is the x-ray peak intensity, P/B is the peak to background ratio and τ is the counting time. Typically the best MMF detectable for a thermionic source instrument is about 0.1 - 1.0 wt. % while an FEG instrument is capable of detecting 0.01 wt. % - 1.0 wt. % of most elements (Lyman and Michael 1987). More recently it has proved possible to design an AEM to optimize the MMF. This instrument, an ultra-high vacuum 300 kV FEG AEM is currently being installed at Lehigh and preliminary calculations (Lyman et al. 1994) indicate that a MMF of <0.01% is feasible as shown in figure 3. This translates in a detectability limit of ~3 atoms.

This new AEM has incorporated several features designed to maximize the detectability of x-rays through maximizing the three terms in equation 4. First the peak intensity is maximized through several innovative design combinations:- 1) use of a FEG source; 2) the use of two x-ray detectors (rather than one as traditionally used in AEM). The two detectors, one Si(Li) and one intrinsic Ge are in equivalent geometrical positions relative to the specimen; 3) creation of detector collection angles of ~0.3 sr, almost twice the previous best reported value; 4) the first implementation of megahertz-rate beam blanking to generate increased throughput of x-ray counts by minimizing pulse pile up in the system electronics. The P/B ratio is maximized by:- 1) availability of 300 kV electrons and 2) careful design of the illumination system and stage to minimize background radiation. Counting time is maximized through 1) ultra-high vacuum stage design, 2) in-situ specimen cleaning facilities to keep contamination to a minimum, thus maximizing counting time 3) liquid N_2 stage cooling, 4) thermal compensation to minimize stage drift and 5) computer controlled image drift compensation. All of these features will result in the highest possible x-ray sensitivity and for the first time it is possible to contemplate quantitative mapping of x-rays in thin foils, which hitherto has been compromised by the low count rate obtained from thin foils in the AEM.

More recent advances in instrumentation that will improve x-ray microanalytical performance have come from improvements in spectrometers and associated electronics. The development of intrinsic Ge detectors with better energy resolution (Cox et al., 1988) and the invention of digital processing technology to optimize x-ray count rates (Mott and Friel, 1993) will enhance the quality of the data generated. Software analysis is becoming increasingly sophisticated, yet the most complex systems can now be run on personal computers such as the Desk Top Spectrum Analyzer system (DTSA 1991), making advanced data processing available to all at a reasonable price.

c) Materials Applications

Applications of thin foil x-ray microanalysis utilizing the high spatial resolution and minimum detectability have traditionally involved studies of segregation to interfaces such as grain boundaries and interphase interfaces, as already shown in Figure 2. From such data it has proven possible to quantify Gibbsian monolayer segregation, relate such segregation to boundary crystallography, make low temperature diffusion measurements and determine low temperature
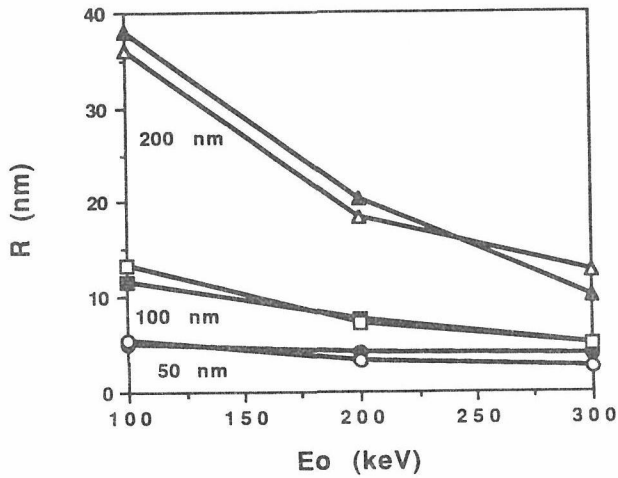
FIGURE 1

Monte Carlo calculations showing the effect of electron energy on the spatial resolution for Cu foils of various thickness. Note the small improvement of 50 nm thickness. From Williams et al., (1993) Reproduced courtesy of Elsevier Science Publishers, B.V.
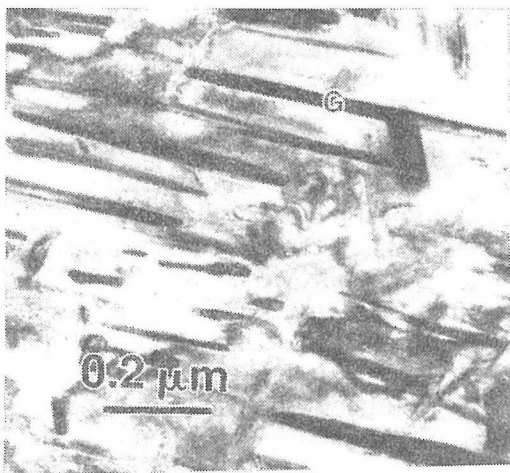
FIGURE 2a

FIGURE 2b
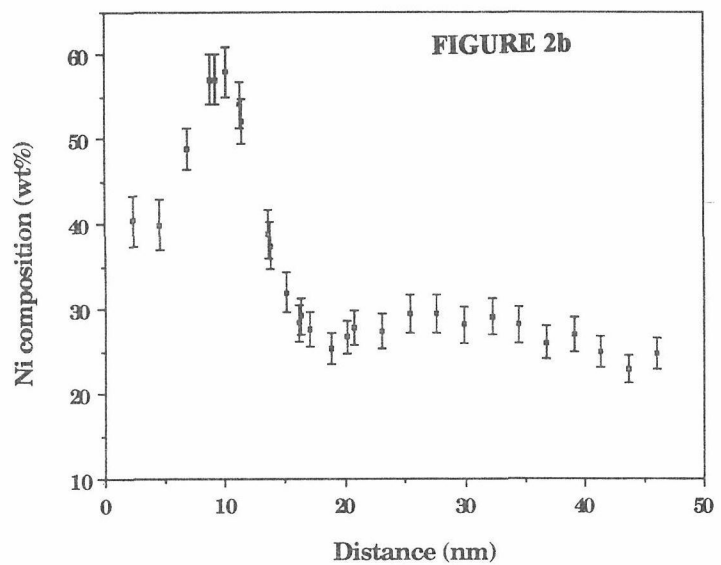
(a) TEM BF image showing thin γ plates (G) in an Fe-Ni foil aged at 300°C for 1 year. The composition profile (b) plots the Ni variation across the atomically-sharp interface, and the profile exhibits a spatial resolution of < 5 nm. Data obtained on a VG HB501 at 100 kV (Courtesy J. Zhang).
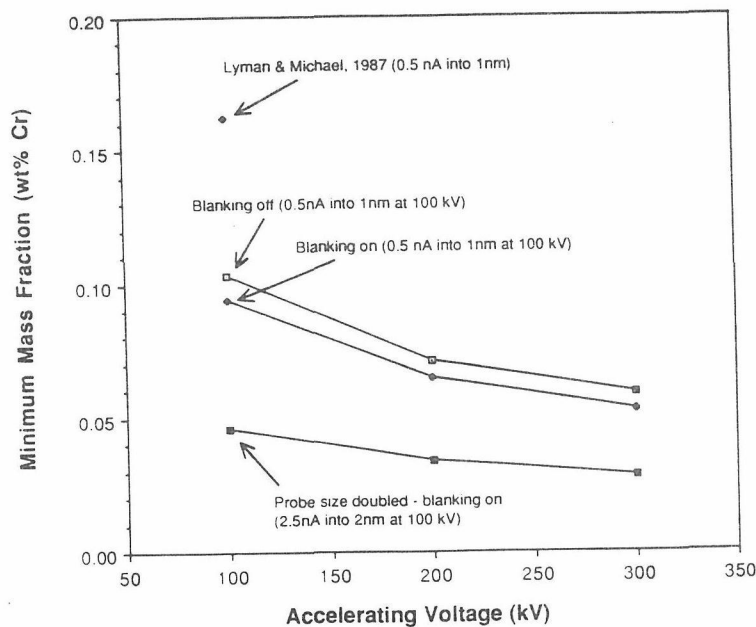
FIGURE 3

Calculated minimum mass fraction for Cr as a function of accelerating voltage, for the VG HB 603. The MMF value of < 0.05 translates to a detectability limit of 3 atoms. (Courtesy C. E. Lyman).

phase equilibria. Amorphous layers at grain boundaries in ceramics have also been characterized. Continued advances in the development of x-ray analysis should permit detection of segregation on a much smaller level, and possibly the detection of trace elements at the < 0.01% (100 ppm) level. This will permit study of such phenomena as Suzuki segregation and Cottrell atmospheres, high-level dopant distributions in semiconductors, and possible study of the initial stages of diffusion-controlled phase transformations such as nucleation and growth and spinodal phenomena.

3. Advances in Electron Energy-Loss Spectrometry

a) Spatial Resolution and Minimum Detectability

Spatial resolution of analysis has not been pursued in EELS to the same extent as in XES because the resolution is not as susceptible to specimen parameters. The resolution in EELS is controlled by the angle of selection of the spectrometer (usually 1-100 mrad) and the probe size, rather than by beam spreading through the specimen. Because of the efficiency of signal collection using parallel EELS, the problem of signal detectability is also of less concern in EELS than XES. Consequently, it has been argued (Leapman and Hunt, 1993) that in virtually all analysis situations, EELS is a more sensitive analytical technique than XES. This conclusion neglects the relative simplicity of signal detection and processing in XES versus the sophisticated signal processing required to extract quantitative data from an EELS spectrum. Furthermore, it neglects to consider that quantitative analysis in EELS requires much thinner specimens (typically < 50 nm) than XES and it may not always be possible to make the specimen thin enough for routine EELS analysis. Nevertheless, it is feasible to contemplate the combination of spatial resolution and minimum detectability from simple geometrical conditions only.

Because of the efficiency of signal collection in EELS, the spectrometer design and interfacing to the microscope do not limit the minimum detectability, as in XES. It is possible to consider the analysis limits from a purely geometrical standpoint. The spatial resolution and minimum detectability are thus a function of the probe diameter, the probe convergence angle (which can be made equal to the spectrometer collection angle) and the specimen thickness. Figure 4a shows calculations of the probed volume of a 20 nm thick pure Si specimen in cubic angstroms and the equivalent number of Si atoms analyzed as a function of the probe diameter (Hunt, 1993). Decreasing the probe convergence angle and the probe diameter result in a smaller volume analyzed. A 1 mrad convergence angle and a 0.5 nm beam can analyze less than 5 Si atoms. Conversely, in figure 4b, where the convergence angle is fixed at 5 mrads and the Si thickness varied, a 5 nm thick specimen permits analysis of a single Si atom with a 0.5 nm beam. Thus it is possible to contemplate single atom analysis and recent progress towards this goal has been demonstrated (Batson, 1993, Muller et al., 1993).

b) Advances in Signal Processing and Data Analysis

Advances in EELS have emphasized data processing and analysis in order to be able to extract more information from the spectrum and maximize the usage of the data gathered at different points in the specimen. The high energy loss portion of the EELS spectrum suffers from the relatively low signal to background ratio, because of the dominance of the plural scattering background intensity when the thickness exceeds several tens of nanometers. Thus it has become necessary to develop first and second difference methods to extract the small peak intensity from the high background. These new processing methods can be combined with the technique of spectrum imaging (Jeanguillaume and Colliex, 1989, Hunt and Williams, 1991) to produce quantitative images of any signal in the EELS spectrum. If a full spectrum is gathered at each pixel in a STEM image, it is then possible to sum the pixels (and the useful spectral information) in a region of interest in the image, thus maximizing the signal intensity from that region.

The low energy loss portion of the spectrum is receiving increasing attention because it does not suffer from the high plural scattering background. The presence of low energy interband transition (see figure 5) enables imaging of different polymers (Hunt, 1993) which would otherwise prove difficult to discriminate without staining. The plasmon peak intensity is extremely high, permitting very accurate determination of its position (Hunt, 1993) as shown in figure 6. The plasmon peak can, on occasions provide quantitative microanalytical data, as well as being a useful fingerprint of the dielectric response of the specimen.

In addition to modeling and fitting the coarse features of the EELS spectrum, there is increased interest in modeling the fine structure. As shown in figure 7, it is possible to make reasonable calculations of the energy-loss near edge structure on a core edge. The near edge

structure contains vital information about the density of states (DOS), which is very sensitive to the bonding state of the ionized atom. The calculated DOS (Rez et al., 1991) show excellent agreement with the energy values of the fine structure, although the intensity of the fine structure is not yet well described. Nevertheless, such modeling promises detailed information on the localized changes in bonding accompanying compositional variations at interfaces, for example.

c) Applications to Materials

The information available depends on what portion of the EELS spectrum is imaged. As already noted, for example it is possible to map out the free electron density from the plasmon peak energy. The free electron density can be related to composition in simple binary free-electron type alloys such as Al alloys. It is possible to map the dielectric constant from the low loss portion of the spectrum. The presence or absence of low energy interband transitions permits discrimination of different polymers without traditional staining methods. The low energy spectrum contains band-gap information, which can reveal fine-scale details in the images of semiconductor devices. The high energy-loss spectrum can be used to map elemental distributions from core edges. Also energy-loss near-edge structure can be used to discriminate regions of different bonding, such as the sp^2 and sp^3 regions of diamond-like carbon films and bonding changes across interphase interfaces are easily discerned, at the nanometer level.

4. Summary

AEM techniques involving both x-ray and electron spectrometry have advanced to the level where spatial resolution limits of a few nanometers are being approached. In combination with this it is proving possible to detect the presence of a few atoms in the analyzed volume. In addition to this high spatial resolution microanalysis and atomic-level sensitivity, the same instruments are capable of direct imaging of single rows of atoms using Z-contrast. Ultimately, therefore AEM can be used to both image and identify the atomic structure of materials. This represents the ultimate goal of the materials scientist in the attempt to relate properties to both the structure and chemistry of the material.

5. Acknowledgments

6. References

Batson, P. E. (1993) Nature, 366, 727.
Cox, C. E., Lowe, B. G. and Sareen, R. A. (1988) IEEE Trans. Nucl. Sci., 35, 28.
DTSA (1991) Office of Standard Reference Data, NIST, Gaithersburg, MD 20899, U.S.A.
Goldstein, J. I., Costley, J. L., Lorimer, G. W. and Reed, S. J. B. (1977) SEM 1, O. Johari, (ed.) 315, IITRI Chicago, IL.
Hunt, J. A. (1993) PhD Dissertation, Lehigh University.
Hunt, J. A. and Williams, D. B. (1991) Ultramicrosc. 38, 47.
Jeanguillaume, C. and Colliex, C. (1988) Ultramicrosc. 28, 252.
Leapman, R. D. and Hunt, J. A. (1991) Microsc. Microanal., Microstruct. 2, 231.
Lyman, C. E. and Michael, J. R. (1987) Analytical Electron Microscopy-1987, D. C. Joy (ed.), 231, San Francisco Press, San Francisco, CA..
Lyman, C. E., Goldstein, J. I., Williams, D. B., Ackland, D. W., von Harrach, S. Nicholls, A. W. and Statham, P. J. (1994) J. Microsc., submitted for publication.
Michael, J. R., Williams, D. B., Klein, C., and Ayer, R. (1990) J. Microsc. 160, 41.
Mott, R. B. and Friel, J. J. (1993) Microbeam Analysis, 2, (Supplement), S 176.
Muller, D. A., Tzou, Y., Raj, R. and Silcox, J. (1993) Nature, 366, 725.
Reed,. S. J. B. (1982) Ultramicrosc. 7, 405.
Rez, P., Weng, X. and Ma, H. (1991) Microsc. Microanal., Microstruct. 2, 143.
Williams, D. B., Michael, J. R., Goldstein, J. I. and Romig, A. D. Jr. (1992) Ultramicrosc. 47, 121.
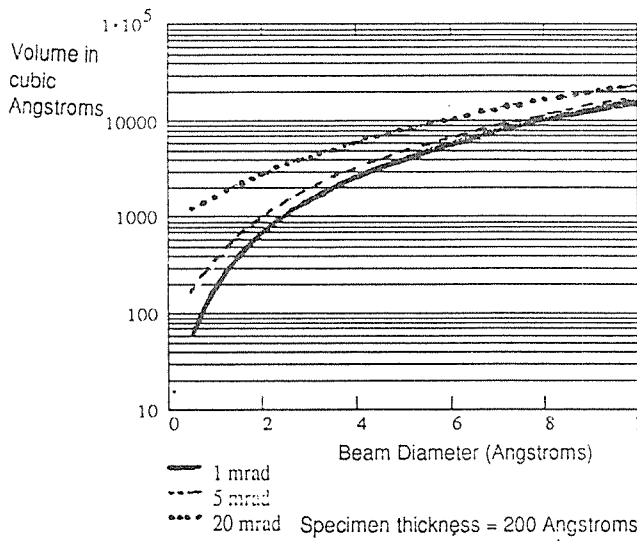
FIGURE 4a
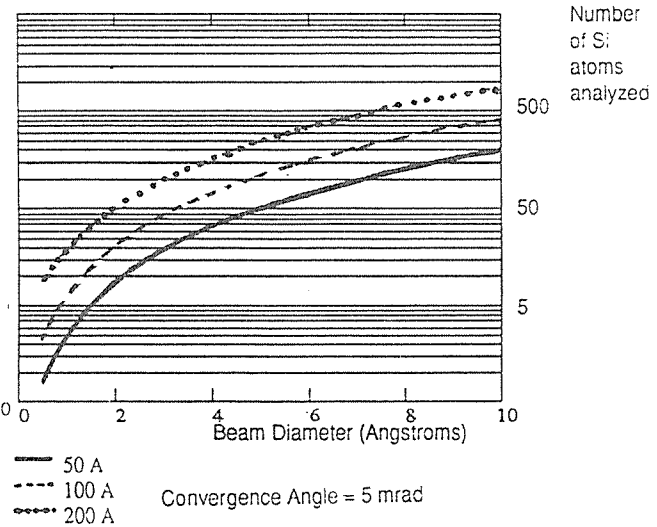
FIGURE 4b

Calculated beam-specimen interaction volume, from purely geometrical considerations for (a) a 20 nm thick Si foil with varying beam convergence angles and (b) a fixed convergence angle and varied thicknesses of Si. In either case, the analysis of < 5 Si atoms is easily achieved. (Courtesy J. A. Hunt).
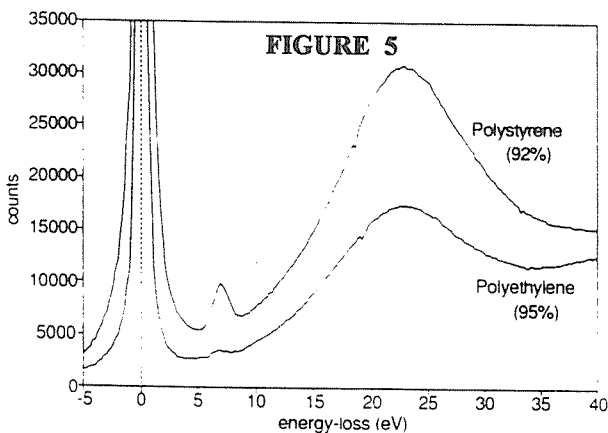
Low-loss spectra from polyethylene and polystyrene showing the presence of a low energy interband transition in polystyrene, that enables discrimination between the two polymers. (From Hunt, 1993).
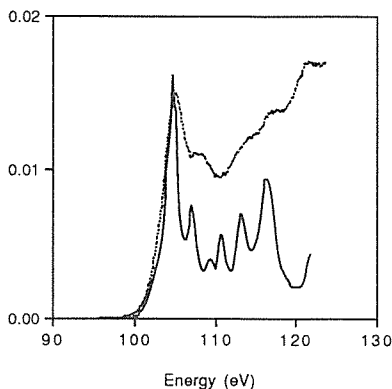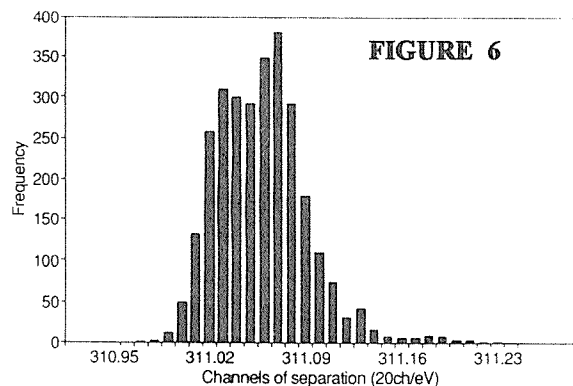
Histogram of the spacing between the zero loss peak and the first plasmon peak position in pure Al. The data are the result of 2883 individual measurements in an Al foil varying in thickness from 15 - 200 nm. From such data the mean plasmon energy Ep can be determined with an error of ~ 3 meV. (From Hunt, 1993).
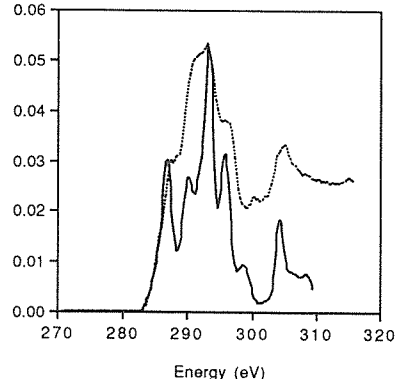
FIGURE 7a

FIGURE 7b

Calculated (dotted lines) energy-loss near edge structure spectra from (a) Si $L_{2,3}$ and (b) C K edges. The energy resolution is ~ 0.5 eV, typical of a FEG AEM. All the main features of the experimental spectra (full lines) are calculated at the correct energy. (Courtesy P. Rez).

Detection of Local Lattice Strains by Convergent-Beam Electron Diffraction (CBED)

Yoshitsugu Tomokiyo

Research Laboratory of High Voltage Electron Microscope, Kyushu University

6-10-1, Higashi-ku, Fukuoka 812, Japan

1.Introduction

Mechanical and physical properties of material depend strongly on microstructures. Structures of interfaces in material play an important role in their properties. Analytical electron microscopy is quite useful for microcharacterization of interfaces in metals, semiconductors, ceramics, superconductors and their composites. As to an analysis of lattice strains, conventional electron diffraction contrast imaging (EDCI) has been used. Quantitative analysis of lattice strain is, however, not easy because strain contrast is sensitive to changes in specimen thickness, the depth of strained region in the specimen and diffraction condition. High resolution electron microscopy (HREM) is not always useful for analysis of lattice strains, because HREM needs very thin specimens and hence the effect of strain relaxation at surfaces can not be neglected. Convergent beam electron diffraction overcomes some of the disadvantages pointed out above and enables us to analyze local lattice strains in crystalline material.

Diffraction lines consisting of higher order Laue zone (HOLZ), which appear in a bright-field disc of CBED pattern, shift sensitively with a change in crystallographic parameters, such as crystal symmetry, lattice spacing, interaxial angles etc. (1). When a defocused large angle convergent-beam is illuminated, a shadow image of the illuminated area appears in a bright-field disc in addition to the diffraction lines (LACBED) as shown in Fig.1. Thus LACBED pattern includes information on both the real and reciprocal lattices (2), while CBED pattern gives information only on the reciprocal lattices. In the present paper, usefulness of the CBED and LACBED in analysis of local lattice strains is demonstrated by applying them to Cu-Al alloys, ZnO varistors and Si devices.

2. HOLZ pattern and lattice parameter

Positions of HOLZ lines in a CBED pattern are very sensitive to a change in lattice parameters. Figure 2 shows how sensitively HOLZ lines shift with a change in lattice parameter. HOLZ patterns in Figs.2a and 2b were taken at 300 and about 100 K, respectively with fixed electron optical conditions. Intersecting points of two HOLZ lines as indicated by arrows apparently change in Figs.2a and 2b on account of a slight change (about 0.05%) in a lattice parameter with temperature. We can determine local lattice parameters by matching an observed HOLZ pattern with the computer simulated one as demonstrated in Figs.3 and 4 (3). When we use the simulation based on the kinematical diffraction, we have to pay special caution to an error originated from neglect of the dynamical effect of diffraction (4). It is recommended to use in the simulation an effective acceleration voltage, Ee in place of an actual voltage of electron microscope. An accuracy of 0.1% is attained in an absolute value of lattice parameter with the kinematical approximation if a proper value of Ee is used. Of course a relative change smaller than 0.1% is easily detected as demonstrated in Fig.2. This method of lattice parameter determination will be applied to estimation of local lattice strains.
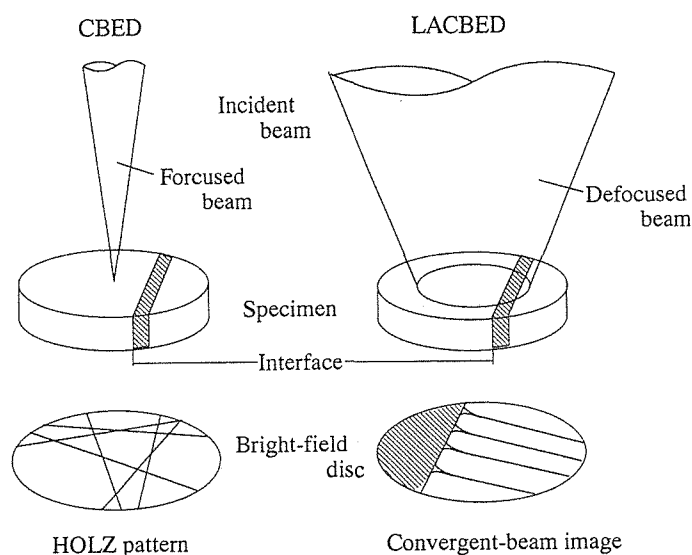
Fig.1 Schematic representation of CBED and LACBED.
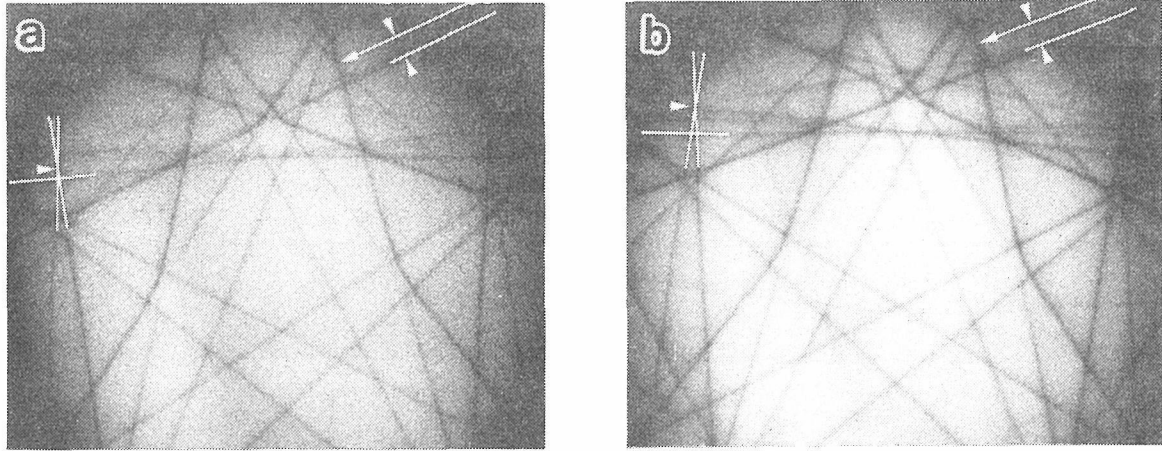
Fig.2 [012] HOLZ patterns of Si showing variation with temperature. (a) 300K, (b) about 100K.

(b)a=0.3626 nm
(c)a=0.3623 nm
(d)a=0.3629 nm
X-ray measure-
ment:0.3629 nm
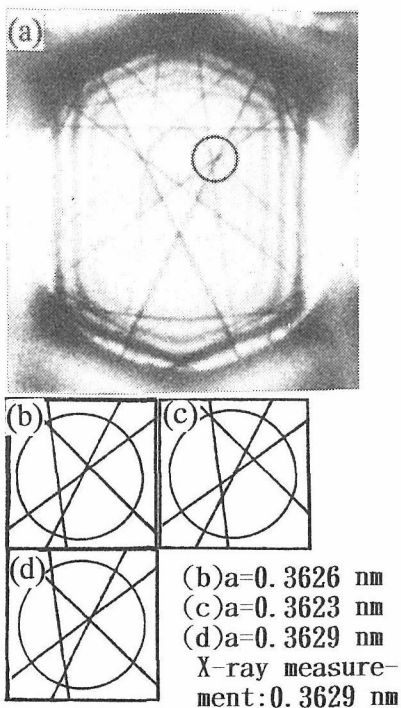
Fig.3 Observed and simulated [114] HOLZ patterns of Cu-5.5at%Ga alloy.
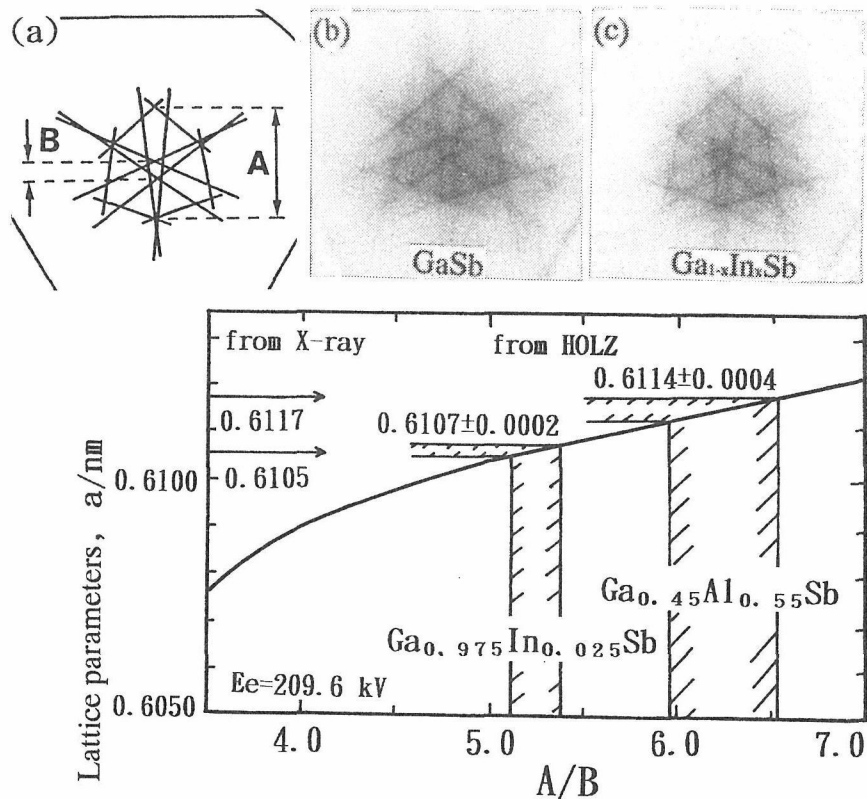
Fig.4 [111] HOLZ patterns of compound semiconductors (upper) and determination of lattice parameters (lower).

3. Lattice strains in Cu-Al alloy

An analysis of coherent lattice strain around a precipitate in an alloy is important in relation to the age-hardening. Figure 5 gives an example of the analysis in a Cu-20at% Al alloy which consists of two phases $\alpha + \alpha_2$; α is a solid solution with an fcc structure, and α_2 is an Al-rich phase of one-dimensional long period supperlattice based on an fcc structure. Figure 5f is taken with the 110 superlattice reflection and consequently α_2 particle with c-axis // [001] appears as bright region, while α_2 particles of other variants are dark. The patterns from dark α_2 particles **a** and **c** indicate the elongation along [100]. The patterns from α-matrix and α_2 with c-axis parallel to [001] should have the mirror symmetry with respect to [22$\bar{1}$] axis. The patterns shown in Figs. 5b, 5d and 5e are , however, slightly distorted. Bright- or dark-field images of EDCI show no strain contrasts but CBED HOLZ patterns apparently show that α_2 phase has tetragonal distortion of c/a=1.004 and lattices of α matrix is slightly strained from a perfect fcc structure near α_2 precipitates (5).

- 41 -
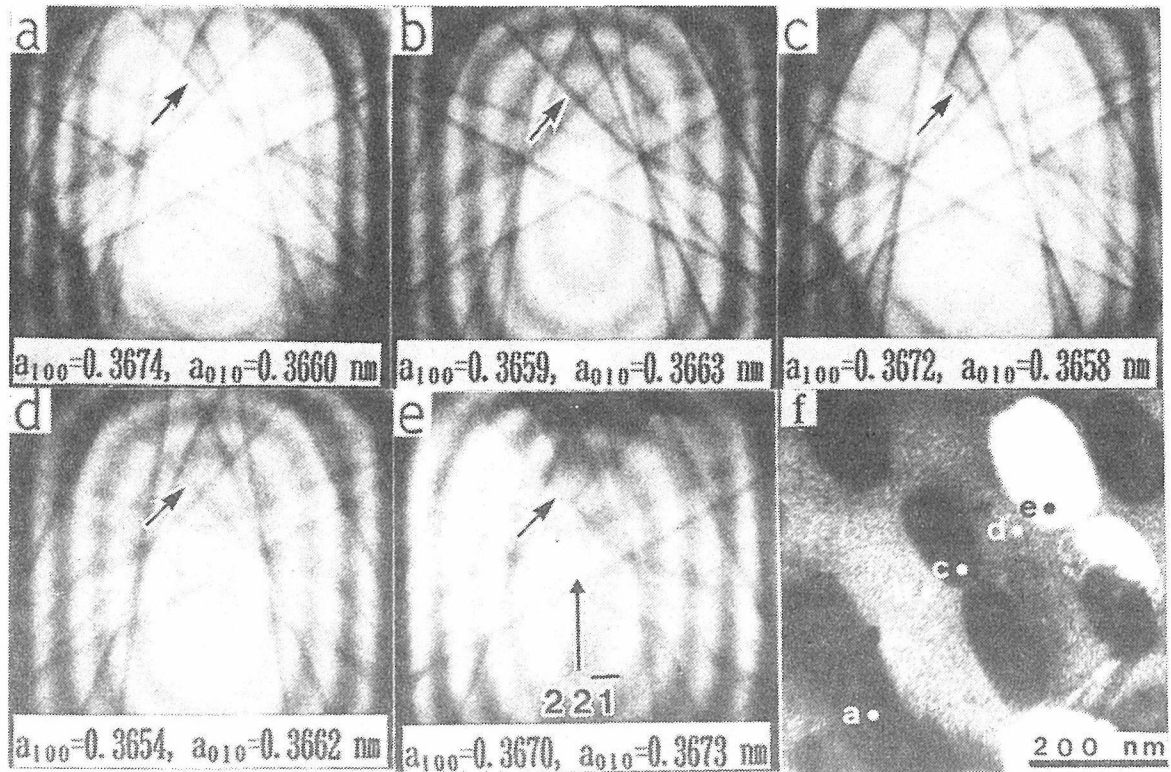
Fig.5 [114] HOLZ patterns (a~e) and dark-field image of Cu-Al alloy. Bright or dark regions correspond to α_2 precipitates of different variants.

4. Lattice strains in ZnO varistor

Properties of sintered ceramics depend sensitively on structures of grain boundaries. One of the typical examples is ZnO-based varistor of which non-ohmic property has been reported to originate from a Schottky barrier formed at a grain boundary. ZnO varistor includes Bi_2O_3 as an essential additive and some other metal oxides to improve the varistor characteristics. According to EDX analysis, Bi_2O_3 hardly dissolve into ZnO grains and persist at grain boundaries although most of Bi_2O_3 concentrates at multiple junctions (6). Bi_2O_3 at the grain boundaries form interfaces between semiconductor ZnO and insulator Bi_2O_3 and hence Schottky barriers.
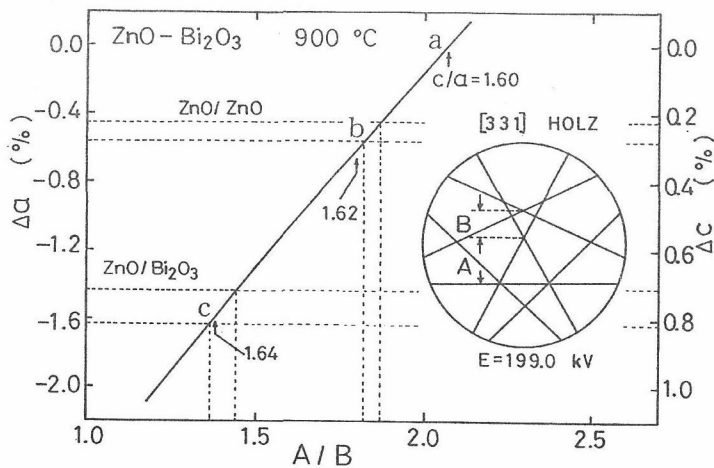
Fig.6 [331] HOLZ patterns obtained from ZnO-Bi2O3 varistor.
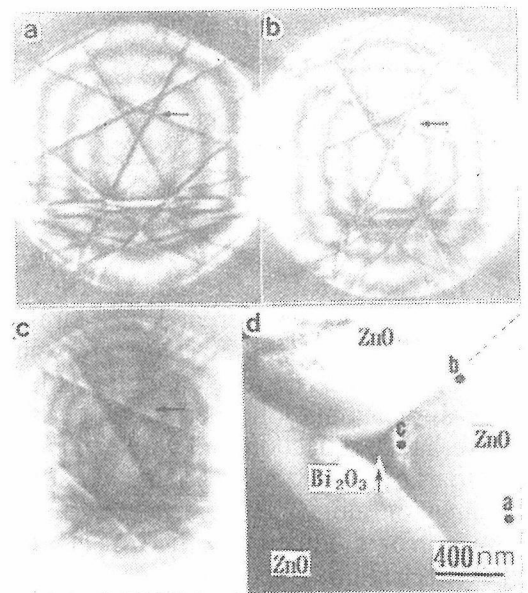
Fig.7 Lattice strains of ZnO and variation of [331] HOLZ patterns given in Fig.6.

Figures 6 and 7 show an example of analysis of lattice strain in ZnO-Bi2O3 varistor. ZnO lattices near the grain boundary and the triple junction are shrunk along an a-axis and elongated along a c-axis compared with a perfect ZnO lattices of wurtzite structure which has an axial ratio of c/a=1.60. The lattice strains along grain boundaries seem to be responsible for the degradation during practical use.

5. Lattice strains in Si wafer

Impurity gettering is one of the important techniques in Si device processes. Poly-Si formed on the back surface of a Si wafer and oxygen precipitates produced in a Si wafer are used as extrinsic and intrinsic gettering, respectively. Since lattice defects and/or lattice strains are used as gettering sinks it is necessary to investigate microstructures near the inter faces between Si and poly-Si, or Si and oxygen precipitate in order to understand the gettering mechanisms.

An oxygen precipitate produced by annealing at 1000 °C is square thin plate having {100} habit planes with <110> sides. An image of a precipitate is shown in Fig.8 where the plate is parallel to an incident beam and penetrating the specimen. Figure 9 gives an example of LACBED pattern taken from the same area as in Fig. 8 . Broadening and bending of diffraction lines show lattice strains around the precipitate. The bending of $\bar{h}h0$ lines turns out to be mainly due to a local lattice rotation and partly due
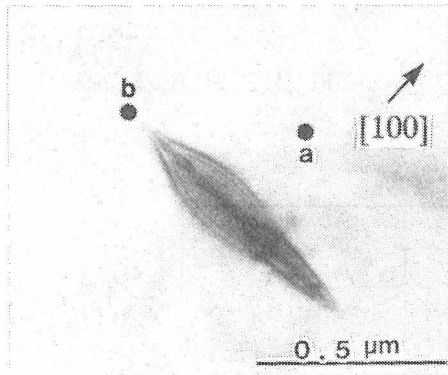
Fig.8 A representative bright-field image of plate-like oxygen precipitate observed along [012] direction.
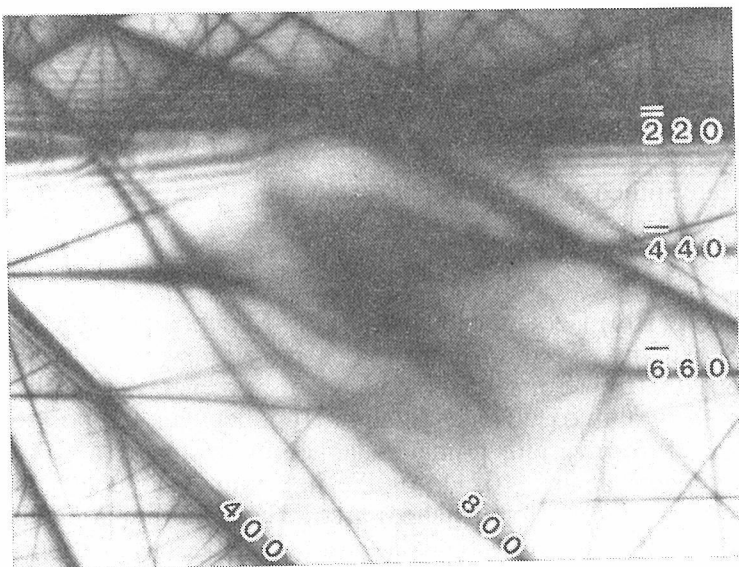
Fig.9 LACBED pattern of the precipitate shown in Fig.8.
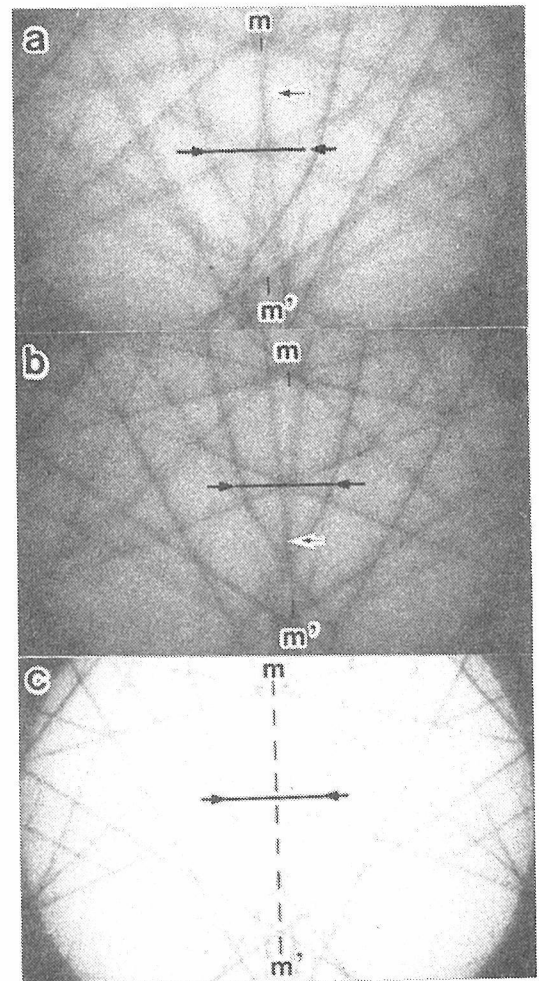
Fig.10 [012] HOLZ patterns taken from points labelled in Fig.12. Pattern (c) is obtained from a strain free region.

- 43 -

to a local shrinkage of the lattice planes. The local lattice rotation is estimated to be about 4.7 mrad at most. Figure 10 shows examples of [012] HOLZ patterns taken from points labelled in Fig.8 and the one from strain free region. It is noticeable in Fig.10 that the intersecting points of two lines as indicated by arrows are shifted to opposite directions in 10a and 10b compared with 10c. This result suggests a difference in signs of lattice strains at point **a** and **b** in Fig.8. The patterns of Figs.10a and 10b hold a mirror symmetry with respect to line mm' suggesting the presence of tetragonal lattice distortion (7). The lattice strains estimated are $\Delta a/a_0 = -0.002 \sim -0.004$ in the vicinity of flat plane of the precipitate, and $+0.002 \sim +0.003$ near the edge of a side plane.
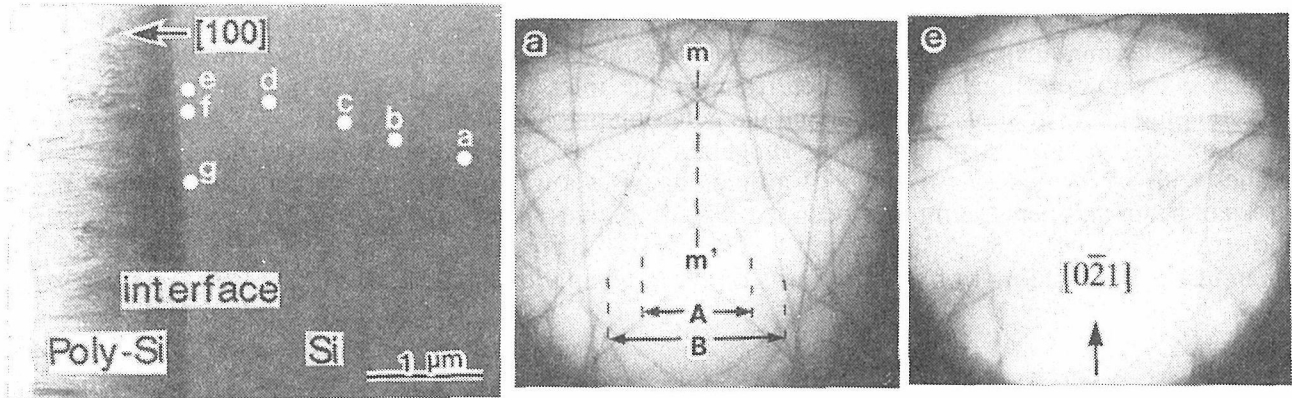
Fig.11 Cross section image of Si/poly-Si interface and [012] HOLZ patterns.
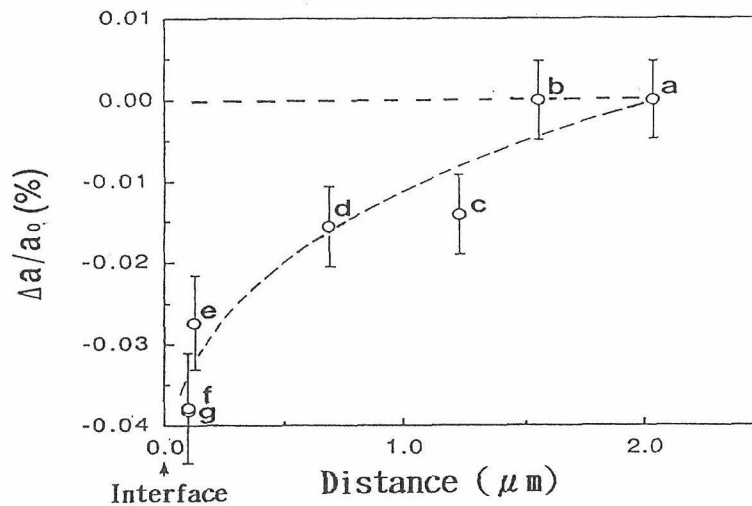
Fig.12 Lattice strain of Si determined as a function of distance from the interface.

A cross section image of the interface between (100) Czochralski Si and poly-Si deposited by CVD is shown in Fig.11 along with [012] HOLZ patterns. Needle-like Si grains are aligned along [100] direction and have an average diameter of about 0.01μm. Some of the grains are, however, partly tilted from [100] by 10~15 degrees. HREM images show thin oxide layer of about 1nm between the poly-Si and (100) surface of CZ-Si. The patterns obtained from various points as lablled in the image (a~g) are similar in appearance and have a mirror symmetry against [0$\bar{2}$1], or the line mm'. However, the distances between intersecting points (A and B in Fig.11a for instance) are different. Comparing the measured A/B with the calculated one we can determine the tetragonal distortion of lattices as a function of distance from the interface as shown in Fig.12. HOLZ patterns obtained in the close vicinity of the interface exhibit splitting of lines as given in Fig.13. The line splitting implies a steep or discontinuous change in interplanar distance or lattice rotation, because gradual change in these parameters will give
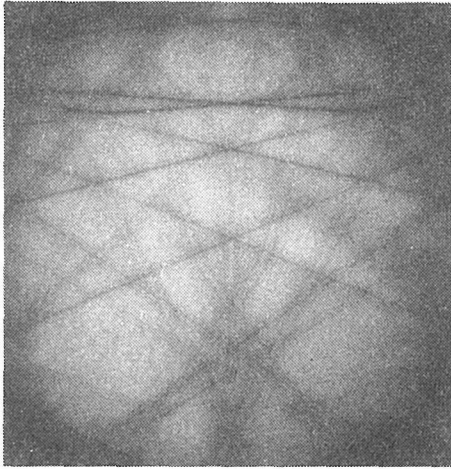
Fig.13 [012] HOLZ pattern obtained from a point distant by 10 nm from the interface. Observed at 160 kV with a probe size of 20 nm.
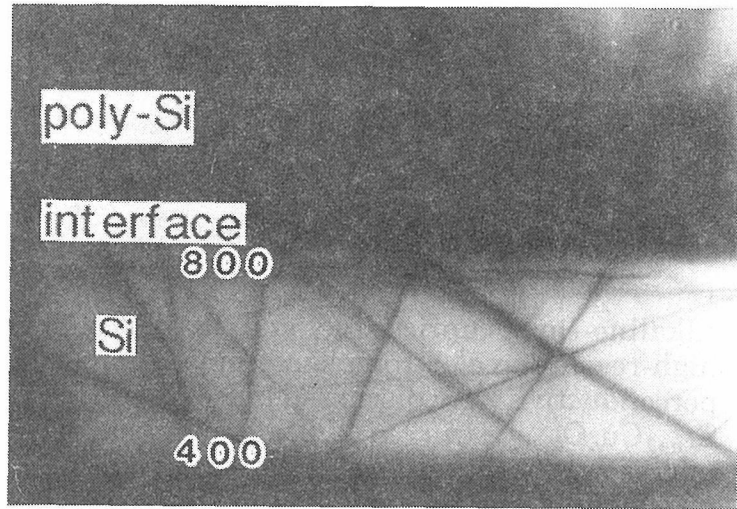
Fig.14 LACBED pattern showing splitting and broadening of lines in the vicinity of the interface.

rise to broadening or bending of HOLZ lines (2). Separations of the split lines depend on angles between HOLZ lines and the line mm' drawn parallel to the interface. Lines almost perpendicular to the interface scarcely split suggesting that an axis of lattice rotation is parallel to the interface. The degree of line splitting turns out to be different if the probed point is changed along the interface. This result corresponds well with a LACBED pattern shown in Fig.14 where splitting of 800 line varies from position to position along the interface (8). Thus the lattice strains of Si substrate seem to depend on growth morphology of poly-Si.

6. Summary

Applications of CBED and LACBED to detection of local lattice strains were demonstrated. CBED enables us to analyze lattice strains quantitatively and to detect small strains that can be hardly detected by the dark-field image of EDCI. LACBED gives us visual information on strain field. A combination of CBED and LACBED with other techniques such as HREM, EDX, EELS and etc. is very powerful for microcharacterization of interfaces. A probe size used in our CBED study is 10~20 nm. A practical probe size, or spatial resolution depend on brightness of electron source. An electron microscope with a field emission gun will give one order of magnitude better spatial resolution.

References
(1)Tanaka M, Terauchi M, and Kaneyama T:Convergent-Beam Electron Diffraction ,Tokyo; JEOL-Maruzen (1988)
(2)Cherns D:Evaluation of Advanced Semiconductor Materials by Electron Microscopy, Ed, Cherns D, Plenum Press, New York and London (1988)
(3)Tomokiyo Y, Okuyama T, Matsumura S, Kuwano N, and Oki K:Materials Trans Jpn. Inst. Metals, 31(1990)641-646.
(4)Okuyama T, Matsumura S, Kuwano N, Oki K, and Tomokiyo Y: Ultramicroscopy, 31(1989)309-318.
(5)Okuyama T, Matsumura S, Tomokiyo Y, Kuwano N, and Oki K:Inst. Iron Steel Jpn. Int.,29(1989)191-197.
(6)Suyama Y, Tomokiyo Y, and Terasaka K:Proc. 12th Int. Cong. on Electron Microscopy, Seattle, USA, Vol.4, (1990)374-375.
(7)Okuyama T, Sadamitsu S, Sumita S, Shigematsu T, and Tomokiyo Y:Proc. 10th European Cong. on Electron Microscopy, EUREM92, Granada, Spain, Vol.2, (1992)157-158.
(8)Tomokiyo Y, Nakashima J, Fujimoto T, and Okuyama T:Proc. 7th Japanese-Chinese Electron Microscopy Seminar, Zhangjiajie, China, (1993) in press.

High-Pressure Synthesis and HRTEM Characterization of Oxide Superconductors

Z. Hiroi

Institute for Chemical Research, Kyoto Univ., Uji, Kyoto-fu 611, Japan

Alkaline-earth cupric oxides stabilized at high pressure of 6 GPa are studied by means of high-resolution electron microscopy. Microstructures and their relevance to high-T_c superconductivity are discussed in two families of superconductors, $(Ca_{1-y}Sr_y)_{1-x}CuO_{2-z}$ and $Sr_{n+1}Cu_nO_{2n+1+\delta}$ (n = 1, 2, 3, ...). Particularly in the former, high-resolution electron microscopy observations reveal that planar defects randomly introduced into the infinite-layer structure gives rise to superconducting carriers in CuO_2 sheets. Modulated structures found in $Sr_2CuO_{3+\delta}$ (n = 1) are also reported.

1. Introduction

High-pressure (HP) synthesis is a powerful means to reach novel materials. When heat-treated under high pressure of several GPa, dense compounds with unusual structures and compositions often form as a result of a decrease in free energy of $\Delta F \sim P\Delta V$. Another advantage of this method is the increase of melting temperature which may prevent a sample from dissolving at higher temperatures before a hidden new compound appears. The importance of the HP synthesis method in searching for a new high-T_c superconductor has been recently recognized by several groups. Key structure for high-T_c superconductivity is so-called infinite-layer (IL) structure (Fig. 1(a)) only seen in $Ca_{0.86}Sr_{0.14}CuO_2$ at ambient pressure, which is based on the infinite stacking of CuO_2 sheets separated by alkaline earth (A) atoms [1]. Takano *et al.* found that under high
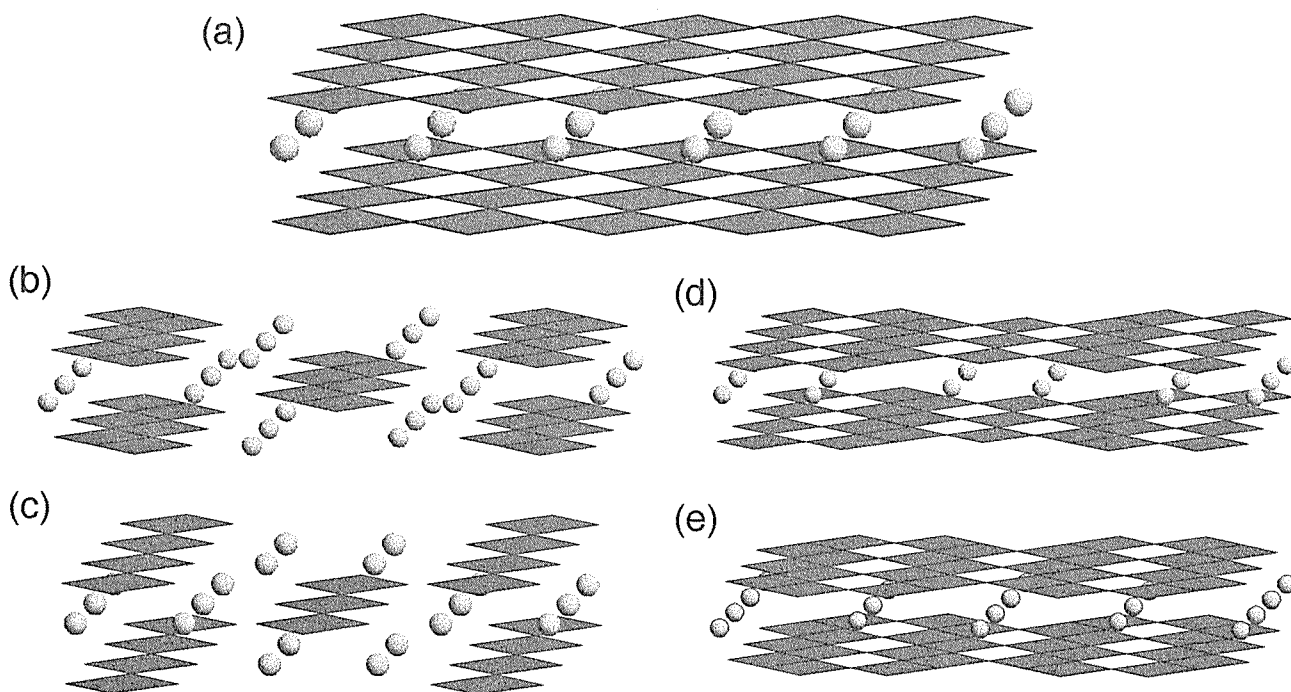
Fig.1 Schematic drawings of the crystal structures of the strontium cupric oxides stabilized at ambient pressure (AP) and high pressure (HP); (a) $SrCuO_2$ (HP), (b) $SrCuO_2$ (AP), (c) Sr_2CuO_3 (AP), (d) $Sr_4Cu_6O_{10}$ (HP), and (e) $Sr_2Cu_4O_6$ (HP). The squares represent CuO_4 polyhedra and the spheres Sr atoms.

pressure of 6 GPa the IL structure becomes stable for a wide range of A composition, just as the perovskite structure does in other complex metal oxides [2]. This opened the possibility to choose various counter layers unacceptable at normal condition which should be intergrown with IL-type layers or just CuO_2 sheets and work as a charge reservoir. The following HP studies brought several new types of superconductors in the A-Cu-O system [3-5], the Hg system [6], and the oxycarbonate system [7].

We have concentrated on the alkaline-earth cupric oxide system and found several new HP phases. The crystal chemistry is so interesting there, because Cu-O polyhedra always form only a square plane, not a square pyramid nor an octahedron as ordinary seen in other complex cuprates, and various simple ways of their networking appear as typically illustrated in Fig. 1. More interesting is their structural evolution as a function of pressure. One dimensional Cu-O chains like the zigzag chains in $SrCuO_2$ (b) or the single chains in Sr_2CuO_3 (c) are characteristic in the ambient-pressure phases, whereas in the high-pressure form always appear two-dimensional Cu-O sheets like the CuO_2 sheets in $SrCuO_2$ (a), the Cu_3O_5 sheets in $Sr_4Cu_6O_{10}$ (d), and the Cu_2O_3 sheets in $Sr_2Cu_4O_6$ (e). Another ambient-pressure phase $Sr_{14}Cu_{24}O_{41}$ which is also stable in an oxidizing atmosphere at high pressure (not shown in Fig. 1) possesses an intermediate structure consisting of edge-sharing Cu-O chains and corrugated Cu_2O_3 sheets similar to that of $Sr_2Cu_4O_6$. This tendency is understood by considering that a tight and short Cu-O-Cu bonding is increased in number with increasing dimensionality, which results in a dense packing preferable at high pressure.

High-resolution transmission electron microscopy (HRTEM) is a superior technique which can provide straightforward information on the crystal structure of unknown compounds. It enables us to construct a reasonable structural model which should be tested by following refinement techniques using X-ray and neutron diffractions. Perovskite related compounds like cupric oxide superconductors are particularly a good target to be observed by using HRTEM, because each metal-atom column along the [100] direction is easily visualized by itself in an ordinary 200 kV-class electron microscope with 2 Å resolution.

In this letter, we report our HRTEM study on the alkaline-earth cupric oxide superconductors stabilized under high pressure

2. Experimental

Samples were prepared at 6 GPa and ~ 1173 K using a classical cubic-anvil-type apparatus, starting from a mixture of some ambient phases with an appropriate composition [8]. To provide an oxidizing atmosphere $KClO_4$, which releases oxygen on heating, was added to the capsule or mixed with the starting powder. HRTEM observation was carried out with a JEOL-2000EX microscope equipped with a top-entry goniometer stage ($C_s = 1.2$ mm) operated at 200 kV. Specimens were prepared by dispersing crushed particles on microgrids. Special care was taken to observe HRTEM images, because some samples were easily damaged by the electron beam irradiation.

3. Results and Discussion
3.1 HP phases in the Sr-Cu-O system

Phase relation at ambient and high pressure of 6 GPa is schematically shown in Fig. 2. Under high pressure without applying high oxygen pressure at least two compounds and one homologous series exist. Orthorhombic Sr_2CuO_3 with the chain structure (Fig. 1(c)) survives, while in the case of $SrCuO_2$ pressure induces a structural transformation to the tetragonal IL structure. On the Cu-rich side the serial phases, $Sr_{n-1}Cu_{n+1}O_{2n}$ ($n = 3, 5, ...$), are formed [9], which do not exist at ambient pressure. They are all semiconductors without conducting carriers. In contrast two kinds of metallic (and superconducting) phases appear by the application of high-oxygen pressure simultaneously. One is a slightly modified infinite-layer type phase which becomes supercon-

$n = 1$ 2 3 4 High pressure & High oxygen pressure

$Sr_{n+1}Cu_nO_{2n+1+\delta}$ $Sr_{1-x}CuO_2$

9 7 5 3 = n High pressure (~ 6 GPa)

$SrCuO_2$ $Sr_{n-1}Cu_{n+1}O_{2n}$

Ambient pressure

Sr_2CuO_3 $SrCuO_2$ $Sr_{14}Cu_{24}O_{41}$

0.3 0.4 0.5 0.6 0.7 Cu / (Sr+Cu)
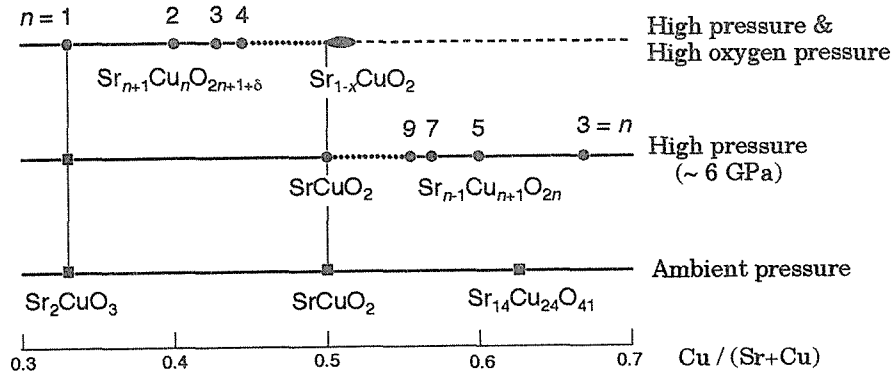
Fig.2 Phase relation in the Sr-Cu-O system.

ductive at $T_c = 100$ K [3]. Another is homologous series of compounds with the formula $Sr_{n+1}Cu_nO_{2n+1+\delta}$ ($n = 1, 2, 3, ...$) extending from $Sr_2CuO_{3+\delta}$ ($n = 1$) to $SrCuO_2$ ($n = \infty$) whose T_c is 70 K (n = 1) and 100 K (n = 2, 3) [4].

3.2 Infinite-layer type phase

Superconductivity in the IL-type phase was first reported with $A = $ (Sr, Ba) and next with $A = $ (Ca, Sr) with a maximum T_c of 110 K. It was suggested from careful examinations of the preparation condition and its relation to the superconducting volume fraction that it was of p-type, with carriers arising from A-ion deficiency. It is very much important to elucidate how carriers are doped and what determines T_c, because the IL structure is believed to be an ultimate structure to reach the highest T_c.

Superconductivity in $(Ca_{0.3}Sr_{0.7})_{0.95}CuO_{2-z}$ have been found to strongly depend on the atmosphere during the heat treatment under pressure. The sample treated in the oxidizing atmosphere shows a large diamagnetic signal with an onset temperature of 110 K, while, in striking contrast, the one treated in the inert condition does not show any trace. On the other hand, the sample treated in a reducing atmosphere suggests the occurrence of a superconducting transition at $T_c \sim 40$ K. These experimental results thus strongly suggest that superconductivity changing from p-type to n-type through a semiconducting state is realized in the present system depending upon oxygen content.

In spite of the observed dramatic change in physical properties the XRD measurements did not tell any significant changes in their patterns correspondingly. Only noticed in common was the peak broadening which was index-dependent, slight for ($hk0$) peaks and serious for (00l) peaks. In agreement with this, electron diffraction (ED) spots were streaked along the c^* axis (insets, Fig. 3). HRTEM revealed the origin of the broadening and streaking: Planar defects were inserted in the parent IL structure in a fairly random way. Figure 3 shows a typical electron micrograph of $(Ca_{0.3}Sr_{0.7})_{0.95}CuO_{2-z}$ treated in the reducing condition. It is a cross-sectional view of the layered structure, and the bright-dot rows running horizontally (marked with arrows) correspond to the projection of the defect layers. Surprisingly, there is almost no tendency that they become ordered to form an $a \times a \times nc$-type superlattice. The interval n, the number of successive Cu-O sheets, is scattered from 5 to a few tens in the image, or more depending upon the area examined. The ED pattern in the inset reveals a streaking along the c^* axis arising from the random distribution of the planar defects. However, the strong fundamental spots guarantee that the IL-type stacking is preserved throughout the crystal. The average defect-layer density seems to increase with increasing A deficiency, and, at the same time, the Meisnner fraction increases. Therefore, it has been considered that A-ion vacancies are not distributed randomly but tend to be concentrated in the defect layers and that these work as a source of carriers. It is probable that the concentration

of the A vacancies within one defect layer is constant, and, thus, the increase simply results in a linear increase of defect-layer density. The defect-layer structure is necessary but not enough for the emergence of superconductivity, because it has been detected independently of atmosphere during the high-pressure treatment.

In order to obtain further information on the mechanism of carrier doping, we performed HRTEM observations of the defect layers. HRTEM is the only means to be applied to such a disordered sub-structure. Figure 4 shows a HRTEM image of the defect layers obtained from the reduced sample. The incident electron beam is parallel to the b direction, giving a cross-sectional atomic view of the layer stacking. The defect layers correspond to the bright-dot rows marked with arrows in the image. Since it was taken under conditions near the Scherzer defocus, a dark dot can be directly interpreted as an atomic column along the incident beam. A computer image simulation of the simple IL structure using the multi-slice method tells that the position halfway between two Cu sites neighboring along the c-axis is always brightest, reflecting the absence of oxygen ions within the A-ion sheet. One can thus determine A and Cu sites without ambiguity as marked in the image. It is thus clear from the image that the $CuO_2/A/CuO_2$ stacking sequence characteristic of the IL structure is basically preserved all over the image.

Concerning the defect-layers, two important indications have been obtained. One is that the central sheet including the brightest-dot row is apparently a Cu-O sheet. Moreover, the sheet is not any more a CuO_2 sheet but a $CuO_{2-\delta}$ sheet having a considerable amount of oxygen vacancies, because its oxygen site is much brighter than that of the other normal CuO_2 sheets. Comparison between two images taken from the oxidized and the reduced samples revealed that the oxygen site was much brighter in the reduced sample, suggesting a larger amount of oxygen vacancies. Another interesting finding from the image of Fig. 4 is that triple Cu-O sheets involved in each defect layer have an elongated intersheet distance of about 3.7 Å, longer by 10 % in comparison with the
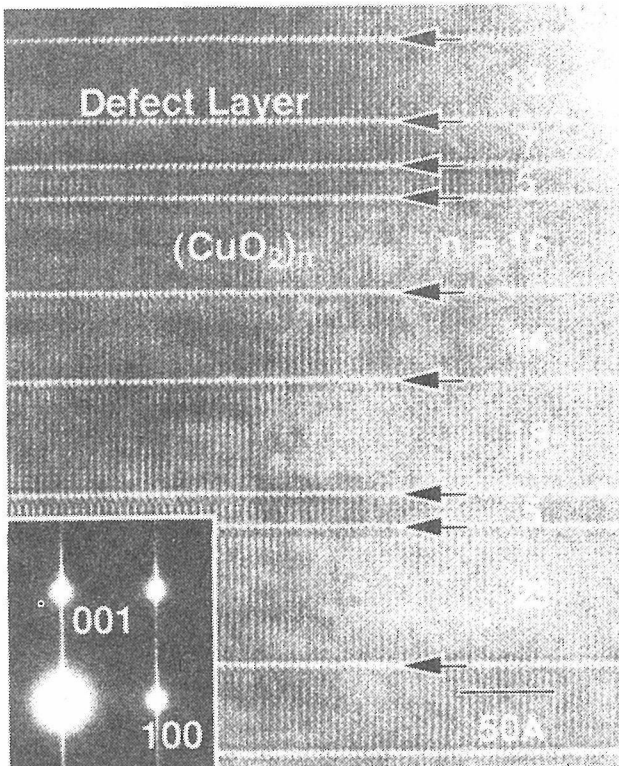
Fig. 3 Lattice image and the corresponding ED pattern of superconducting IL phase, $(Ca_{0.3}Sr_{0.7})_{0.95}CuO_{2-x}$.
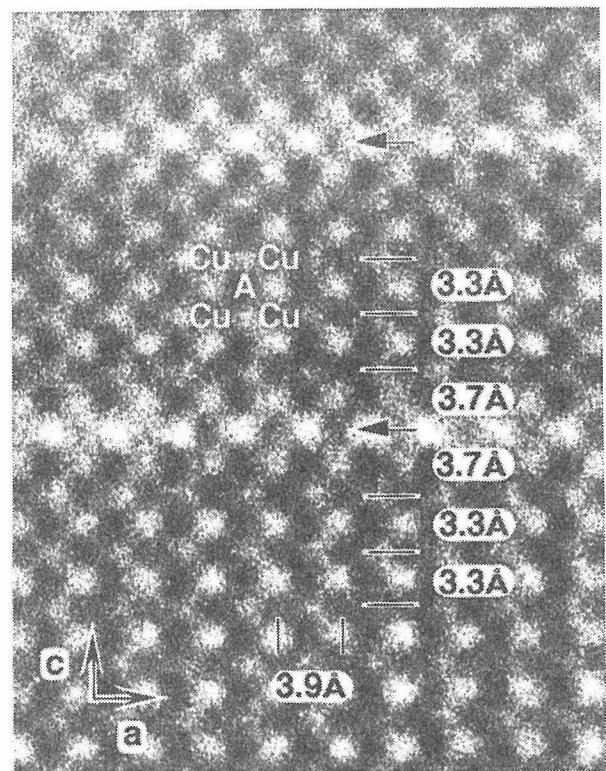
Fig. 4 HRTEM image of a planar defect. Small and large dark dots correspond to Cu and A ions.

normal distance. It is reasonable to assume that the inter-CuO_2-sheet distance is elongated if the bridging A ions are partly deficient in the defect layer. A possibility that a small amount (a few tens of %) of extra oxygen atoms are incorporated into the couple of A-atom sheets might not be ruled out. A HRTEM image taken with the 2 Å resolution can not detect them if they should exist.

Structural characteristics of the superconducting IL phase are summarized as follows. It has basically the IL-type layer stacking but includes defect-layers probably formulated as $A_{1-\alpha}/CuO_{2-\delta}/A_{1-\alpha}$. Their distribution is almost random: The number of successive CuO_2 sheets between adjacent defect layers is scattered between several and several tens. The only one notable modification in microstructure leading to the drastic change in physical properties is oxygen content of the $CuO_{2-\delta}$ sheet in the defect layer. The oxygen deficiency and the A-ion deficiency compensate their charges each other. The neutrality $\delta \approx 2\alpha$ must be preserved when the sample is synthesized in the inert atmosphere, while a hole-creating qualification $\delta < 2\alpha$ must be met for the oxidized sample and an electron-creating one $\delta > 2\alpha$ for the reduced sample.

3.3 $Sr_{n+1}Cu_nO_{2n+1+\delta}$

Another phases stabilized under high pressure and high-oxygen pressure are $Sr_{n+1}Cu_nO_{2n+1+\delta}$. Well-known in crystal chemistry is the Ruddlesden-Popper series, $A_{n+1}M_nO_{3n+1}$ with, e. g., A = Ca, Sr, Eu and M = Mn, Ti, whose end members crystallize in the K_2NiF_4 ($n = 1$) and perovskite structures ($n = \infty$). The present series of cuprates can be considered as an oxygen-deficient version of the R-P series with two end members of $Sr_2CuO_{3+\delta}$ ($n = 1$) and IL-$SrCuO_2$ ($n = \infty$). $Sr_2CuO_{3+\delta}$ and $Sr_3Cu_2O_{5+\delta}$, ($n = 2$) show superconductivity at T_c's of 70 K and 100 K, respectively.

The metal sublattice of $Sr_2CuO_{3+\delta}$ is of the tetragonal K_2NiF_4-type (or the Nd_2CuO_4-type, equivalently). The pressure modifies the oxygen sublattice to induce a transformation from orthorhombic Sr_2CuO_3 with single Cu-O chain (Fig. 1(c)) into tetragonal $Sr_2CuO_{3+\delta}$ with Cu-O sheets. A unique feature of this phase is that nearly a half of the oxygen atoms are missing from the K_2NiF_4 structure. This large amount of oxygen vacancy induces structural instability and gives rise to two dimensionally modulated structures with supercells of $4\sqrt{2}a \times 4\sqrt{2}a \times c$ ($\delta \sim 0.1$) and $5a \times 5a \times c$ ($\delta \sim 0.2$).

Figures 5 show the ED patterns and the lattice images of $Sr_2CuO_{3.1}$ (a) and $Sr_2CuO_{3.2}$ (b) taken with the [001]* incidence. Intense fundamental spots of the K_2NiF_4 type in each case are dressed with two dimensional arrays of satellite spots whose intensity decreases monotonically with the order, characteristic for a modulated structure.
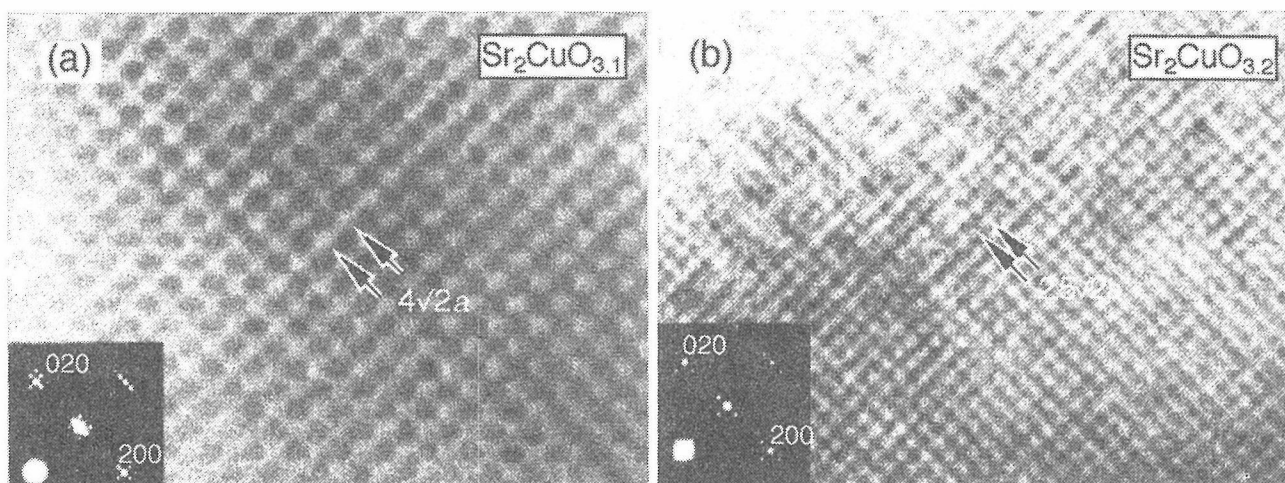
Fig. 5 Modulated structures of $Sr_2CuO_{3+\delta}$; (a) $4\sqrt{2}a \times 4\sqrt{2}a \times c$ for $\delta \sim 0.1$ and (b) $5a \times 5a \times c$ for $\delta \sim 0.2$.
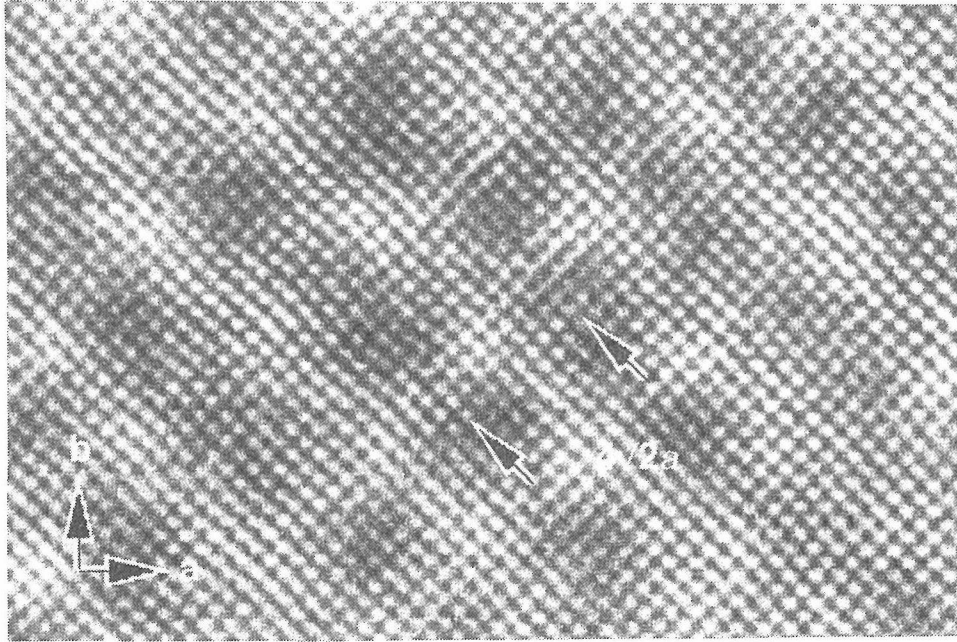
Fig. 6 HRTEM image of the modulated structure of $4\sqrt{2}a \times 4\sqrt{2}a \times c$. Note that the atomic rows along the <110> directions are not straight but wavy, suggesting a formation of a displacive modulation.

The superlattices are commensurate, $4\sqrt{2}a \times 4\sqrt{2}a \times c$ (a) and $5a \times 5a \times c$ (b). Incommensurate periodicities were also observed at intermediate oxygen contents. The images correspondingly represent that two orthogonal waves of contrast along the <110> direction of the K_2NiF_4 structure are overlapped on the fundamental lattice fringes. The HRTEM image of Fig. 6 indicates that the atomic rows along <110> are not straight but wavy to form a sinusoidal transverse wave with unusually large amplitude of more than 0.2 Å. The origin should be related to the ordering of large amount of oxygen vacancies, because the periodicity reduces from $4\sqrt{2}a$ at $\delta \sim 0.1$ to $2.5\sqrt{2}a$ at $\delta \sim 0.2$, keeping essential features unchanged. Details will be reported elsewhere.

Other members of $Sr_{n+1}Cu_nO_{2n+1+\delta}$ have not yet been isolated at the present stage. The $n = 2$ and 3 members were identified as macroscopic phases by XRD measurements, while others with $n \geq 4$ was observed on an electron microscopic level. $Sr_3Cu_2O_{5+\delta}$ crystallizes in a tetragonal structure of $I4/mmm$ with $a = 3.9$ Å and $c = 21.0$ Å, which is isomorphous with those of $La_2SrCu_2O_6$ and $Sr_3Ti_2O_7$.

References
1. T. Siegrist, S. M. Zahurac, D. W. Murphy, and R. S. Roth, Nature 334 (1988) 231.
2. M. Takano, Y. Takada, H. Okada, M. Miyamoto, and K. Kusaka, Physica C 159 (1989) 375.
3. M. Azuma, Z. Hiroi, M. Takano, Y. Bando and Y. Takeda, Nature 356 (1992) 775.
4. Z. Hiroi, M. Takano, M. Azuma, and Y. Takeda, Nature 364 (1993) 315.
5. M. G. Smith, A .Mnthiran, J. Zhou, J. B. Goodenough and J. T. Markert, Nature 351 (1991) 549.
6. O. Chmaissem, Q. Huang, E. V. Antipov, S. N. Putilin, M. Marezio, S. M. Loureiro, J. J. Capponi, J. L. Tholence and A. Santoro, Physica C 217 (1993) 265.
7. T. Kawashima, Y. Matsui, and E. Takayama-Muromachi, Physica C, in press.
8. Z. Hiroi, M. Azuma, M. Takano, and Y. Takeda, Physica C, 208 (1993) 286.
9. Z. Hiroi, M. Azuma, M. Takano, and Y. Bando, J. Solid State Chem. 95 (1991) 230.

Polytypism in the Hg-Ba-Ca-Cu Oxide System

M. Cantoni, H.-U. Nissen, A. Schilling and H.R. Ott

Solid State Physics, ETH Hönggerberg, CH-8093 Zürich, Switzerland

1. Introduction

After the discovery of the Hg-oxide superconductor with the composition $Hg_1Ba_2CuO_{4+x}$ (Hg-1201) [1], which has a critical temperature T_C of 94K, an attempt was made to introduce Ca or Y atoms in order to obtain members of a new series of oxides with the general chemical composition $Hg_1Ba_2M_{n-1}Cu_nO_{2n+1+x}$ (M=Ca,Y) [2,3]. Since a structurally analogous series with the element Tl instead of Hg was already known to contain members with very high values of T_C [4-6], the existence of a series of superconductors with isotypic structures was assumed. In these experiments the runs including Ca resulted in superconducting fine-grained samples containing up to six different crystal phases. Energy dispersive X-ray microanalysis (EDX) on a 300kV transmission electron microscope (Philips CM30) showed that, besides several non-superconducting materials such as CuO, $BaCuO_2$ and $CaCuO_2$, a number of Hg-Ba-Ca-Cu oxide compounds could be recognized. High resolution transmission electron microscopy showed that these Hg-oxides contained layered structures which are members of the expected series: Hg-1212, Hg-1223, Hg-1234 and Hg-1245 (Fig. 1). The latter two were only found as individual slabs of one unit cell thickness [2,3].

The present paper attempts to describe in detail the special structural features observed in the set of Hg-layer-structures of these specimens which are characterized by complicated stacking phenomena. Detailed measurements and an interpretation of the bulk physical properties have previously been reported [7].

Fig. 1:

schematic drawing
of the known members
of the Hg-12(n-1)n
homologous series
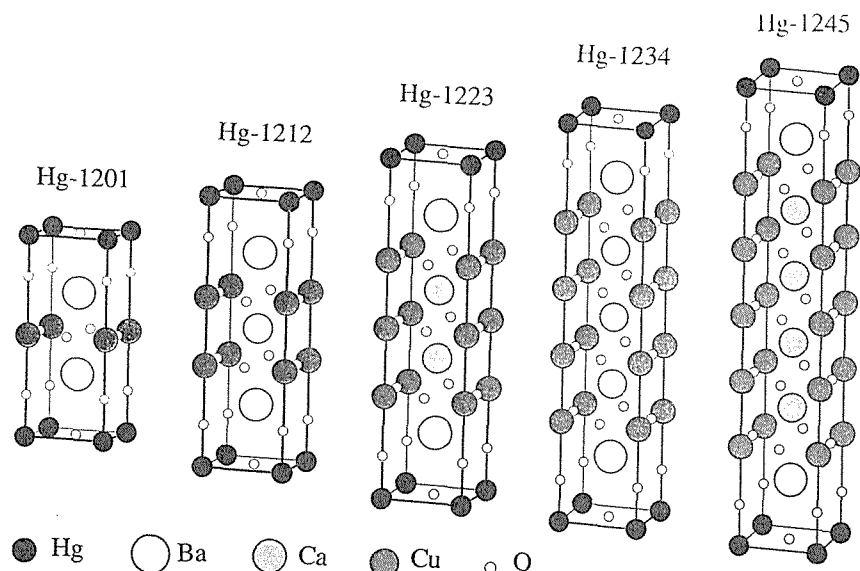
2. Experimental

The specimens having bulk composition $Hg_1Ba_2Ca_1Cu_2O_x$, $Hg_1Ba_2Ca_{1.5}Cu_{2.5}O_x$, $Hg_1Ba_2Ca_2Cu_3O_x$ and $Hg_1Ba_2Ca_3Cu_4O_x$ were synthesized using the procedure described in ref. [2]. For HRTEM work, conventional preparation techniques (powder technique or ion thinning) were applied. The necessary image contrast calculations were executed using the EMS program package [8].

3. Results

Investigations of specimens with the above-mentioned four bulk compositions revealed the presence of two pure phases of the Hg-series, i.e. the Hg-1212 and the Hg-1223 structures. In the electron microscope these two phases were found to be virtually free of defects, and they did not contain any superstructure. Fig. 2 presents a high resolution transmission electron micrograph of the Hg-1223 phase and the corresponding dynamical contrast calculation for two different defocus values. The models used for our calculations were derived from the corresponding structural members of the Tl-cuprate series. By contrast to the Tl-cuprates, no phases with a double layer of Tl (Tl-22(n-1)n) were found. In a few grains of the Hg-1223-phase isolated single unit layers corresponding to Hg-1234 and Hg-1245 were found as intercalations (Fig. 3). Careful analysis of these layers by HRTEM showed that these intercalations were always combined with a single unit cell layer of the Hg-1212 structure (Fig. 4).
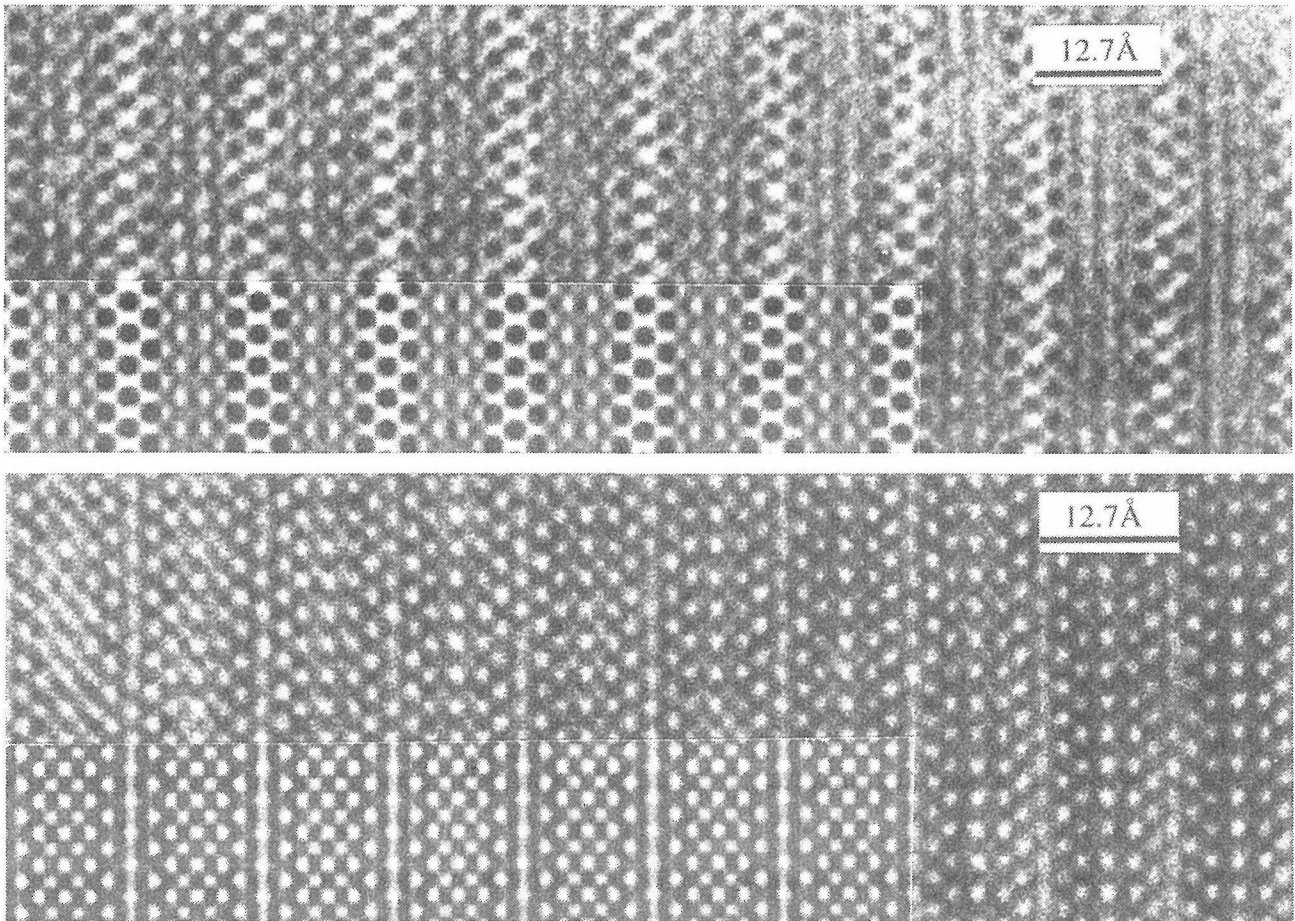
Fig. 2: Experimental HRTEM images of the [100]-pole of Hg-1223, with contrast simulations inserted. Defocus settings were -37nm (upper) and -77nm (lower), Cs=1.1mm, 300keV
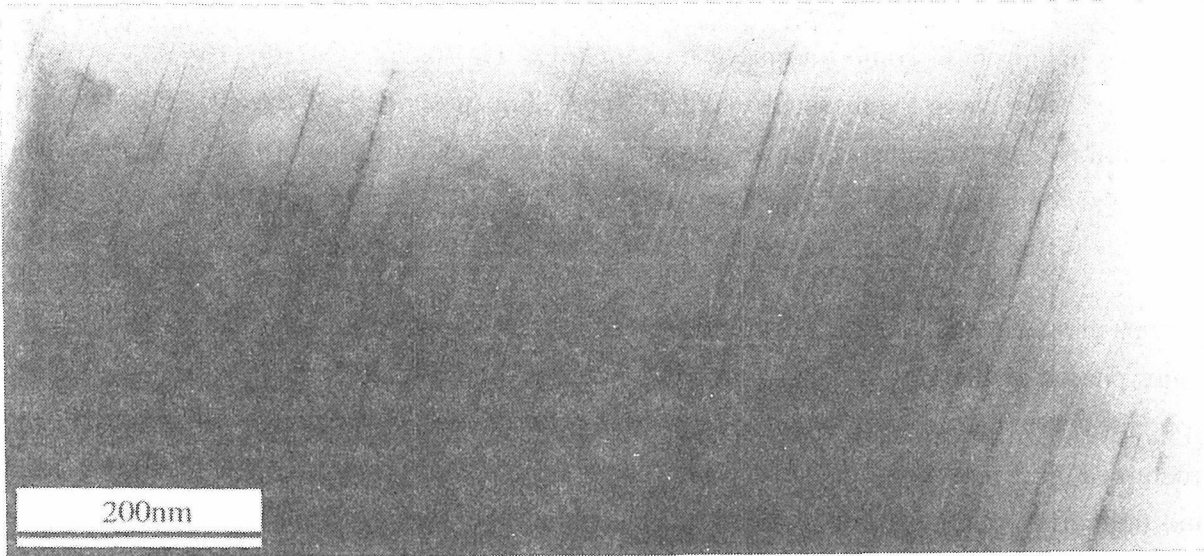
Fig. 3: Bright field image of a single grain of Hg-1223. Stacking defects appear as dark lines.

| 3 | 3 | 3 | 4 | 2 | 3 | 3 | | 3 | 3 | 5 | 2 | 3 | 3 | 3 |
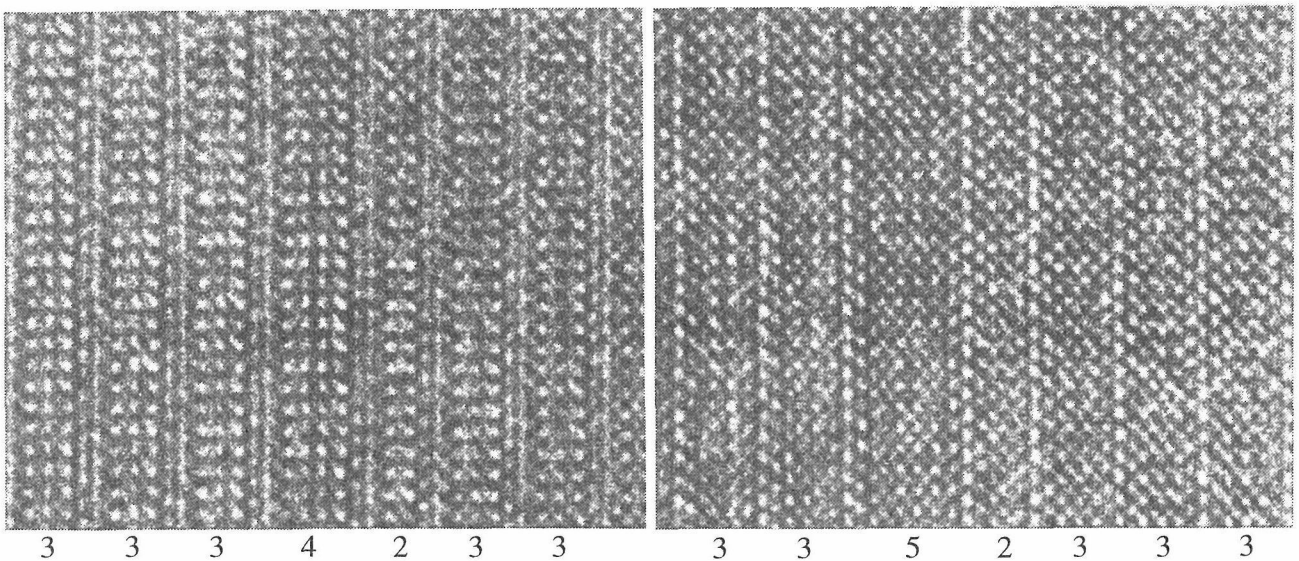
Fig. 4: HRTEM images of stacking defects in Hg-1223. The intercalated slabs of Hg-1234 (left) and Hg-1245 (right) are always paired with one slab of Hg-1212.

Besides the pure members of the homologous Hg-cuprate series with stoichiometries intermediate between those of the Hg-1212 and Hg-1223 phase could be observed. The composition of these grains corresponds to Hg-2435. These intermediate materials are either a random sequence of unit cell slabs of Hg-1212 and Hg-1223, or they consist of a specific short or long sequence of unit cell slabs of these two phases which is repeated periodically normal to the c-direction. This repeat is completely periodic over one whole grain. This complicated crystal structure differs from a normal superstructure, because it is composed of structurally and chemically different basic units. Therefore, and also by contrast to disordered sequences called disordered polytypes, we term these structures ordered polytypes.

Table 1

type	a / c	stacking sequence 3=Hg-1223, 2=Hg-1212	polarity
a	3.85 / 28.7	3-[2-3]-2-3-2	no
b	3.85 / 70.1	3-[3-2-2-2-3]-3-2-2-2-3-	no
c	3.85 / 86.1	3-[3-2-2-3-2-3]-3-2-2-3-2-3-	yes
d	3.85 / 143.5	3-[2-2-3-2-3-3-2-3-2-3]-2-2-	yes
e	3.85 / 188.1	3-[2-3-2-3-2-3-3-2-3-2-2-3-3]-2-3-	yes

We have observed five such ordered polytypes differing in their c-parameter. The cell parameters together with the periodically repeated sequences are listed in Table 1. The most simple of these polytypes has a c-parameter of $12.75 + 15.95 = 28.7$Å. A related ordered structure which represents a specific phase is the compound $Y_2Ba_4Cu_7O_{15-x}$, which has alternating layers of the phases $Y_1Ba_2Cu_3O_{7-x}$ and $Y_2Ba_4Cu_7O_{15-x}$ [9,10]. Most of the sequences of Hg-1212 and Hg-1223 given in table 1 are different when regarded along the two directions of the c-axis. This polarity appears to be a specific property of these polytype sequences. The two polytypes in table 1 which have an odd number of subunits differ in the bulk chemical composition from the ideal formula Hg-2435 by small amounts. HRTEM micrographs of three of the five polytypes, namely a,c and d, are presented in Fig.s. 5,6 and 7, respectively. In Fig. 8 a quarter portion of a SAED pattern showing reflections corresponding to the reciprocal c-axis repeat is presented. The distinct and sharp spots indicate the high degree of order in the polytype.
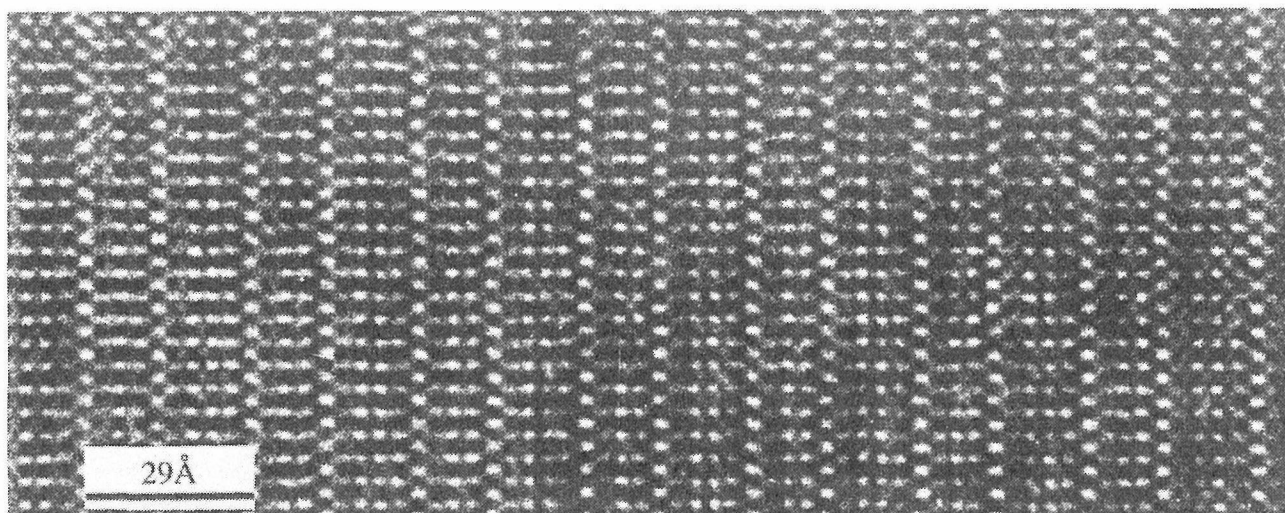
Fig. 5: HRTEM image of the polytype a with alternating Hg-1212 and Hg-1223 slabs.
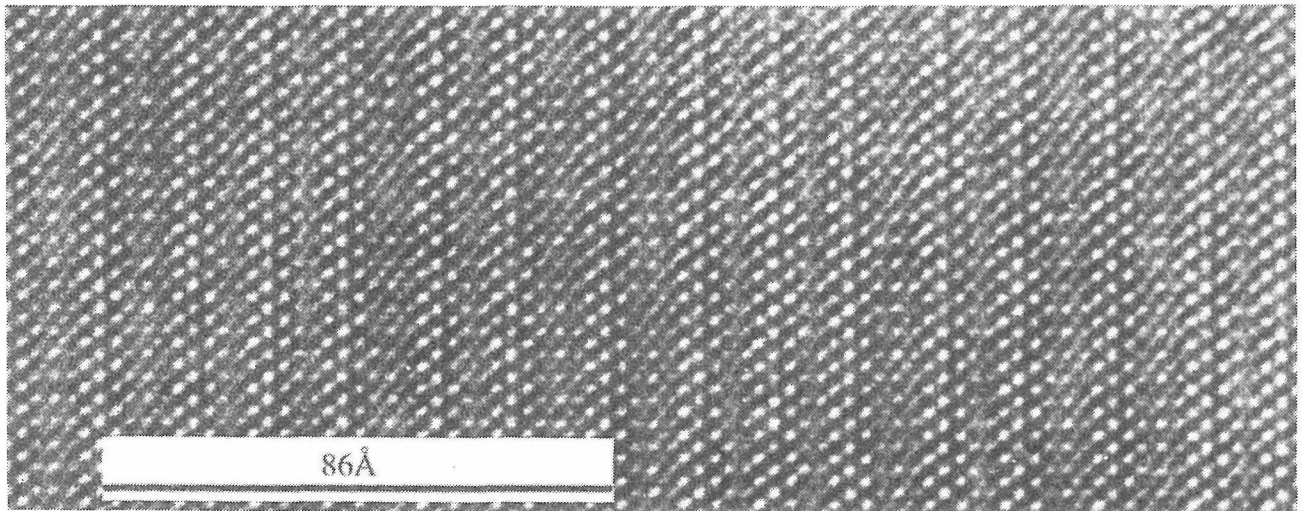
Fig. 6: HRTEM image of polytype c with the stacking sequence 3-2-2-3-2-3.
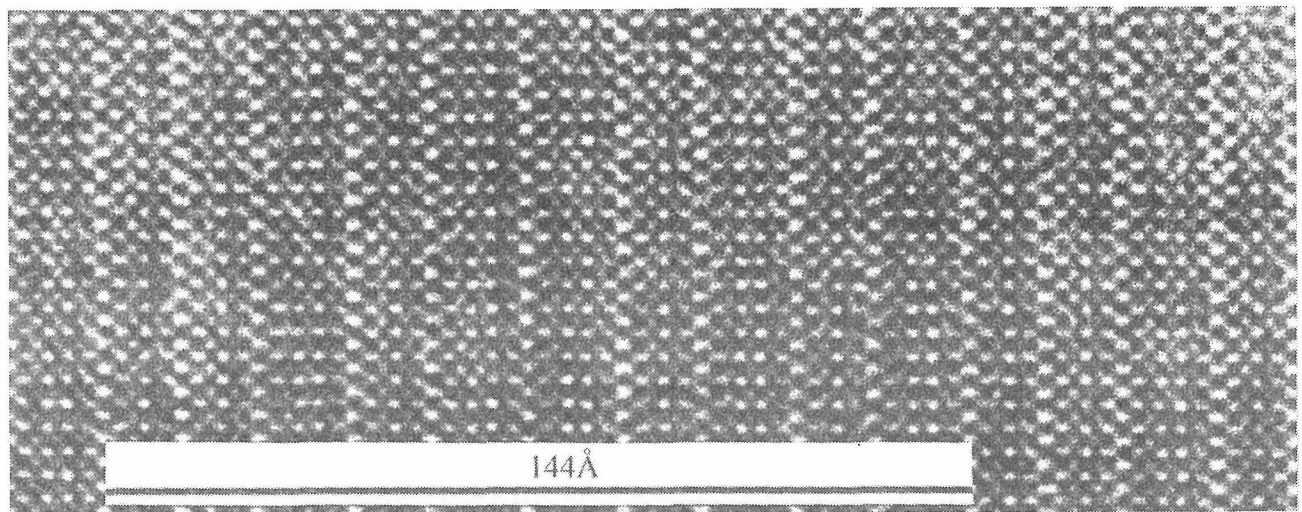
Fig. 7: HRTEM image of polytype d with the stacking sequence 2-2-3-2-3-3-2-3-2-3.
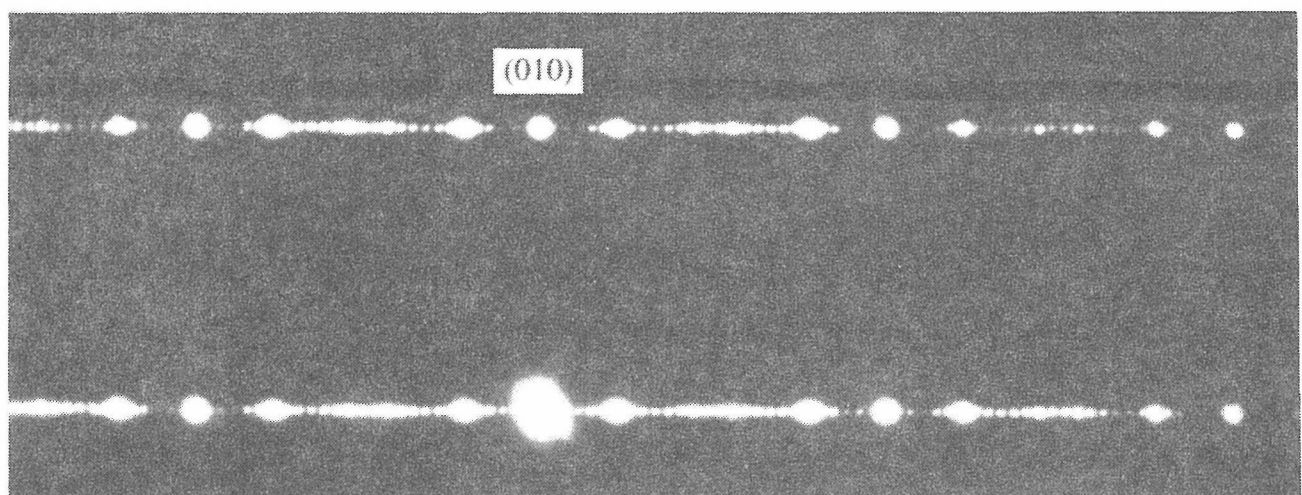
Fig. 8: SAED diffraction pattern of the (100)-pole of the polytype d, shown in Fig. 7. The sharp spots indicate the perfect ordering of the structure over large areas.

4. Discussion

Considering the crystal properties of the Hg-cuprates described here in comparison with the Tl homologous series, the similarity in the cell geometry between the Hg- and the corresponding Tl-compounds is evident. This is astonishing in view of the difference in the valency of Hg^{2+} and Tl^{3+}. In our as-prepared samples we have observed all members in the Hg-12(n-1)n series up to n=5 (compare Fig. 1). The fact that stacking defects are always found to be a single unit cell slab of the n=4 and n=5 member associated with one slab of Hg-1212 (n=2), can at present not be explained.

An astonishing feature of the polytype structure described here is the unusually high degree of ordering in the c-axis repeat and the existence of very large c-parameters up to 188Å. It is presently not known, whether these polytypes represent thermodynamically stable phases or must be interpreted as a transitional stage in the formation of the Hg-1223 phase from the Hg-1212 phase. The most fascinating problem is that of the growth mode of the Hg-polytypes with their specific and perfectly translated stacking sequences. It is not known whether this phenomenon is related to diffusion processes or possibly originates from step growth propagation at spiral dislocations.

References

[1]   Putilin S. N., Antipov E.V., Chmaissem O., Marezio M. (1993) Nature **362**: 226.

[2]   Schilling A., Cantoni M., Guo J.D., Ott H.R., (1993) Nature **363**: 56.

[3]   Cantoni M., Schilling A., Nissen H.-U., Ott H.R., (1993) Physica C **215**: 11.

[4]   Kaneko T., Yamauchi H., Tanaka S., (1991) Physica C **178**: 377.

[5]   Gopalakrishnan I.K., Yakhmi J.V., Iver R.M., (1991) Physica C **175**: 183.

[6]   Parkin S. S. P. et al., (1988) Phys. Rev. Lett. **61**: 750.

[7]   Schilling A., Jeandupeux O., Guo J.D., Ott H.R., (1993) Physica C **216**: 6.

[8]   Stadelmann P., (1987) Ultramicroscopy **21**: 131.

[9]   Beeli C., Nissen H.-U., Kawamata Y, Stadelmann P., (1988) Z. Phys. B **73**: 313.

[10]   Bordet P. et al., (1988) Nature **334**: 596.

Development of High-Resolution, High-Voltage Electron Microscope and Its Applications to Oxide Superconductors

S. Horiuchi and Y. Matsui

National Institute for Research in Inorganic Materials, Tsukuba, Ibaraki 305, Japan

Abstract

Some characteristic features, especially on the resolving power, of an ultra-high-resolution high-voltage electron microscope (UHR-HVEM), constructed at NIRIM in 1990, are shortly summarized. Recent applications of this EM on the high-Tc superconductors are then presented: 1) Direct observation of oxygen atoms in $YBa_2Cu_3O_{6+x}$ became possible and their distributions have been clarified. 2) An HRTEM image of a twin boundary in a very thin fragment of $YBa_2Cu_3O_{6.4}$ was taken and the structure was determined to be of "oxygen-centered type". 3) A wavelength of the structural modulation in $Bi_2Sr_2CaCu_2O_{8+x}$ was measured at a low temperature near 20K.

1. Introduction

In 1990 we have constructed a new UHR-HVEM (model H-1500)[1,2]. The Scherzer resolution limit of the microscope, analyzed from the measurement of electron-optical parameters, is 1.04 Å at the accelerating voltage of 1300kV, 1.25Å at 1000kV and 1.4Å at 800kV.

The main purpose of the microscope is to visualize all the atoms in ceramic materials, including oxygens in high-Tc superconductors, to determine crystal structures.

2. Measurement of point-to-point resolving power

Fig. 1 shows the experimental measurement of the point-to-point resolving power of the microscope together with the result of analysis. Images of the leftmost columns show the through-focus series of images, taken from a Ge thin film. The accelerating voltage is 800kV. The middle column shows corresponding optical diffraction patterns. Diagrams in the rightmost column show the intensity profile of the diffraction pattern calculated theoretically. Both experimental and theoretical diffraction intensities are in good agreement. We can conclude that the point-to-point resolving power (u_m) of the microscope is 1.4Å at 800kV.

3. Direct observation of oxygen atoms in $YBa_2Cu_3O_{6+x}$[3]

It is known that $YBa_2Cu_3O_{6+x}$ crystals has the structure of superconducting orthorhombic phase for $0.35<x<1$ and non-superconducting tetragonal phase for $0<x<0.35$. They are essentially similar to each other, i.e. the positions of metal atoms are almost the same for both of the structures. The structure can simply be denoted by the stacking sequence of $BaO/CuO_2/Y/CuO_2/BaO/CuO_y$ planes in the c direction. How many oxygens exist in the CuO_y planes determines their total content 6+x.

The imaging conditions for visualizing oxygen atoms in $YBa_2Cu_3O_{6+x}$ by the present microscope are examined first by computer simulations of

image intensity. They are defined in terms of the crystal thickness and the defocus amount, and summarized by a map in Fig.2, in which the areas for dark-spot and bright-spot (reversed contrast) images are specified. In one of the areas (area D1), which is realized nearly at the Scherzer defocus for a crystal thinner than 40 Å, column sites not only of metal atoms but also of oxygen atoms can individually be resolved as dark spots. The essential advantage of the UHR-HVEM for discriminating oxygen atoms is in the enhancement of the image contrast.

A small sintered block of $YBa_2Cu_3O_{6.4}$ crystal (Tc=27K, orthorhombic, a=3.84, b=3.87 and c=11.73Å) was lightly crushed in an agate mortar. Fragments obtained were mounted on a microgrid and observed in the UHR-HVEM. The accelerating voltage was selected at 800kV in order to avoid the irradiation damage[1]. Fig.3 shows a through-focus series of images from a very thin part of the crystal, taken with incident electrons parallel to the [001] direction[3]. The direct magnification was 3.5×10^5 times. The exposure time was 2 sec.

Figs.3(a), (b), (c), (d) and (e) are electron micrographs taken at the defocus of about 800Å (underfocus), 450 Å, 300 Å, 50Å and -300 Å (overfocus), respectively. Figs.3(a) and (d) are bright-spot images, while Figs.3(b), (c) and (e) are dark-spot ones. The contrast of images is apparently reversed between (a) and (b), (c) and (d), and (d) and (e). Images calculated for the areas B1, D1, D2, B2 and D3 in Fig.2 are inserted in Fig.3 with the same magnification. It is noted that they almost fit to each other. In (b) small dark spots are clear at the sites of arrowheads; the columns of oxygen atoms can clearly be discriminated beside those of metal atoms. The observation agrees with the previous report[4] that oxygens in the CuO_y planes distribute inhomogeneously.

The direct observation of oxygen atoms has also been performed for ZrO_2[5] and $YBa_2Cu_3O_{7.7}$[6].

4. Structure analysis of a twin boundary in $YBa_2Cu_3O_{6.9}$[7]

Twins are inevitably introduced in orthorhombic superconductive $YBa_2Cu_3O_{6+x}$ crystals. The boundary of twins contributes in increasing the critical current density Jc by acting as pinning centers for fluxoid[8]. However, its exact structure is not known. A reason for this is that the crystal is so sensitive to electron beam that high-resolution transmission electron microscopy (HRTEM) could not reveal the details, i.e. during HRTEM observation of $YBa_2Cu_3O_{6.9}$ a phase transition from orthorhombic to tetragonal system easily occurs mainly due to the temperature rise of crystals caused by electron irradiation[9,10]. The transition initiates at the twin boundary and propagates to the surrounding matrix[11]. This is due to that the orthorhombic lattice is distorted at the twin boundary[12].

The use of high-voltage electron microscopy (HVEM) seems useful because it induces less beam heating of specimens. The UHR-HVEM was operated at 800kV. In order to minimize the electron irradiation damage an image intensifier (Gatan model 622) was used. Highly sensitive photographic films (Mitsubishi EM film) were used to record images. Under an electron beam with the dose (~1A/cm^2) necessary for the HRTEM observation, a twin boundary started to change in about 30sec.

Fig.4 is an HRTEM image[7], taken by an electron irradiation within

30sec, nearly at the so-called Scherzer defocus (500Å underfocus). The electron beam is incident parallel to [001]. The exposure time was rather long (5sec) in order to attain the necessary intensity. At the twin boundary, marked by an arrow, lattice fringes bend sharply, although slightly, indicating that the structure has been little affected by electron irradiation. Although the image is not so sharp, we can recognize the position of dark spots, corresponding to the columns of metal atoms. The positions of Ba(Y) atom columns, which are identified as the darkest spots, are represented in the inset with the same magnification.

A possible structure model of the boundary derived from the result of Fig.4 may be as shown in Fig.5(a). It is noted that the twin boundary is of an "oxygen-centered type".

A model structure for optical diffraction was made based on Fig.5(a). Fig.5(b) is an optical diffraction pattern from the model: the fundamental spots are split due to the twinning and, moreover, a number of satellites with fine spacing appear along [110]. The spacing and intensity of satellites depend on the magnitude of θ and the size of selected area. Satellites must correspond to a diffuse diffraction streak really observed.[13]

5.Modulation wavelength in $Bi_2Sr_2CaCu_2O_{8+x}$ at ~20K

Thin fragments of a $Bi_2Sr_2CaCu_2O_{8+x}$ crystal (pseudo-tetragonal, a≒b= 5.4 and c=30.8Å), prepared by crushing, were mounted on a microgrid, which was cooled to about 20K. Figs.6(a) and (b) are an image and a corresponding diffraction pattern, taken with incident beam parallel to the c axis. Figs.6(c) and (d) are those after cooling, taken from the same area. It is found that the wavelength of structural modulation in the b direction changes from 4.75 to 4.92 on cooling. These were obtained by averaging 10 sampling values. Small sphere-like substances observed on the cooled microgrid are considered to be a frozen ice. The origin of the change in the modulation wavelength is unknown yet. A possible one is that extra oxygens, which must have been included, run out of the specimen on the electron beam irradiation at low temperature, although the electron dose used was rather low.

References
1) S.Horiuchi, Y.Matsui, et al.: Ultramicrosc. 39(1991)231.
2) Y.Matsui, S.Horiuchi, et al.: Ultramicrosc. 39(1991)8.
3) S.Horiuchi: J.Electron Microsc. 42(1993)166.
4) S.Horiuchi: Jpn.J.Appl.Phys. 31(1992)L1335.
5) S.Horiuchi and Y.Matsui: Jpn.J.Appl.Phys. 31(1992)L283.
6) S.Horiuchi, Y.Matsui and B.Okai: Jpn.J.Appl.Phys.31(1992)L59.
7) S.Horiuchi and A.Ono: Jpn.J.Appl.Phys. (1993) in press.
8) H.Fujimoto,T.Taguchi,M.Murakami and N.Koshizuka: Physica C 211(1993)393.
9) H.W.Zandbergen, G.van Tendeloo, T.Okabe and S.Amelinckx:
   Phys.Status Solidi a 103(1987)45.
10) S.Iijima, T.Ichihashi, Y.Kubo and J.Tabuchi: Jpn.J.Appl.Phys.
    26(1987)L1478.
11) T.Yoshino, Y.Tomokiyo and Y.Suyama: Proc.3rd Intl.Symp.
    Superconductivity (ISS'90), Sendai, (Springer, Tokyo, 1990) p.355.
12) Y.Hirotsu, Y.Nakamura, Y.Murata, S.Nagakura, T.Nishihara and M.Tanaka:
    Jpn.J.Appl.Phys. 26(1987)L1168.
13) Y.Zhu, M.Suenaga, J.Tafto and D.O.Welch: Phys.Rev.B 44(1991)2871.
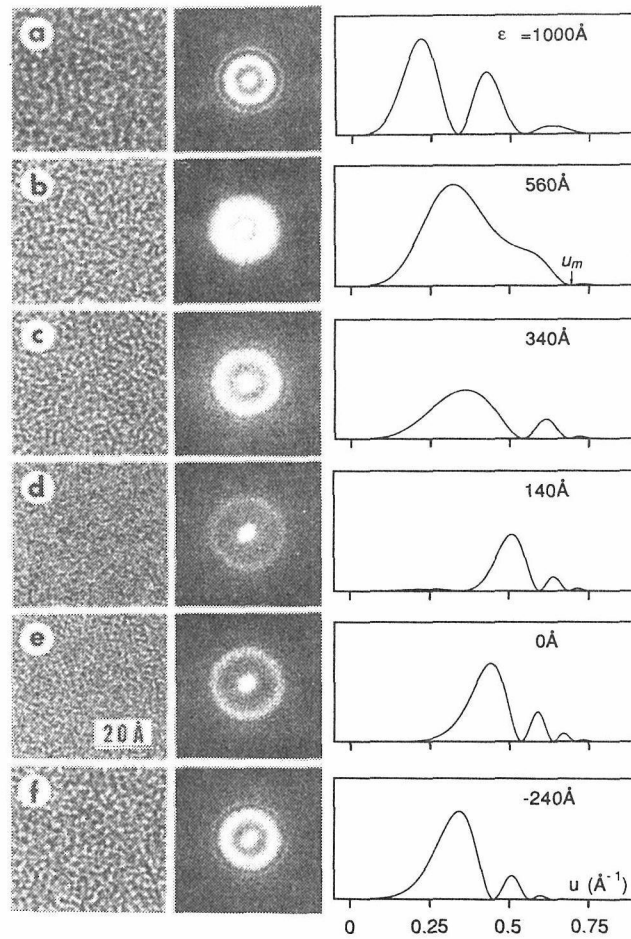
Fig.1 Measurement of the point-to-point resolving power of the UHR-HVEM. Through-focus images of a Ge thin film, corresponding diffraction patterns and calculated diffraction intensity are shown. ε means defocus values.

Fig.2 Defocus vs thickness map, showing the result of the computer simulation for image contrast. D means a dark-spot image, while B means a bright-spot image. Images attached in each area are calculated for the crystal thickness of 23.5Å and 74.3 Å, respectively. The accelerating voltage is 800kV, the spherical aberration constant is 2.2mm, the fluctuation of focus is 100Å and the illumination (half-) angle is 0.5mrad.
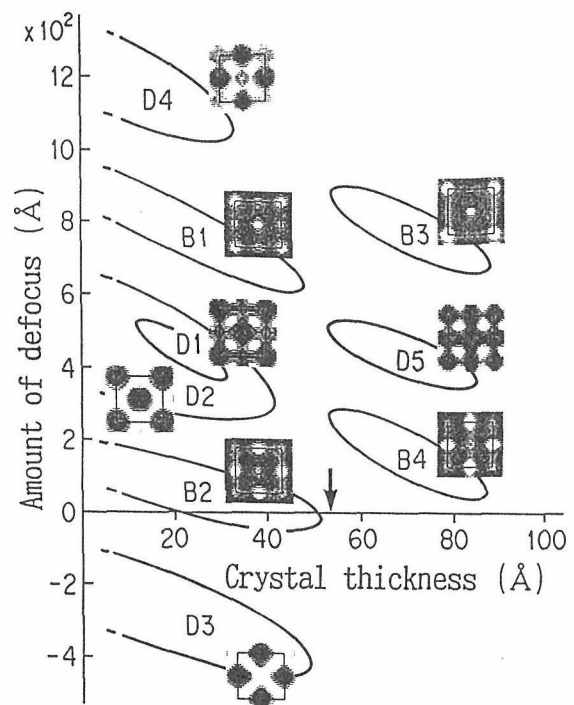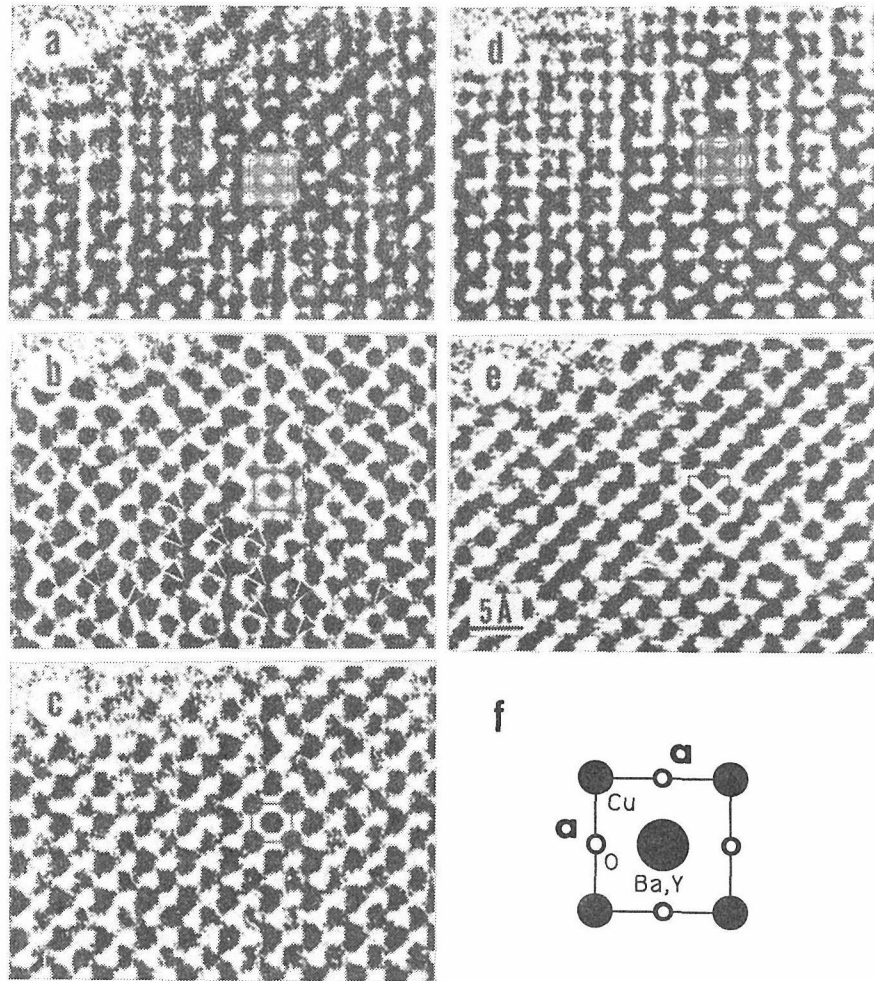
Fig.3 Through-focus series of UHR-HVEM images for a very thin part of $YBa_2Cu_3O_{6.4}$, taken with incident beam parallel to [001] at 800kV. The defocus amount is 800 Å (a), 450 Å (b), 300 Å (c), 50Å (d) and -300 Å (e). (f) is a projected structure of the unit-cell. At arrowed sites in (b) small but clear dark spots are visible, showing the column sites of oxygen atoms.
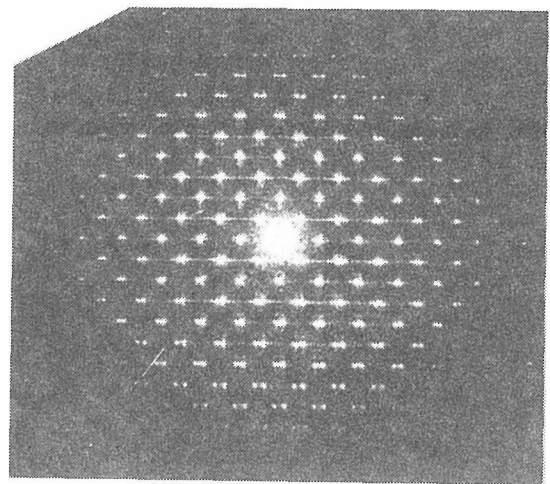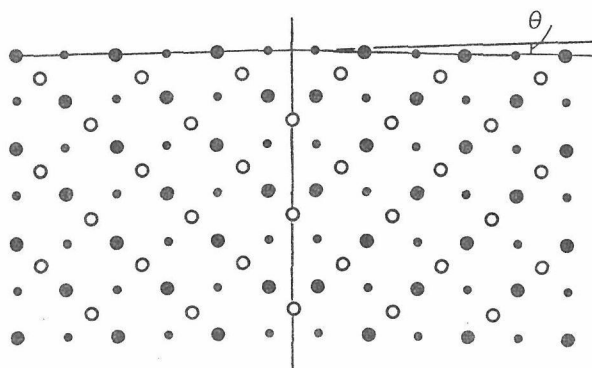
Fig.5 (a) A structure model for a twin boundary in $YBa_2Cu_3O_7$. (b) An optical diffraction pattern corresponding to (a). Finely split satellites appear along [110].
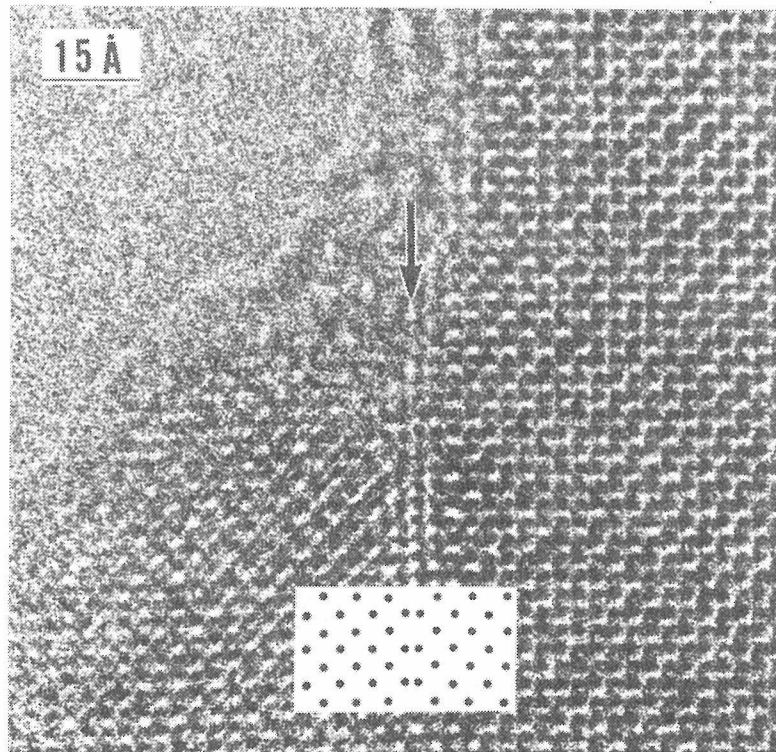
Fig.4. An HRTEM image of a twin boundary at a thin edge part of a $YBa_2Cu_3O_{6.9}$ crystal fragment, taken with incident electron beam parallel to [001]. Positions of the darkest spots, corresponding to the column sites of Ba(Y) atoms, are schematically shown.
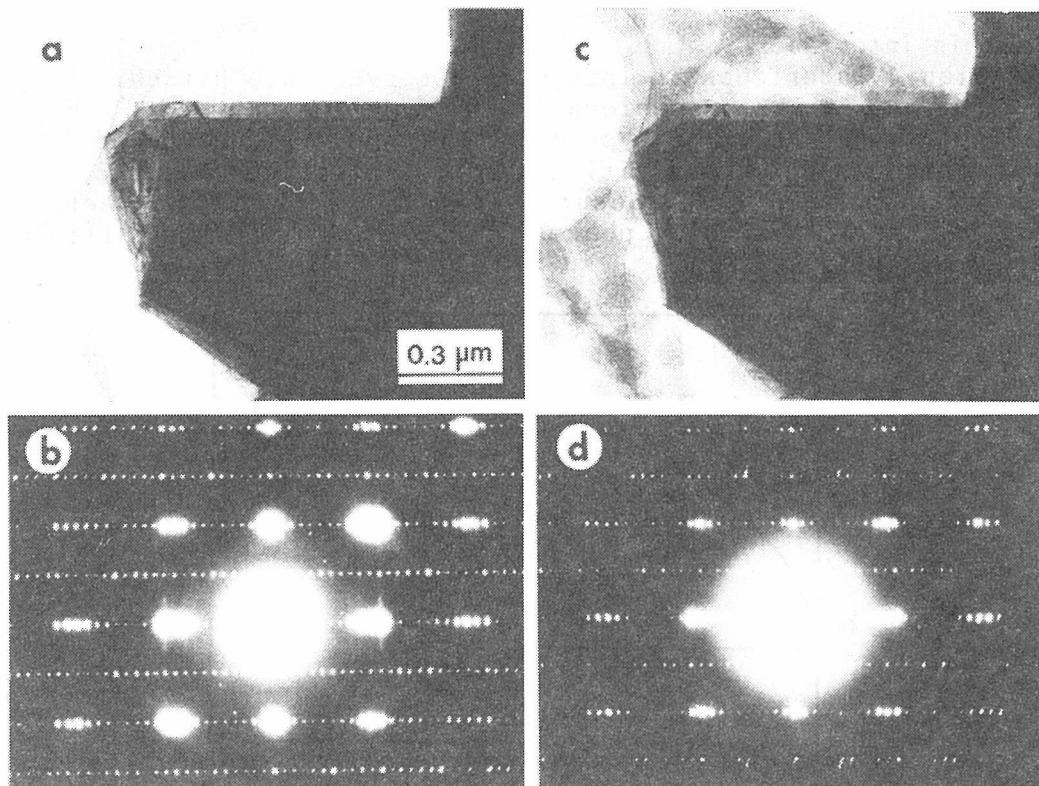
Fig.6 (a) and (b) are an HVEM image and a corresponding diffraction patterns of $Bi_2Sr_2CaCu_2O_{8+x}$ at room temperature. (c) and (d) are those after cooling to about 20K. The wavelength of structural modulation slightly increases on cooling.

In-situ Observations of Solid-liquid Interfaces by TEM

H. Saka, K. Sasaki and T. Kamino

Department of Quantum Engineering and Department of Materials Science and Engineering

Faculty of Engineering, Nagoya University, Nagoya 464-01

*Hitachi Instrument Engineering, Co. Ltd., 882 Ichige, Katsuta, Ibaraki 312, Japan

Recent observations by the in-situ electron microscopy of the melting processes in InSb and In have been reviewed with special reference to the morphology and structure of the solid-liquid interfaces. It has be shown that, in some cases, the structure of the solid-liquid interface can be observed at a resolution allowing the lattice-fringe image. The results of the observations have been compared with thoertical model of solid-liquid interfaces due to Jackson.

1. Introduction

The morphology of the solid-liquid interface plays a very important role in the processes of solidification and melting of crystals[1]. In-situ electron microscope observation is a very useful technique to observe directly the solid-liquid interface, and some in-situ observations of the solid-liquid interfaces have been carried out on metallic materials[2,3,4]. Unfortunately, the resolution of the in-situ observations carried out so far was not high enough for information on the solid-liquid interfaces, at near-atomic resolution level, to be obtained. However, recently some attempts have been made to observe the solid-liquid interface by in-situ high-resolution electron microscopy by the present authors, and will be described in this review.

2. Solid-liquid interfaces in InSb

Solid-liquid interfaces in InSb were observed in a Hitachi HU-1000D and H-1250ST microscopes at an accelerating voltage of 1000kV[5]. Fig.1 shows the phase diagram of the In-Sb system[6]. Intermetallic compound InSb occurs at the 1:1 stoichiometric composition and two eutectic reactions, namely L→ In + InSb and L → InSb + Sb, occur at 155°C and 500°C, respectively. The mutual solubility of the solid phases is vey small. Intermetallic compound InSb melts congruently at 530°C.
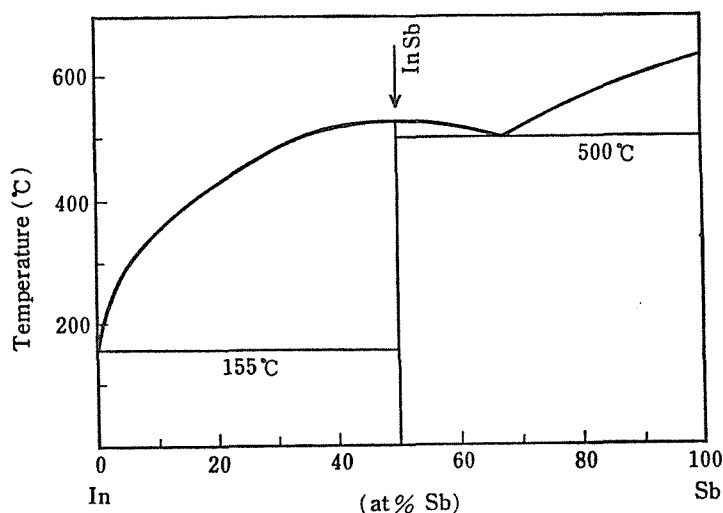
Fig.1   Phase diagram of In-Sb (From ref. [6]).

However, when foil specimens of InSb are heated in the vacuum of the electron microscopes, the depletion of Sb atoms starts well below the melting point of InSb owing to the preferential evaporation of Sb. As a result, the overall chemical composition of the heated foil specimens deviates from the original stoichiometric 1:1 composition towards the In-rich side. This means that, above the eutectic temperature between In and InSb(155°C), the foil specimen has an In rich liquid phase and an InSb solid phase, the composition and amount of the liquid phase depending on the temperature and the deviation from the stoichiopmetry.

Fig.2(a) and (b) show the typical structure of the mixture of the In-rich liquid phase and InSb matrix. Fig.2(c) shows the diffraction pattern from the liquid droplets; halo rings characteristic of non-crystalline (liquid) structure are clearly observed. The liquid droplets are elongated along [$\bar{1}10$] (intersection of the ($\bar{1}11$) plane with the surface plane(113)), indicating that the interfacial energy between the liquid and the solid InSb is anisotropic.
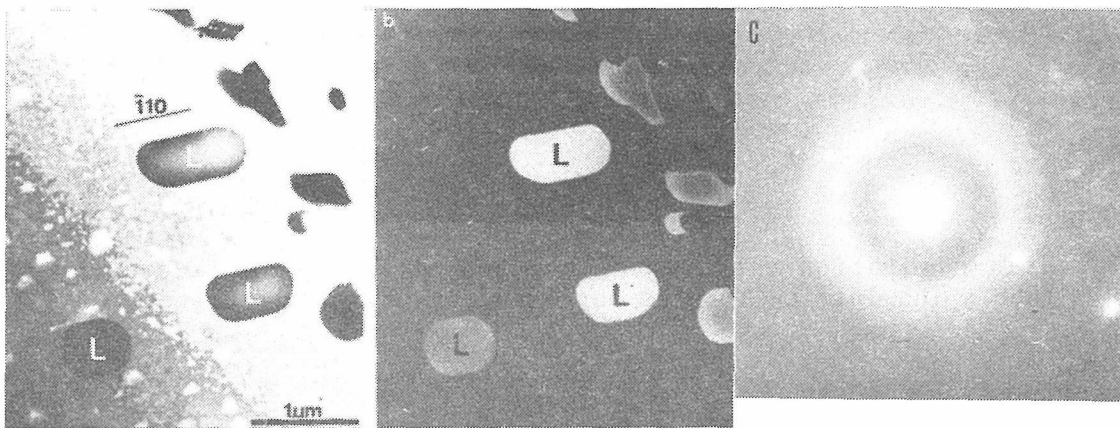
Fig.2   Structure of a foil specimen of initially stoichiometric InSb heated in an electron microscope: (a) bright field image with the beam direction B=113; (b) dark-field image using part of the first haloring of the diffraction pattern from the liquid droplets; (c) diffraction pattern from the regions marked L(From ref.[5]).

Fig.3 shows a high-resolution electron micrograph of the solid-liquid interface of InSb. Within the region of crystalline InSb the lattice-fringe images of the ($\bar{1}11$) planes was observed clearly, while in the liquid droplet no lattice-fringe images were seen. The interface along the ($\bar{1}11$) planes is very straight, while the curved interface shows no evidence for faceting.

Fig.4 shows an example of the interaction of pre-existing dislocations with migrating solid-liquid interface. As the liquid droplet grew, the dislocation moved in such a way that it intersected the solid-liquid interface at the right angle in order to reduce the line energy. However, neither preferential melting nor preferential solidification was observed at the intersection of the dislocation with the solid-liquid interface. It is thought that in-situ HREM observation is necessary to detect such an interaction.

3. Solid-liquid interfaces in In

Melting process of In particles embedded in an Al matrix has been observed continuously using an in-situ heating experiment in a H-1250ST microscope at an accelerating voltage of 1000kV [7,8]. Fig.5 shows the phase diagram of Al-In sysytem[6]. Again, the mutual solubility between Al and In is very small. Al-In alloy was splat-quenched from liquid state. Fig.6 shows a typical structure of Al-In alloy in the as-splat-quenched condition. It is
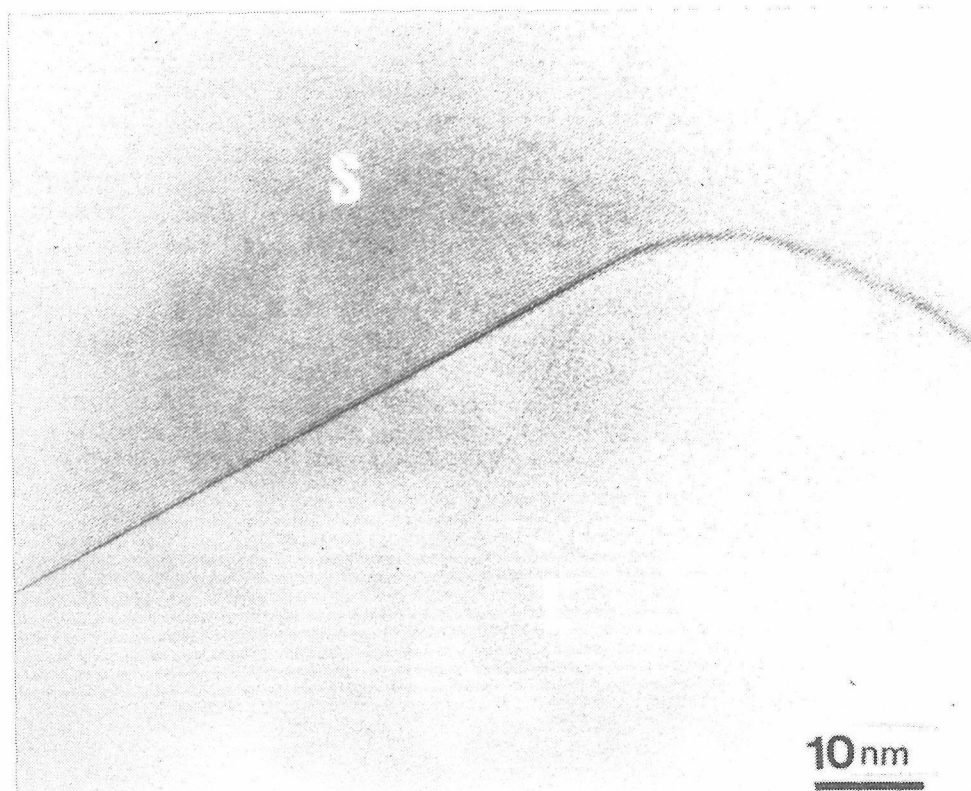
Fig. 3　High-resolution electron micrograph of the solid-liquid interface of InSb.　The lattice fringes correspond to the (Ī1̄1) plane.
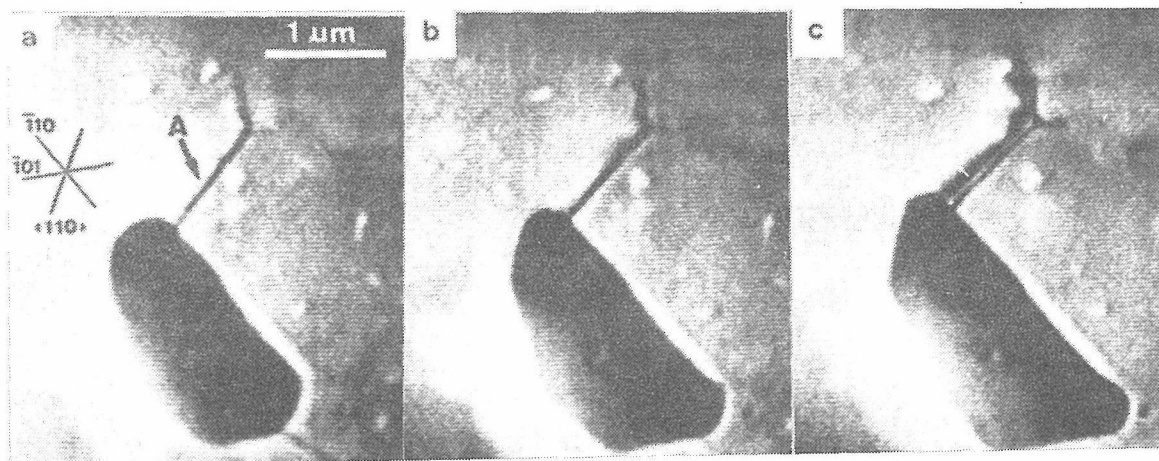
Fig. 4　Interaction of the solid-liquid interface in InSb with a pre-existing dislocation.　In-rich liquid droplet grew as the temperature was increased slightly.

clear that In particles were dispersed uniformly in a matrix of Al. The crystalline In particles are cuboctahedral in shape, and bounded by eight $\{111\}_{Al, In}$ and six $\{100\}_{Al, In}$ facets.

　　Melting started either at one of the $\{100\}$ facets and proceeded into the interior of the In particle. Fig. 7 shows an example of the solid-liquid interface in an In particle. The solid-liquid interface is not sharp in this case, in contrast to the case of InSb.

- 66 -
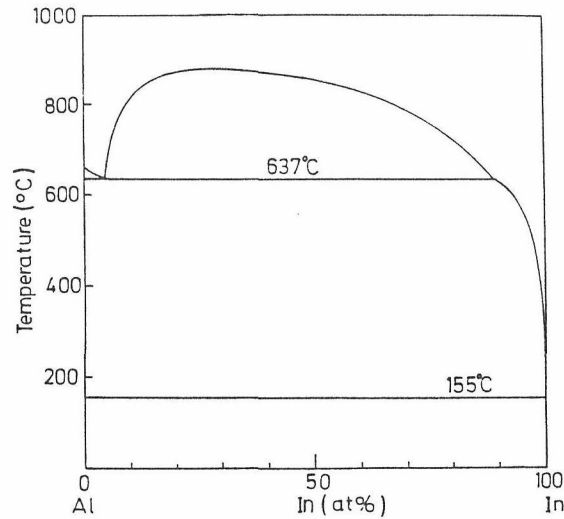
Fig. 5　Phase diagram of Al-In(From ref. [6]).

50nm
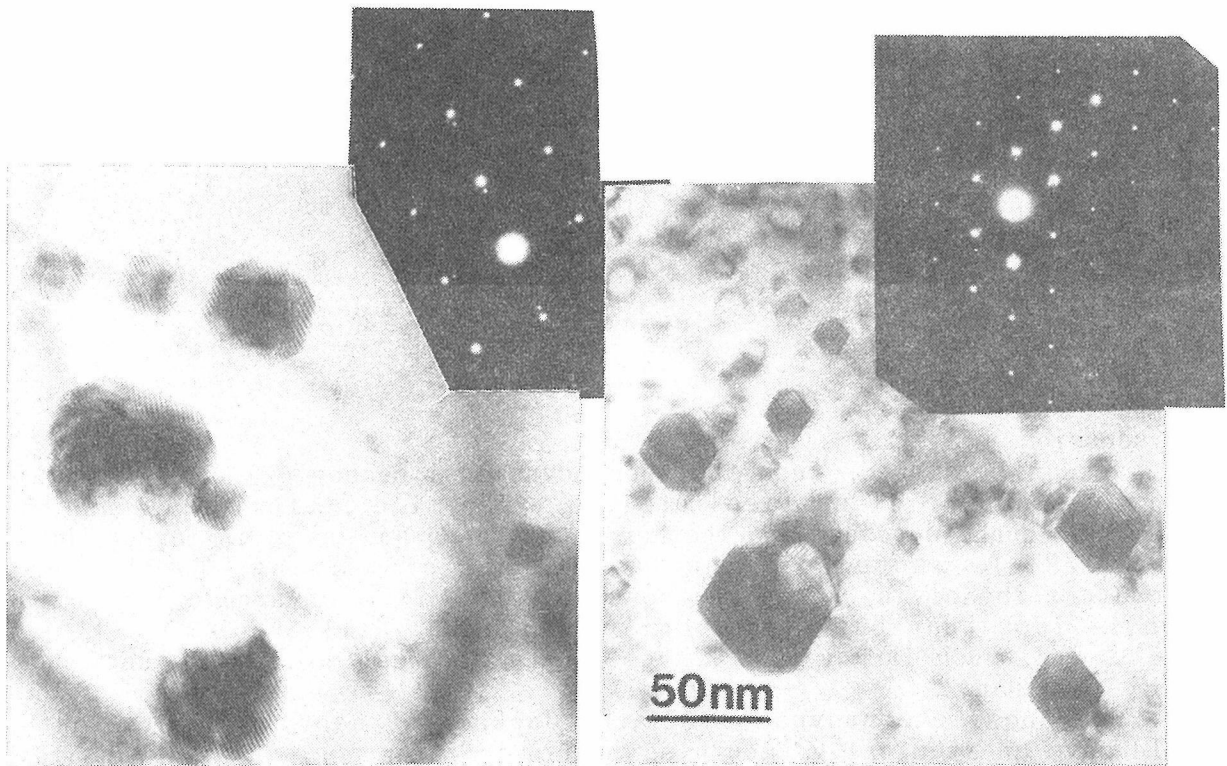
Fig. 6　Electron micrograph of splat-quenched Al-In alloy taken at room
　　　　temperature.　Inset shows the diffraction pattern;　it is clear that
　　　　there is an orientation relationship between In particles and an Al
　　　　matrix(From ref. [8]).
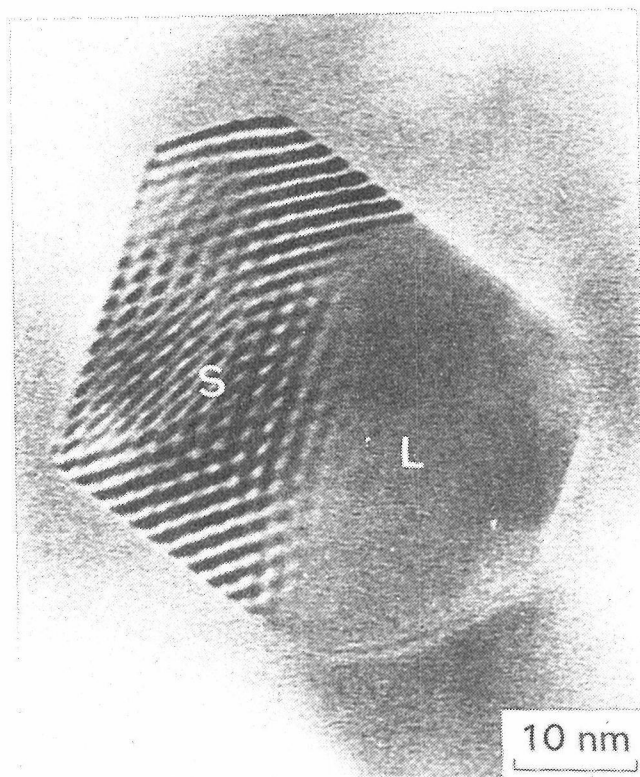
Fig. 7   High-resolution electron micrograph of a solid-liquid interface in an
          In particle (From ref. [8]).

4. Discussion

Jackson[1] showed, from the thermodynamical reasoning, that solid-liquid interfaces can be classified into two types, i.e., atomically smooth and atomically rough, depending on whether or not a parameter α is larger than 2. $\alpha = \zeta (L/RT_M)$, where L is the latent heat of melting, T_M the melting temperature in Kelvin, R the gas constant, and ζ a crystallographic factor which is less than but almost unity. For InSb, L=11.8kcal mol^{-1}[10], and hence α =7.4, much larger than 2. For In, L= 0.78kcal mol^{-1}[10], and hence α = 0.9, less than 2.

From these thermodynamical data, Jackson's theory predicts that InSb should have an atomically smooth solid-liquid interface, while In should have atomically rough solid-liquid interfaces. Comparison of Fig. 3 with Fig. 6 indicates that this prediction is valid for InSb and In.

References

[1] K.A.Jackson, Liquid Metals and Solidification (ASM, Cleveland, 1975) p. 174.
[2] M.E.Glickman, and C.L.Vold, Acta Metall., 15 (1967), 1409.
[3] C.Lemaignan, D.Camel, and J.Pelissier, J.Crystal Growth, 52 (1981), 67.
[4] R.Hamar, and C.Lemaignan, J.Crystal Growth, 53 (1981), 586.
[5] H.Saka, A.Sakai, T.Kamino, and T.Imura, Phil.Mag.A, 52 (1985), L29.
[6] M.Hansen, Constitution of Binary Alloys, second edition (McGraw-Hill, New York, 1958).
[7] H.Saka, Y.Nishikawa, and T.Imura, Phil.Mag.A, 57 (1988), 895.
[8] K.Sasaki and H.Saka, Phil.Mag.A, 63 (1991), 1207.
[9] S.Iijima, and T.Takahashi, Phys.Rev., 56 (1986), 616.
[10] O.Kubaschewski, and C.B.Alcock, Metallurgical Thermochemistry, fifth edition (1979, Pergamon Press, Oxford).

Typical Defects in AlN and SiC Ceramic Compounds

D. Dorignac, A. Mazel, D. Tang, Ph. Marti, Y. Kihn, S. Schamm, Ch. Grigis, V. Serin, S. Abaïdia,
G. Zanchi and J. Sévely

CNRS, CEMES-LOE, MEA, BP4347, 31055 Toulouse, France

Abstract

AlN and SiC coatings prepared by LPCVD have been examined by several complementary TEM techniques, including ED, EELS, EXELFS and HREM, to determine the local chemical compositions and structures. The major features of the AlN compounds lie in the occurrence of extended planar defects. It is suggested that these defects are induced by oxygen impurities. The SiC layers structure is found to be consistent with a heavily twinned zincblende model, leading in most cases to a one-dimensionnally disordered polytype with a wide variety of typical defects

Introduction

Aluminium nitride (AlN) and silicon carbide (SiC) are probably the most widely used ceramic materials in the area of structural composites. They are of considerable interest in advanced materials sciences, since they have important potential applications, particularly as thermostructural compounds. Moreover, as already widely discussed, their physical properties are known to be strongly dependent on the microstructure and, therefore, on the processing parameters. For example, it has been suggested that the addition of small quantities of oxygen, which affects the thermal properties of AlN adversely, could stabilize the compounds against hydrolysis[1].

Previous approaches to the characterization of particular AlN and SiC deposits, obtained by low-pressure chemical vapour deposition (LPCVD), have been reported[2-3]. This paper is thus primarily concerned with recent studies on similar compounds, trying (i) to clarify the influence of oxygen doping on local AlN defect structures and (ii) to explain some defects associated with the SiC "chaotic" polytypism. The experimental applicability of the TEM techniques to the study of these coatings is also demonstrated.

Experimental details

The AlN and SiC layers were grown on polycrystalline graphite substrates in a LPCVD hot-wall reactor[4]. The source gases for preparing AlN were $AlCl_3$ vapour, H_2, NH_3 and N_2, with addition of N_2O in order to obtain "oxygen-doped" compounds. For SiC the decomposition of tetramethylsilane (TMS) and H_2 as carrier gas were used. Thin specimens, suitable for TEM, were then prepared from the above samples by cutting them into 2.3mm disks, mechanical polishing and by Ar^+ ion milling at liquid N_2 temperature to perforation.

The electron microscope used was a Philips CM30ST (spherical aberration constant C_s=1.2mm), operating at 300kV, with a point (interpretable) resolution of 0.20nm at the optimum defocus (-58nm). For HREM, a careful operating procedure was followed at direct magnification of 1M in the axial-illumination bright-field (AIBF) mode, based on a Sofretec (CF1500) high resolution TV camera, for image acquisition, and a Synoptics advanced software package (SysTEM), for microscope control and on-line image processing, namely: (i) fine astigmatism correction, (ii) accurate coma-free alignement and (iii) identification of the correct defocus by reference to the neighbouring crystal edges. The simulated images were computed using standard (MacTEMPAS) multislice techniques, since no additional improvement is really needed for relatively simple structures consisting of low-Z elements, such as those investigated here[5]. Instrumental factors corresponding to the Philips CM30ST were included in the calculations: rms electron-beam focal spread 8nm; incident beam divergence semi-angle 1.2mrad; rms vibration parameter 0.02nm. Since no objective aperture was used in the HREM experiments, an "effective" aperture with a radius of $10nm^{-1}$ was used in the calculations.

For EELS, an on-line Gatan (666) parallel detector spectrometer, with an attainable energy resolution of 1.5eV (full width at half maximum of the zero-loss peak), has been used. Appropriate electron probe diameters, varying from 10 to about 40nm, have been chosen. For the quantitative chemical analyses, the EELS spectra were processed using standard Gatan software. For analysing the EXELFS modulations a software developed in the laboratory has been employed[6].

Results and discussion

AlN. The material prepared with a N_2O gas flow appears to consist of a disordered assembly of similar microcrystals, exhibiting "feather-like" shapes. Intermediate magnification pictures reveal the presence of isolated and extended structural defects. This is evidenced in figure 1, which shows an example of TEM dark-field (DF) images obtained by selecting the 1-11 diffraction spot, the incident electron beam direction being parallel to the [110] zone axis.

When examined in the HREM mode, the defects confined to the extremities of the crystals prove to consist of intrinsic (I1 type) parallel stacking faults. Two typical examples are given figure 3: from the simulated images it is clear that atomic shifts occurred in two particular (001) atomic planes, separated by three (a) or eleven (b) intermediate planes.

How do these defects form, when the microcrystals are growing, and do they contain oxygen atoms? Because of their absence in pure AlN and, on the contrary, of their abundance in the oxygen-doped AlN, it is probable that they could have been created during the progressive introduction of N_2O in the gas mixture used as a precursor. Other AlN defect structures are known to have a large affinity for oxygen as an impurity[7]. These "chemically-induced" stacking faults could also have been capable of progressively accommodating single O atoms, one per original unit cell, in agreement with the average EELS and EXELFS results. Figure 1b shows an example of the resulting radial distribution functions (RDFs): the appreciable enlargement of the first peaks can, effectively, only be attributed to the additional Al-O distance (0.2185nm) corresponding to O atoms filling the empty octahedral sites of the hexagonal-close-packed structure[8].

It should then be possible that O atoms remain locally concentrated in the fault basal planes. But it is unfortunately very difficult to prove this by means of EELS, since the local detection of small amounts of such light atoms is only just feasible at present[9]. Moreover, till now, we have obtained no experimental evidence of this by means of HREM, although the presence of the O atoms can modify the image contrast just sufficiently to be noted. See for example the comparative simulations shown in figure 4, which emphasize that O atoms are not present in the stacking faults shown in figure 3. Another possible explanation is that the O atoms may rapidly be evacuated during their observation under the electron beam, particularly in the ultra-thin areas required for HREM. Extensive HREM observations are in progress to clarify these points.

SiC. Conventional TEM observations of the layers reveal that the structure is consistent with a heavily twinned zincblende model, as shown figure 2. The extra spots due to the twins can easily be recognized on the corresponding ED patterns. Figure 2 also shows typical examples of EELS spectra obtained from individual microcrystals and exhibiting the characteristic Si-L and C-K edges. The deduced (Si/C) atomic concentration ratio is close to 1, in agreement with both the SiC chemical stoichiometry and the above zincblende crystalline structure.

The interesting structural phenomenon that often occurs in SiC, the one-dimensional disorder (so-called "chaotic polytypism"[10]), that allows many structures with different stacking sequences to occur, is clearly visible in the HREM images. An example is shown in figure 5.

Figure 6 shows other high-magnification HREM images displaying features common to most of the images recorded. A structural model is proposed for the marked grain boundary, which necessarily involved lengthy computer simulations. Note that the agreement is good, in spite of some contrast variations, probably due to the fact that the ordering is assumed to be perfect along the defect length. This is a rare example where it proves possible to utilize the extra information available beyond the Scherzer limit.

Interfacial structure is of fundamental importance in influencing the properties of these ceramics. Figure 7, for example, shows a single micrograph from which one should be able to determine the atomic arrangements in the vicinity of an SiC/Si interface. The interface is effectively sufficiently flat, with no interfacial steps, and it presents an edge-on configuration to the incident beam direction. It can also be seen that crystallinity continues up to the interface.

Line defects such as dislocations are difficult to image because the sample must be tilted in such a way that the defect lies precisely along the beam direction. Nevertheless, it is clear from the examples given in figure 8 that HREM is singularly successful for characterizing these crystal imperfections. The structure of the disordered central region in 8b can be simulated, even it appears that the match with the experimental image is still rather qualitative, probably because the extent of the real defect is not as well defined as the proposed structural model. Experimental HREM micrographs are currently being compared with image simulations based on structural models, in particular to analyse the defect terminations.
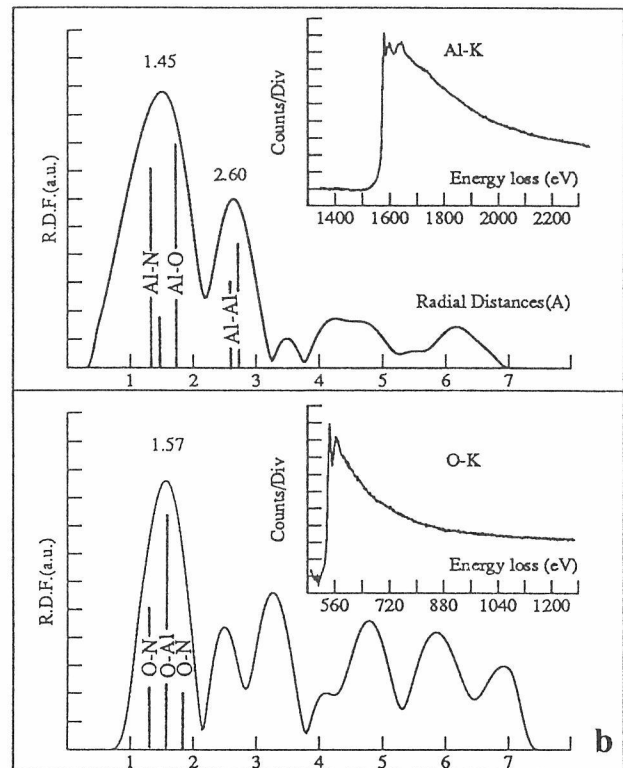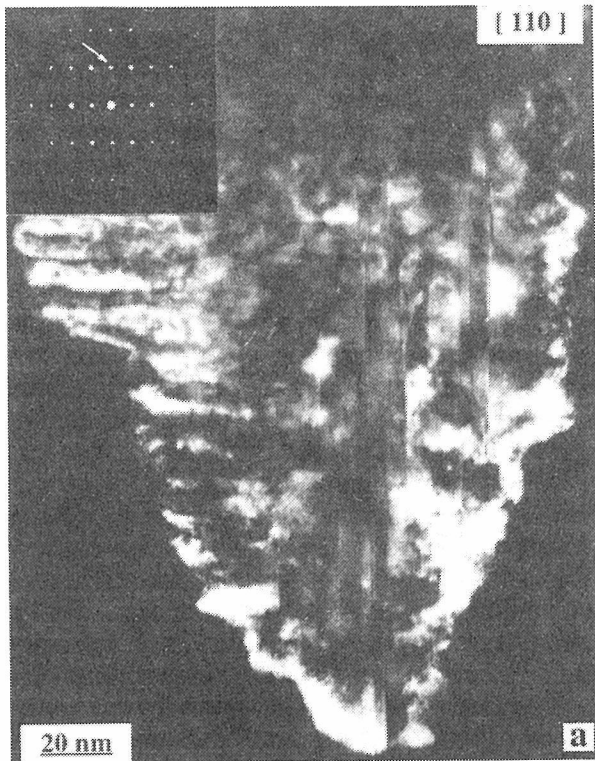
Figure 1. AlN: a) TEM DF image illustrating the "dendritic" aspect of the "oxygen-doped" microcrystals, with the presence of central (always) and lateral (sometimes) extended defects. The inserted ED pattern, for [110] zone axis, confirms the normal AlN wurtzite (2H type) structure.

b) Typical RDFs obtained from the EXELFS modulations of the (inserted) EELS spectra around the Al-K and the O-K edges. The enlargement of the first main peak reveals that single O atoms are inserted in the wurtzite AlN unit cells in the empty octahedral sites (add a 0.047nm phase shift correction).
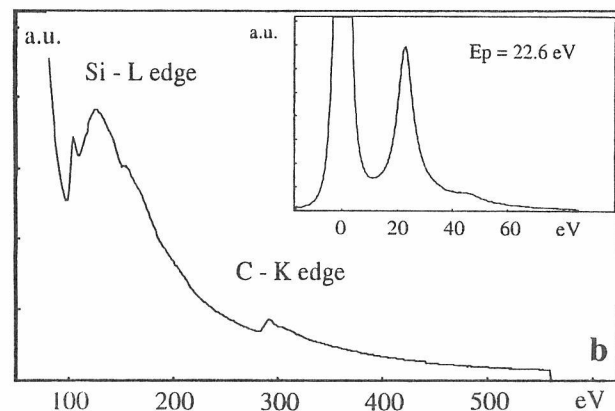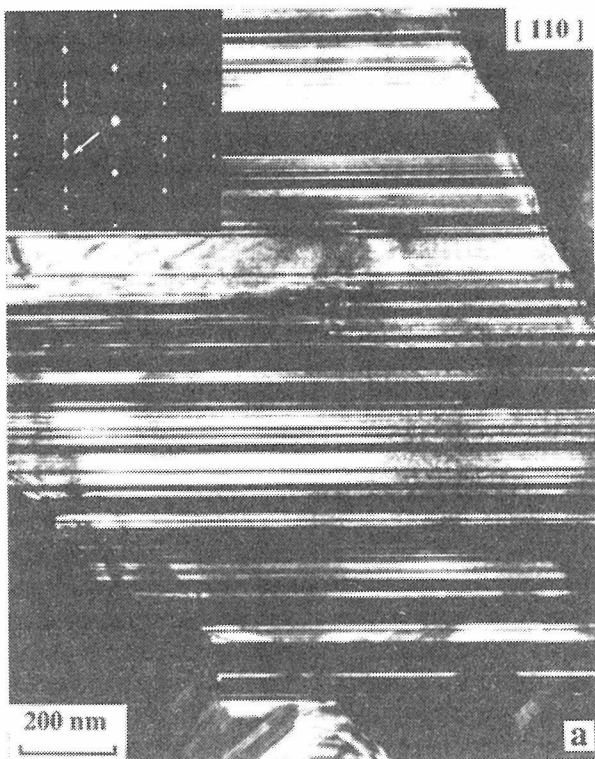
Figure 2. SiC: a) Typical low-magnification TEM DF image associated with the arrowed reflection, clearly revealing the distribution of the twins; b) Typical EELS spectrum: the C plasmon peak at 22.6eV confirms the SiC stoichiometry.
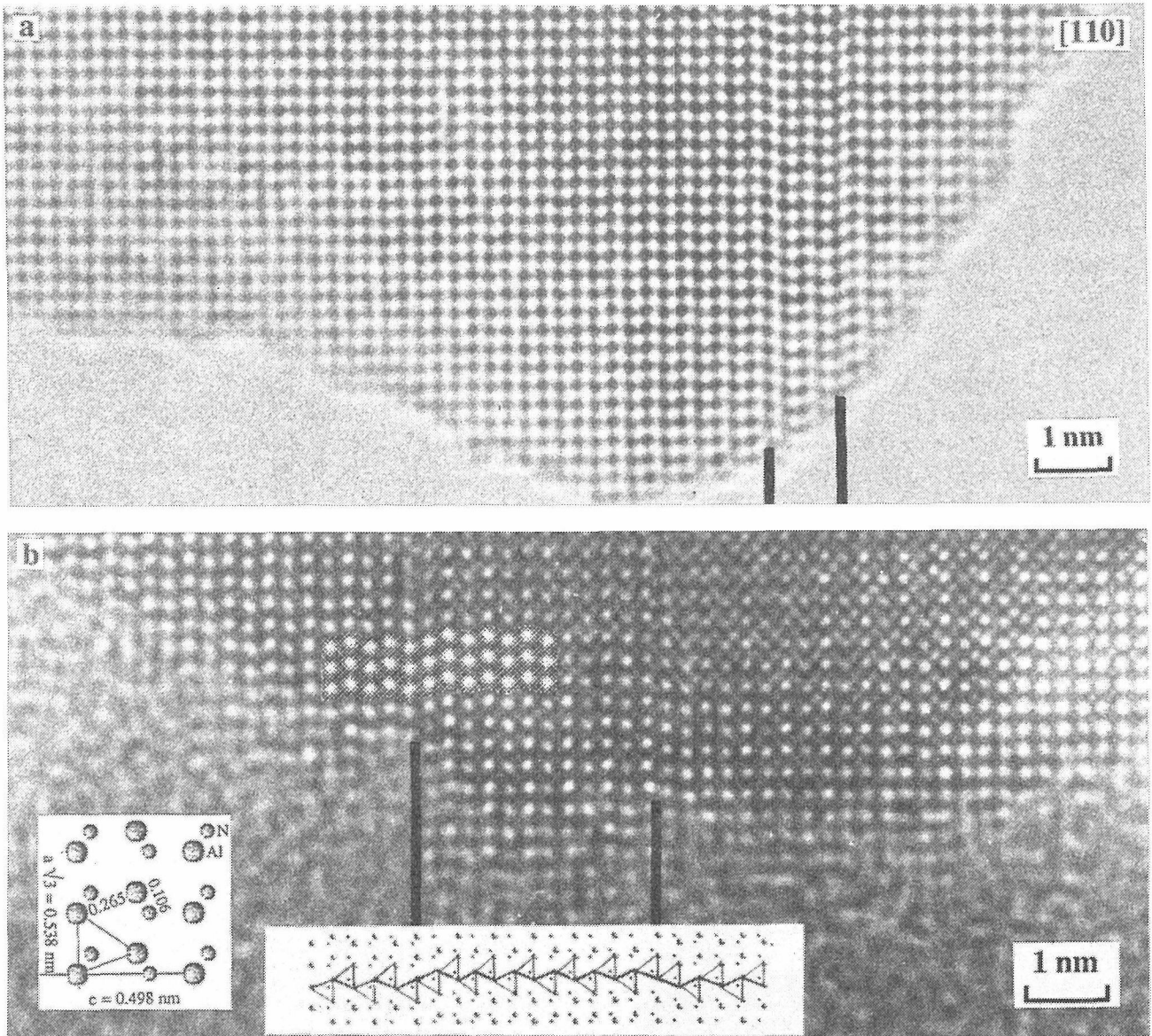
Figure 3. AlBF HREM images corresponding to the ultra-thin extremities of the central defects. From the simulations, the defects are revealed to be double intrinsic stacking faults (I1 type). The structural model corresponding to image b is inserted (Scherzer optimum focus; black spots corresponding to (unresolved) Al-N atomic bi-columns).
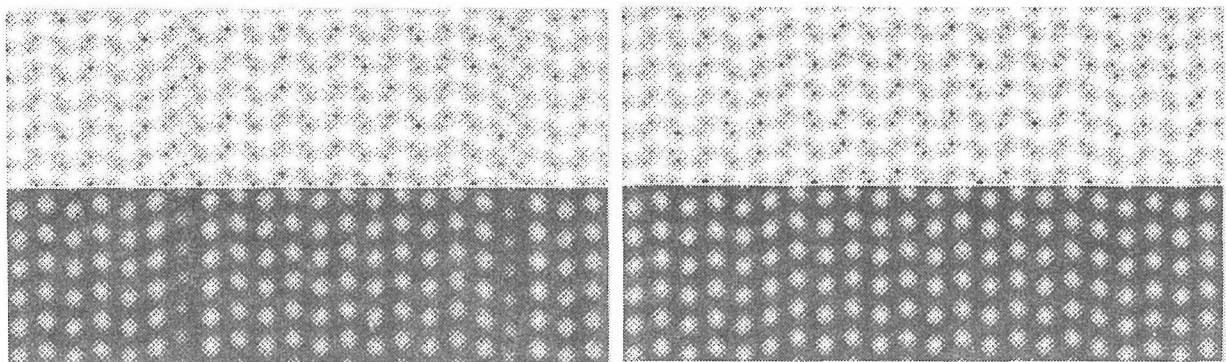
Figure 4. HREM computer image simulations (bottom) and corresponding projected structure potentials (top), with (left) or without (right) O atoms inserted in the basal planes of the two stacking faults. Structural model corresponding to figure 3b: crystal thickness: 4nm; microscope defocus: -58nm; "black" atoms. Compare with the above experimental image.
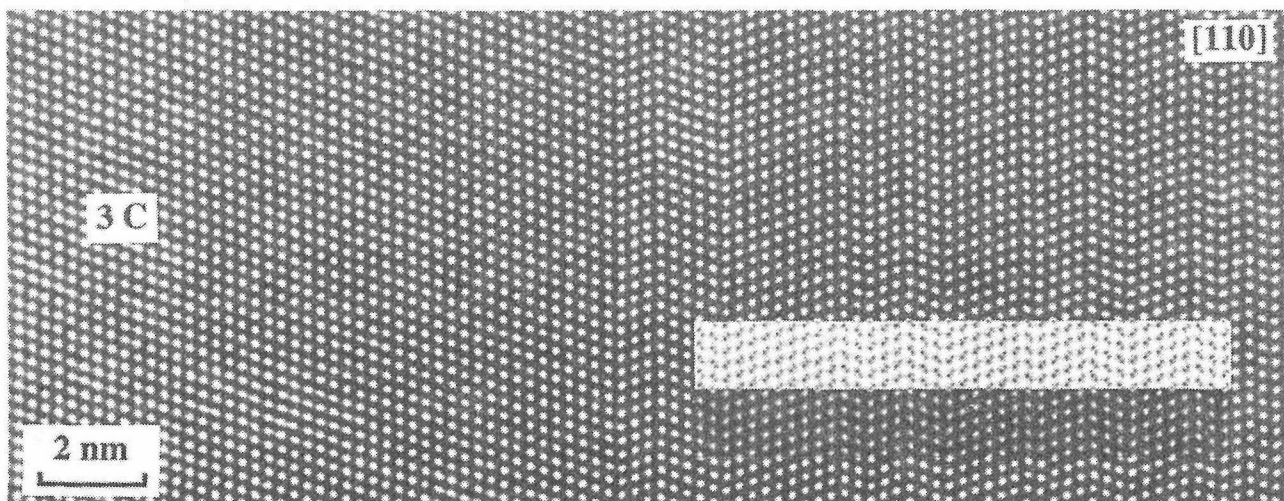
Figure 5. AIBF HREM image of a SiC microcrystal with uniform thickness, observed in [110] direction. Left: perfect 3C zincblende structure; right: characteristic one-dimensional disorder, with corresponding atomic projected potentials and image simulations (defocus: -84nm; thickness: 4nm; white spots correspond to (unresolved) Si-C atom pairs).
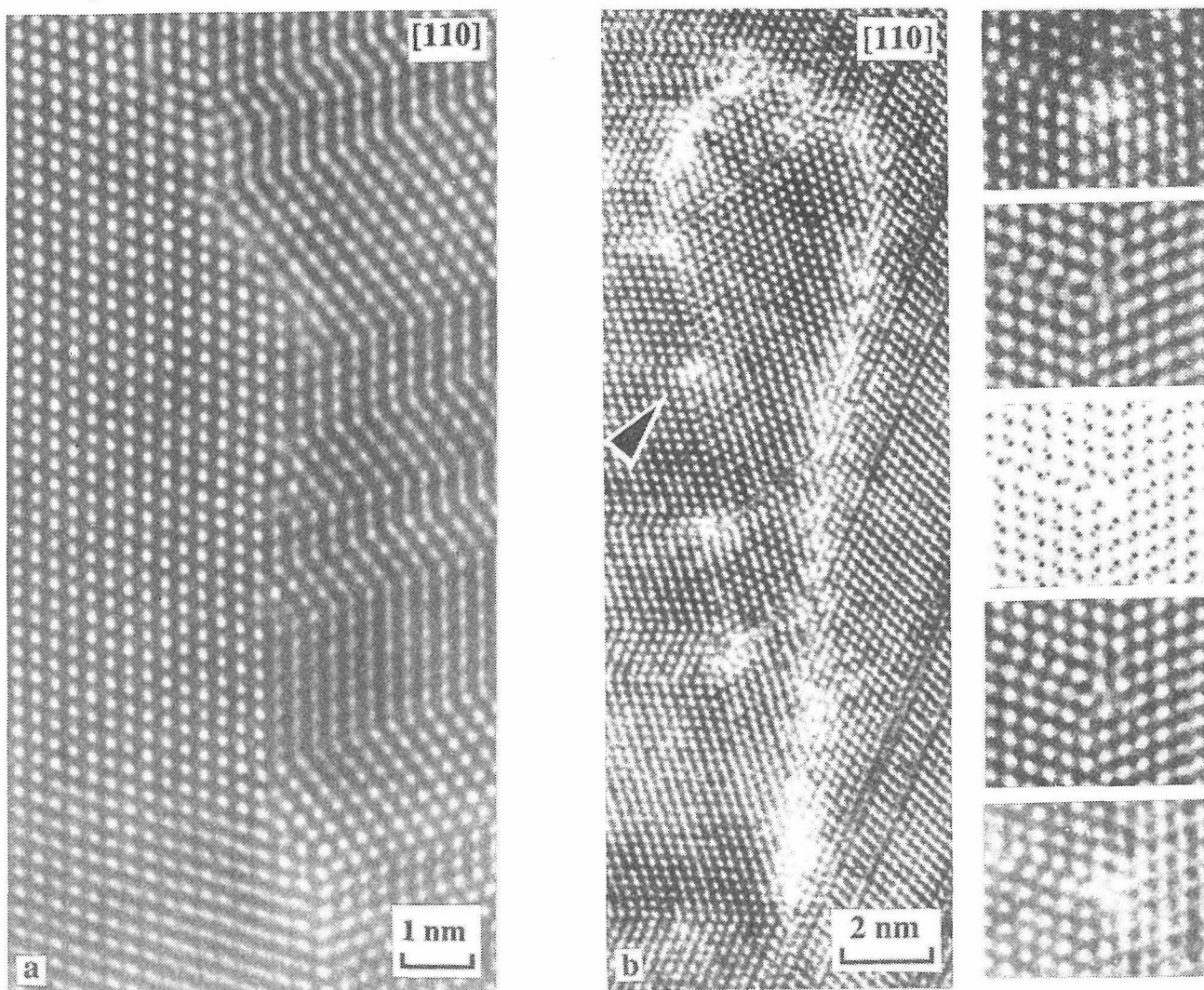
Figure 6. High-magnification HREM images of grain boundaries in SiC, viewed in [110] projection. a) β-3C/ α-polytypes transformation interface; b) Top right image: enlargement of the arrowed area (defocus: -114nm). Bottom right image: same region, observed with a slightly different focus (-118nm). The proposed structural model is shown in the centre, together with the corresponding computer simulations (thickness close to 5.5nm; "black" atoms).

- 73 -
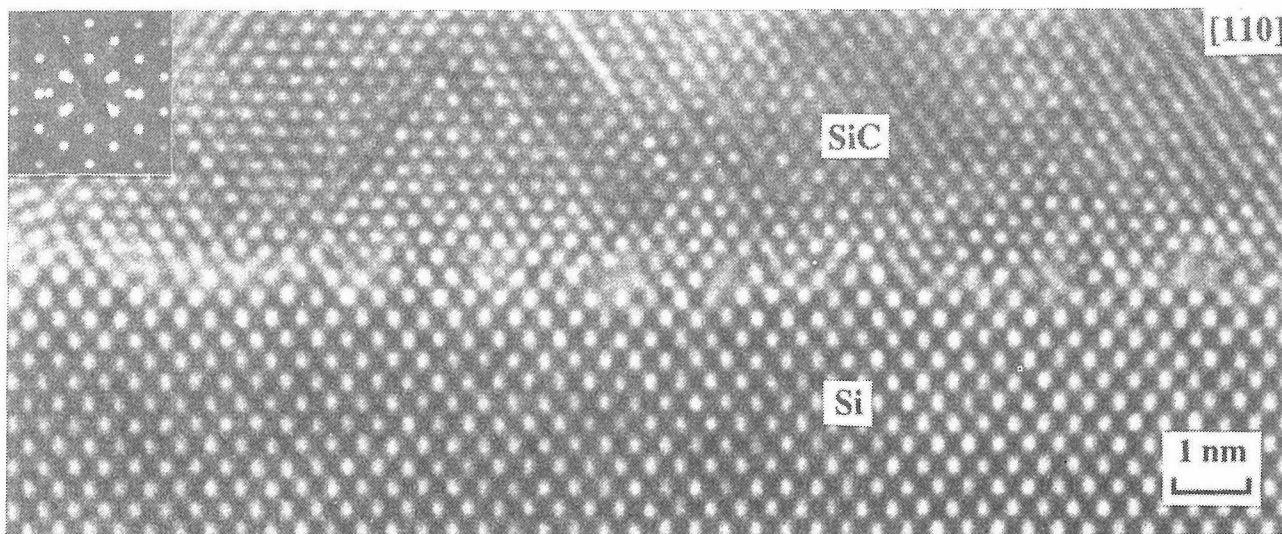
Figure 7. HREM image showing transverse cross-sectional view of as-grown SiC-on-Si. Note the complex twinning and stacking defects in SiC leading away from the interface and the absence of any amorphous layer at the interface itself. ED pattern (inset) demonstrating the orientation relationship between SiC and Si. Note also the regular array of Lomer dislocations.
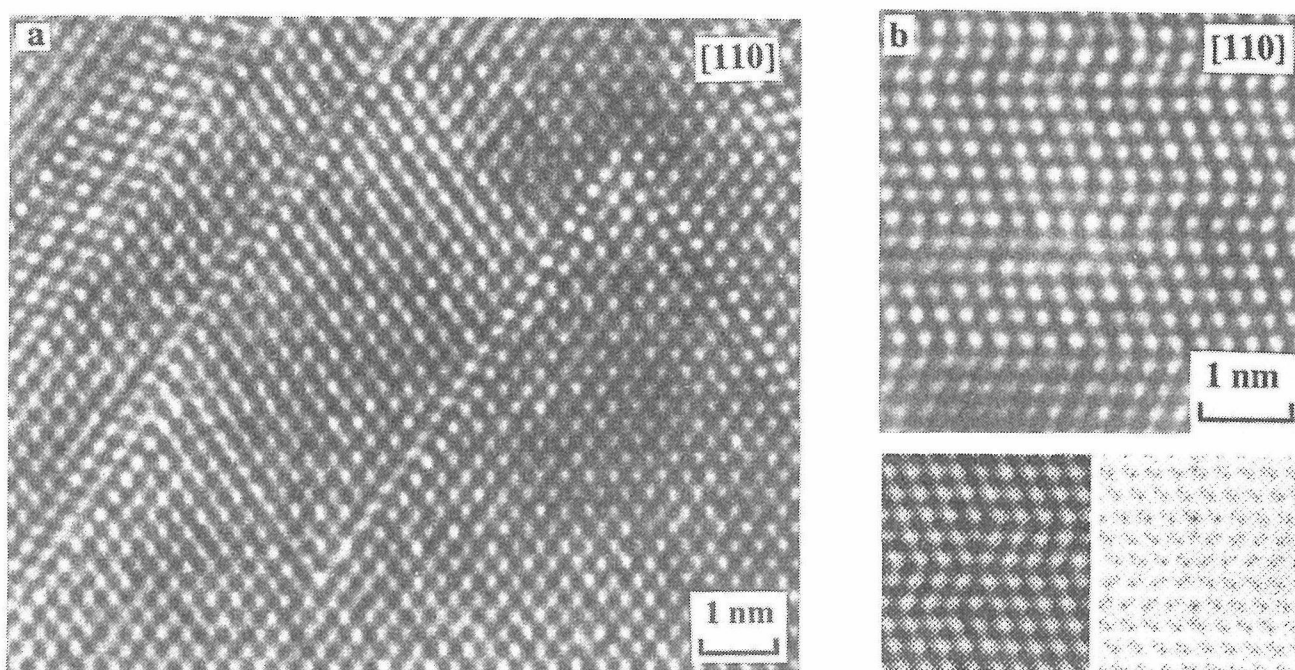
Figure 8. Atomic resolution images showing dislocations in SiC. A structural model is proposed to interprete the central image features seen in 8b (defocus: -84nm; thickness: 2nm; "white" atoms).

References

[1] B. Armas and C. Combescure, *Proc. 10th Int. Conf. on CVD* , (1987) 1060-1069.
[2] S. Schamm, A. Mazel, D. Dorignac and J. Sévely, *Microsc. Microanal. Microstruct.* , **2** (1991) 59.
[3] D. Dorignac, A. Mazel et al, *J. Eur. Ceram. Soc.*, **13** (1994) in press.
[4] B. Aspar, R. Rodriguez-Clemente et al., *J. Cryst. Growth* **129** (1993) 56-66.
[5] D. Tang and D. Dorignac, *Acta. Cryst. A* , **50** (1994) 45-52.
[6] V. Serin, G. Zanchi. and J. Sévely, *Microsc. Microanal. Microstruct.* , **3** (1992) 201-212.
[7] M.R. McCartney, R.A. ,Youngman and R. G. Teller, *Ultramicroscopy,* **40** (1992) 291-299.
[8] S. Abaïdia , V. Serin , G. Zanchi, Y. Kihn and J. Sévely , *Phil. Mag.* , submitted.
[9] P. Redlich, *Diplomarbeit (Stuttgart),* (1993).
[10] P. Pirouz and J. W. Wang, *Ultramicroscopy,* **51** (1993) 189-214.

Shock-Induced Phase Transformation Mechanism of Materials

Yasuhiko Syono

Institute for Materials Research, Tohoku University, Sendai 980, Japan

Abstract---Phase transformations due to displacive mechanism can be achieved within a short time of shock process because no extensive diffusion is involved, but generally revert during unloading. However, irreversibly formed metastable phases in the pressure release process provide a clue for the mechanism of shock-induced phase transformations. Typical examples for some simple oxide systems such as rutile-fluorite-α-PbO_2 or C-A-B type rare earth sesquioxides are demonstrated. Blocking mechanism for retaining shock-induced high pressure phases which is important for shock synthesis of new materials via phase transformations will also be discussed.

The shock compression technique has long been used for production of very high pressures exceeding 100 GPa and for determination of pressure-volume relation of condensed matter.[1] Shock compression is characterized by steep rise of shock pulse of ns time scale, followed by μs time scale hydrostatic regime. In the analysis of shock compression experiments of solids, hydrodynamic approximation was made using the conservation relation of mass, momentum and energy across the shock front and very good agreement with the compression data obtained by static high pressures is generally obtained. Owing to adiabatic compression, temperature is also increased instantaneously with the pressure rise and remarkable residual temperature persists even after the pressure release.

Phase transformations of solids induced by shock compression have also been observed in many substances and compared with those induced under static pressures.[2,3] The phase transformations inducible under shock compression should be due to fast reaction kinetics, since the shock duration is limited within a microsecond time scale in laboratory experiments.[4-6] Such fast transitions of electronic origin or displacive mecanism have been observed in many simple metals and compounds. The high pressure phases are generally back-transformed in the pressure release process and unquenchable. However, some irreversible phase transformations provide important information for the mechanism in the shock process.

One of the most thoroughly studied cases is the rutile-fluorite-α-PbO_2 transition in the shock process. Hugoniot measurements of TiO_2 with the rutile form revealed a phase transformation with about 15 % volume decrease, suggesting a fluorite structure as a possible high pressure phase.[7] Strong anisotropy in the transition pressures was also noted, i. e. lower transition pressures in the shock-loading perpendicular to the c-axis than that parallel to the c-axis. However, the recovered phase with the α-PbO_2 structure had a density only 2 % denser than rutile, indicating that it was not the high pressure phase and metastably formed in the shock release process.[8] Proposed displacive mechanism based on the topological relationship among the crystal structures of rutile, fluorite and α-PbO_2 successfully explained the observed anisotropy in the transition pressures. Direct evidence to support the proposed mechanism was obtained by TEM observation of lamellae consisting of rutile and α-PbO_2 in the shock-recovered products; Orientation relationship between coexisting rutile and α-PbO_2 was found to be exactly as expected from the proposed mechanism. Computer simulation of rutile-fluorite transition also revealed that the transition could occur within a picosecond time scale,

much shorter than the typical rise time of the shock front, and only with the uniaxial compression perpendicular to the c-axis.[9] Later static high pressure study confirmed that the high pressure phase has a tetragonally distorted fluorite structure, corroborating the above model.[10]

Recently similar shock-induced phase transformations were found to occur in the rare earth sesquioxides with the A, B and C type structures in the decreasing order of density.[11,12] Direct transition from C-type to A-type was observed under both shock and static pressures with about 10 % volume decrease. Transition pressures were found to be linearly decreased with cation to anion radius ratio, indicating the existence of critical cation to anion radius ratio for stabilizing the A-type structure. However, shock recovered phase was found to be with the B-type structure, which was presumably formed during the pressure release process, as schematically shown in Fig. 1. Similarity among the crystal structures of the A, B and C type was
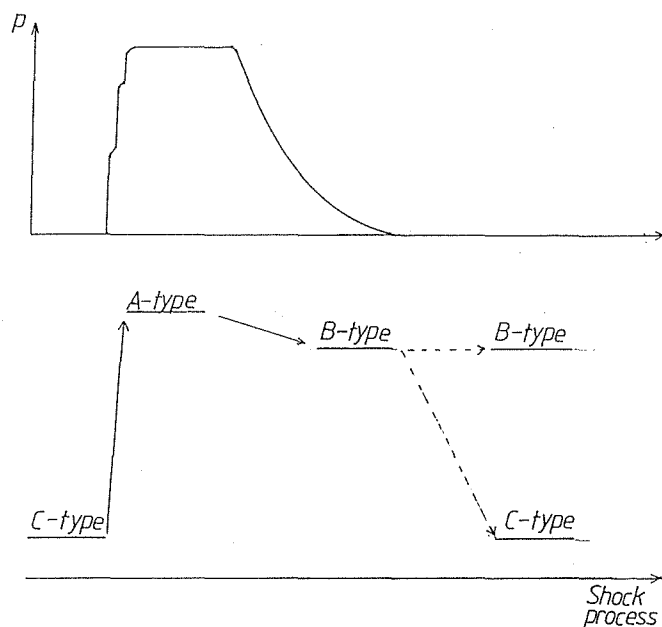
Fig.1 Schematic illustration of wave profile (top) and sequential C-A-B phase transformations of rare earth sesquioxides in the shock process (bottom).

pointed out, which makes the phase transformation due to displacive mechanism during shock process possible. Interestingly no direct transition from C-type to B-type could occur and the transformation attained only via most simple structure of the A-type. Sequential phase transformations of C-A-B type rare earth sesquioxidesin the shock process is quite analogous to those of rutile-fluorite-α-PbO$_2$ as mentioned above.

Complete retention of high pressure phases induced via displacive mechanism by shock loading seems to be rather difficult, since they are in general easily back-transformed during shock release process. Some blocking mechanism would be needed to stabilize the induced high pressure phase. The scheelite type ZrSiO$_4$ was successfully recovered from the shock loading of the zircon type ZrSiO$_4$.[13] It has been noted that zircon to scheelite transition is very similar to the rutile-fluorite transition, as far as the cation arrangements are concerned, as shown in Fig. 2.[14] Only difference is the coherent rotation of SiO$_4$ tetrahedra during the zircon-scheelite transition, which may play an important role in preventing back transition from shock-induced scheelite phase to the zircon phase during pressure release. A phase transformation due to similar block movement of atomic cluster was suggested in the case of shock formation of Cr$_3$Si (A15) type Nb$_3$Si from the Ti$_3$P type structure, although shock-yield of the high pressure phase was rather low.[15]
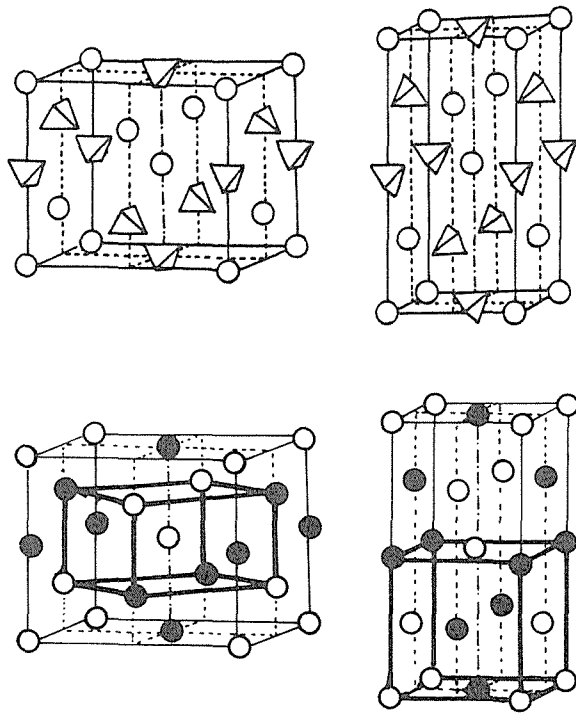
Fig.2 Schematic illustration of the crystal structures (top) of zircon (left) and scheelite (right) and their relationship (bottom) to rutile (left) and fluorite (right) which are indicated with bold lines respectively. Open and closed circles are Zr and Si atoms. SiO_4 tetrahedra are shown in the top figures.

The shock-induced A15 type Nb_3Si was found to have superconducting critical be temperature of 18 K, instead of non-superconducting Ti_3P type Nb_3Si.[16] This case shows importance of blocking mechanism in the shock-induced phase transformations, if they are intended for synthesis of new materials by shock-compression technique. In this regard worthy mentioning is that wBN can be synthesized from hBN,[17] while hexagonal form of diamond formed by shock loading of graphite is unquenchable.[18,19] This marked contrast suggests importance of bonding between different elements of B and N in preventing back-transformation from shock-induced wBN.

There have been long arguments whether the olivine-spinel transformation is due to diffusion-controlled nucleation-growth mechanism or martensitic mechanism. From the viewpoint of shock compression experiments, no martensitic mechanism seems to work in the shock process, since no anomaly around the phase transition pressures determined by static high pressure-temperature studies was ever noticed in the Hugoniot measurements of forsterite.[20-22] This strongly suggests that the phase transformations of the reconstructive nature is hardly achieved during a short time interval of the shock process. Even an order-disorder phse transformation with cation rearrangements seems to be unfavorable under shock compression; The disordered rutile type $FeTaO_4$ was found to transform to the disordered α-PbO_2 type, instead of the ordered $NiWO_4$ type structure obtainable by static high pressure experiments.[23] Interestingly MD calculation of forsterite revealed a pressure-induced phase transformation.[24] This might correspond to the observed Hugoniot anomaly above about 80GPa, which has previously been believed to be disproportionation of Mg_2SiO_4 to $MgSiO_3$ perovskite plus MgO.

In conclusion shock compression attains extreme high pressure condition within a short time interval and therefore unique response of materials is expected. To understand the real nature of shock compressed states is not only scientifically interesting, but also has a potential technological application. In the present article, the discussion is restricted to the shock-induced phase transformation. However, many other aspects of applications of shock compression techniques such as shock compaction and chemical reactions of powder materials are developing now, and further progress in near future is very promising.

References
[1] G. E. Duvall and G. R. Fowles, High Pressure Physics and Chemistry, R. S. Bradley (ed.), Academic, New York (1963) vol.2, p.209.
[2] G. E. Duvall and R. A. Graham, Rev. Mod. Phys., 49 (1977) 523.
[3] R. G. McQueen, S. P. Marsh, J. W. Taylor, J. N. Fritz and W. J. Carter, High Velocity Impact Phenopmena, R. Kinslow (ed.), Academic, New York (1970) p.293.
[4] Y. Syono, High Pressure Explosive Processing of Ceramics, R. A. Graham and A. B. Sawaoka (eds.), Transtech, Aedermansdorf (1986) p.377.
[5] Y. Syono, Shock-Waves in Condensed Matter-1987, S. C. Schmidt and N. C. Holmes (eds.), North Holland, Amsterdam (1988) p.19.
[6] Y. Syono, K. Kusaba, T. Atou and K. Fukuoka, Shock Waves, K. Takayama (ed.), Springer, Berlin (1992) vol.1, p.121.
[7] Y. Syono, K. Kusaba, M. Kikuchi, K. Fukuoka and T. Goto, High Pressure Research in Mineral Physics, M. H. Manghnani and Y. Syono (eds.), Terra/AGU, Tokyo/Washington, D. C. (1987) p.385.
[8] K. Kusaba, M. Kikuchi, K. Fukuoka and Y. Syono, Phys. Chem. Miner., 15 (1988) 238.
[9] K. Kusaba, Y. Syono and Y. Matsui, Shock Waves in Condensed Matter-1989, S. C. Schmidt, J. N. Johnson and L. W. Davison (eds.), North Holland, Amsterdam (1990) p.135.
[10] H. Sato, S. Endo, M. Sugiyama, T. Kikegawa, O. Shimomura and K. Kusaba, Science, 251 (1990) 786.
[11] T. Atou, K. Kusaba, K. Fukuoka, M. Kikuchi and Y. Syono, J. Solid State Chem., 89 (1990) 378.
[12] T. Atou, M. Kikuchi, K. Fukuoka, K. Kusaba and Y. Syono, Proc. of the 1993 joint AIRAPT/APS Topical Conference on High Pressure Science and Technology, Colorado Springs (1994), in press.
[13] K. Kusaba, Y. Syono, M. Kikuchi, and K. Fukuoka, Earth Planet. Sci. Lett., 72 (1985) 433.
[14] K. Kusaba, T. Yagi, M. Kikuchi and Y. Syono, J. Phys. Chem. Solids, 47 (1986) 675.
[15] B. Olinger, Acta Cryst., A38 (1982) 151.
[16] S. Ohshima, T. Wakiyama, T. Goto and Y. Syono, Jpn. J. Appl. Phys., 22 (1983) 264.
[17] T. Soma, A. Sawaoka and S. Saito, Mater. Res. Bull., 9 (1974) 755.
[18] D. J. Erskine and W. J. Nellis, Nature, 349 (1991) 317.
[19] M. Yoshida and N. N. Thadhani, Shock Compression of Condensed Matter 1991, S. C. Schmidt et al. (eds.), North Holland, Amsterdam (1992) p.585.
[20] I. Jackson and T. J. Ahrens, J. Geophys. Res., 84 (1979) 3039.
[21] Y. Syono, T. Goto, J. Sato and H. Takei, J. Geophys. Res., 86 (1981) 6181.
[22] J. M. Brown, M. D. Furnish and R. G. McQueen, High Pressure Research in Mineral Physics, M. H. Manghnani and Y. Syono (eds.), Terra/AGU, Tokyo/Washington, D. C. (1987) p.373.
[23] K. Kusaba, K. Fukuoka and Y. Syono, J. Phys. Chem. Solids, 52 (1991) 845.
[24] S. Tsuneyuki, pivate communication.

Structures and Properties of Materials Recovered from High Shock Pressures

W.J. Nellis

Lawrence Livermore National Laboratory, University of California, Livermore, California 94550, U.S.A.

Abstract

Shock compression produces high dynamic pressures, densities, temperatures, and their quench rates. Because of these extreme conditions, shock compression produces materials with novel crystal structures, microstructures, and physical properties. Using a 6.5-m-long two-stage gun, we perform experiments with specimens up to 10 mm in diameter and 0.001 – 1 mm thick. For example, oriented disks of melt-textured superconducting $YBa_2Cu_3O_7$ were shocked to 7 GPa without macroscopic fracture. Lattice defects are deposited in the crystal, which improve magnetic hysteresis at ~1 kOe. A computer code has been developed to simulate shock compaction of 100 powder particles. Computations will be compared with experiments with 15-20 μm Cu powders. The method is applicable to other powders and dynamic conditions.

Introduction

Shock compression produces dynamic pressures up to the Mbar range, compressions up to a few tens of percents, and temperatures up to a few 1000 K. Dynamic pressure is applied for about a μsec. Strain rates on compression are very high, reaching above 10^8/s. Quench rates on release of pressure are also very high, ranging up to about 10^9 K/s and 10^{12} bar/s. Because of these extreme conditins and rates, shock compression produces material with novel crystal structures, microstructures, and physical properties.

Using a 6.5-m-long two-stage light gas gun with a 20 mm bore, we accelerate projectiles (impactors) up to 4 km/s. When such a projectile impacts a target, pressures from 1–100 GPa (0.01–1 Mbar) are generated, depending on materials and impactor velocity. Impactors typically weigh 5-10 g and so it is straight forward to contain the kinetic energy and momentum of the impactor in a fixture containing the specimen.[1,2] Specimens are typically 10 mm in diameter and 0.001 to 1 mm thick. As an example, 1 μm thick films have been recovered intact from 100 GPa shock pressure.[3] With our 35 mmbore two-stage gas gun larger diameter specimens can be used, although maximum velocities and impact pressures are lower.

In this paper we give two examples. The first example shows that a disk of a brittle ceramic oxide can be shocked to relatively high pressures without macroscopic fracture, that is, without breaking the oxide disk. The high strain rates induce shock defects, which change the properties. In this case, the disk is a high-temperature superconductor and the physical property is the magnetic hysteresis ΔM induced in the disk by an applied magnetic field. The second example is the combination of the development of a computer code to simulate the dynamic compaction of 100 individual powder particles and the comparison of the computations with the results of gas-gun experiments using Cu powders as a simple test material.

Bearings made from new high-transition-temperature (high-T$_c$) superconducting oxides are a possible application of these new superconductors. External magnetic fields are generated in such bearings by superconducting magnetic fluxoids which should be strongly pinned in the lattice to prevent dissipative losses. The purpose of a superconducting bearing is not to transport high currents and thus the problem of relatively small intergranular critical current density in polycrystalline oxide super-conductors is minimized. However, intragranular critical current density needs to be increased by increasing the number and strength of flux-pinning sites within the lattice. In so doing, the magnetic field which can be generated and sustained by a bearing material is increased. High densities of lattice defects are induced in shock-compacted powders of YBa$_2$Cu$_3$O$_7$ and the dislocations and stacking faults generated are effective in increasing flux-pinning energies and intragranular critical current densities.[4] However, an effective technique is needed to shock-induce lattice defects and ΔM in high-T$_c$ oxides, which does not fracture the specimen. These defects should enhance flux-pinning energies and intragranular critical current densities.

An attractive material to investigate is YBa$_2$Cu$_3$O$_7$. An ideal form of YBa$_2$Cu$_3$O$_7$ to investigate is melt-textured material because it consists of large disk-shaped grains several mm across and several 10 μm thick, in which the c axis of the orthorhombic crystal structure is along the thin direction of each disk-shaped grain. Superconducting fluxoids point preferentially along the c axis, and these grains are preferentially aligned in melt-textured YBa$_2$Cu$_3$O$_7$.

Our objective is to shock-induce lattice defects in a crystallographicaly aligned disk without fracture, at least on a macroscopic scale. In this way, an oriented shocked specimen can be annealed and its superconducting properties measured in a straight forward manner. The slip planes in YBa$_2$Cu$_3$O$_7$ are in the basal plane of the orthorhombic crystal structure.[5] Thus, shocking YBa$_2$Cu$_3$O$_7$ powders causes increasing fracture with increasing pressure,[6] because the slip planes are randomly oriented. Shocking a disk-shaped single crystal along the c axis normal to the plane of the specimen is expected to fracture it into many small pieces, since no slip direction is available along the shock direction. On the other hand, a small YBa$_2$Cu$_3$O$_7$ single crystal shocked at 45° from the basal plane broke into only a few pieces which were heavily defected.[7] Thus, controlling the crystallographic orientation of a specimen with respect to the shock direction is an effective way to control fracture while shock-inducing defects.

For this reason, a dense melt-textured YBa$_2$Cu$_3$O$_7$ specimen disk 7.7 mm in diameter and 1.1 mm thick was embedded in a steel recovery capsule, which in turn was embedded in a steel fixture, and shocked to 6.6 GPa at an angle of 30° with respect to the average c-axis direction of YBa$_2$Cu$_3$O$_7$. The velocity of the lexan projectile was chosen to give the desired impact pressure in steel. The experiment is illustrated in Fig. 1; in this configuration the direction of shock propagation is about 30° from the average c-axis direction of the disk-shaped melt-textured YBa$_2$Cu$_3$O$_7$.

The shock pressure in the oriented melt-textured YBa$_2$Cu$_3$O$_7$ disk produced a one-piece specimen. The specimen was easily handled without breaking for post-shock annealing and SQUID magnetometer measurements. The shock pressure did not change the superconducting transition temperature of 92 K.
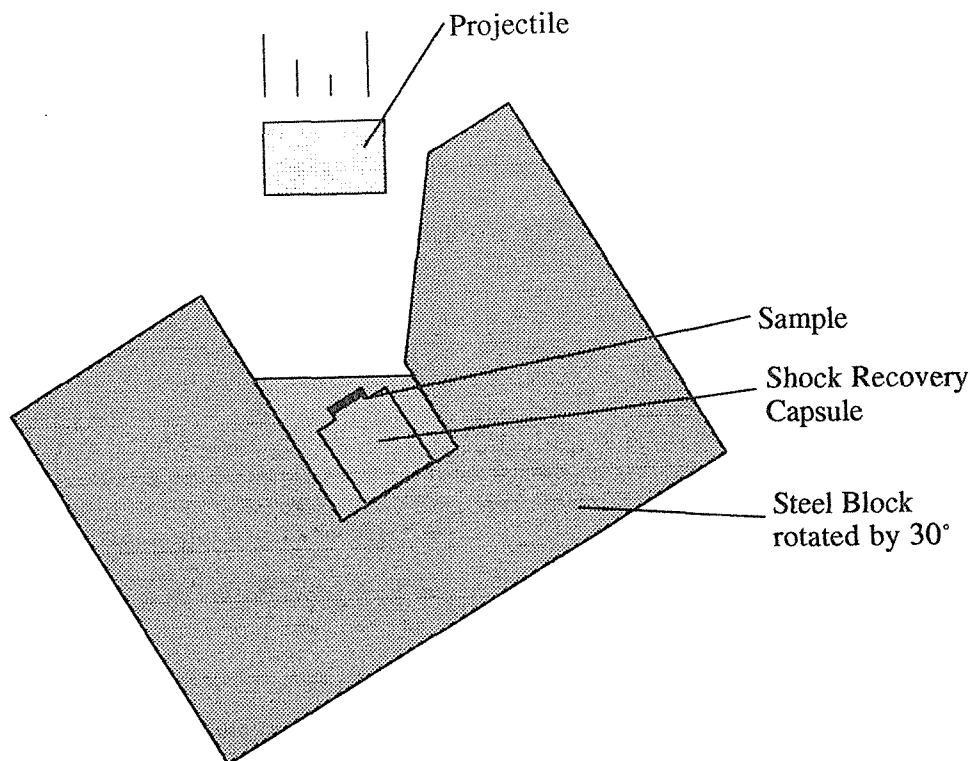
Figure 1. Schematic of fixture to shock a disk-shaped specimen of melt-textured $YBa_2Cu_3O_7$ without macroscopic fracture.

Magnetic moment induced in the specimen was measured at 70 K as a function of applied magnetic field up to 40 kOe. Magnetic hysteresis ΔM is the difference in magnetic moment M induced on increasing and decreasing applied magnetic field H. Magnetic hysteresis is sensitive to shock-induced changes in microstructure and, thus, to changes in critical current density. At an applied magnetic field of 1 kOe, annealing the specimen in oxygen was found to increase the magnetic hysteresis of the specimen relative to the initial state. Thus, the ability of the shocked and annealed specimen to act as a magnetic-bearing material is enhanced.

Magnetic hysteresis ΔM versus applied magnetic field was measured initially, after shocking, and after successive heat treatments in oxygen at 890° C for various times, followed by 4 hours in oxygen at 450°. The results for an applied field of 1 kOe are plotted in Fig. 2 as ΔM versus cumulative annealing time at 890° C. The dashed baseline in Fig. 3 is the reference result for the unshocked specimen. At zero annealing time the lower ΔM point is for the as-shocked specimen; the upper ΔM point near zero corresponds to 10 minutes at 890° C. After a cumulative annealing time of 15 hours, ΔM is enhanced over the starting value. An ehancement of about 15% is observed after a cumulative annealing time of 48 hours.

These results show that the brittle oxide $YBa_2Cu_3O_7$ can be shocked to 6.6 GPa without macroscopic fracture, provided the disk-shaped specimen is in the preferentially oriented melt-textured form and is shock-compressed at an angle of about 30° from the effective c axis of the orthorhombic-phase specimen. Subsequent anneals in oxygen at
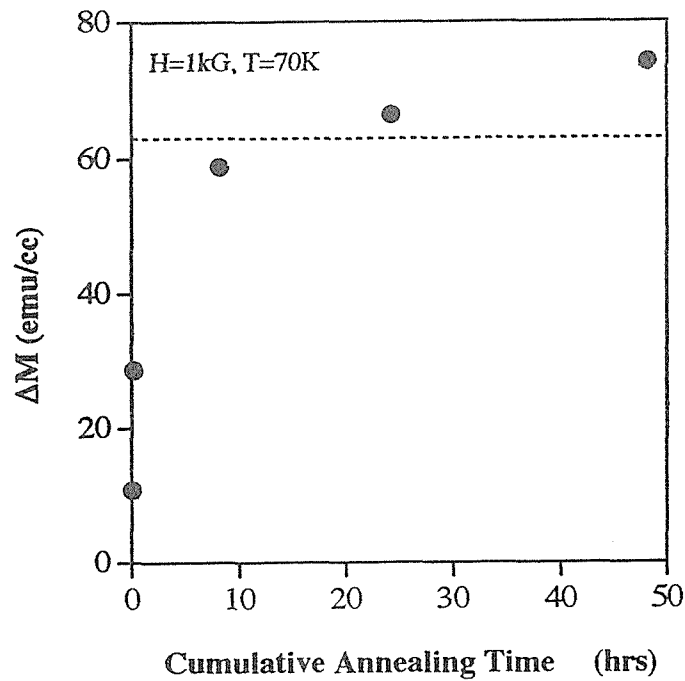
Figure 2. Magnetic hysteresis DM at 1 kOe and 70 K versus cumulative annealing time at 890° C in oxygen for the specimen shocked to 6.6 GPa. The lower DM point at zero annealing time is for the as-shocked specimen; the upper DM point near zero time corresponds to 10 minutes at 890° C.

890° C produce a magnetic hysteresis which is enhanced relative to the initial unshocked state, as expected for shock-induced dislocations and stacking faults.[4] This work is described in more detail elsewhere.[8]

Dynamic Compaction of Powders

The dynamic compaction of powders is a technique to produce a wide variety of dense ceramic, metallic, and other specimens with potentially novel properties.[9-13] The method, for example, is attractive to consolidate nanocrystalline powders without grain growth. In this method consolidation is achieved by dynamic high pressures which densify powders and last for very brief times of ~1 μs. The fast time scale offers the opportunity to consolidate fine-grained powders, which do not have time to increase their grain size. The fast time scale also produces heterogeneous surface heating on particle boundaries, high quench rates and possible interfacial bonding between particles. Several phenomenological models have been developed to describe the process.[9-11] However, a generalized computational simulation is needed which can test various ideas and guide experiments to produce dense compacts. In this way, a wide variety of issues could be addressed computationally, including heterogeneous pressures, temperatures, and and their quench rates for various particle-size distributions, plastic flow, fracture, and phase transitions.

For this reason we initiated development of a computer simulation of the compaction of powders to iterate with experimental results. This computational model was developed in collaboration with Dr. David Benson. Copper was chosen as a test material because i)

Cu is a relatively simple material with an available material model at high shock pressures,[13] ii) real-time shock compression data are available for porous Cu for comparison with computation,[14] and iii) Cu powders are readily available for experiments to compare observed changes in particle shape with computational predictions.

In this model about 100 powder particles of a given size distribution and average initial porous density fill a box using a Monte Carlo method and the particles are compressed dynamically using an Eulerian computer code. The equation of state and constitutive model of each solid particle, initially at normal density, are those of Cu. The initial computations were performed in two dimensions, which require less computer time than three dimensions. The initial size of the box containing the particles is 160 μm with 100 Eulerian zones on a side. The particle sizes were chosen as in the experiment described below. The consolidation was calculated for a compressive wall velocity of 0.2 km/s or about 2 GPa shock pressure in Cu powder of density 6.1 g/ cm^3.

In order to test the computational predictions, spherical Cu powders 15-20 μm in diameter were dynamically compacted using a 6.5-m-long two-stage light-gas gun. The powder specimens were 10 mm in diameter and 0.5 mm thick and were placed in a steel capsule. For comparison of experiment with calculation, we use the fact that most of the internal energy and consolidation are achieved in the powder in the first shock wave. The computed single-shock compaction is, thus, compared with results from experiments in which compaction is achieved by a reverberating shock wave in the 0.5 mm thick specimen. Measured initial powder density was 6.1 g/cm^3. Shock compression data for porous Cu[14] and the standard shock-impedance-match method were used to estimate the impact velocity of the lexan plastic projectile required to obtain the wall velocity used in the computation. The photomicrograph result for a wall velocity of 0.2 km/s, a lexan impact velocity of 1.1 km/s, and a first shock wave in the powder of 2 GPa is in good agreement with the computation.[15, 16]

In summary the computational results for Cu powders are in good agreement with experimental observations of the shapes of particles consolidated at pressures up to a few GPa,which shows that the simulation is accurate up to a few GPa. The computational method could be generalized to other materials, size distributions, compaction rates, and higher pressures.

Acknowledgments

References

1.   J. J. Neumeier, W. J. Nellis, M. B. Maple, M. S. Torikachvili, K. N. Yang, J. M. Ferreira, L. T. Summers, J. I. Miller and B. C. Sales, High Pressure Res. 1, 267 (1989).

2. A. J. Gratz, W. J. Nellis, J. M. Christie, W. Brocious, J. Swegle and P. Cordier, Phys. Chem. Minerals 19, 267 (1992).

3. R. Koch, W. J. Nellis, J. W. Hunter, H. Davidson and T. H. Geballe, Pract. Met. 27, 391 (1990).

4. S. T. Weir, W. J. Nellis, M. J. Kramer, C. L. Seaman, E. A. Early and M. B. Maple, Appl. Phys. Lett. 56, 2042 (1990).

5. M. J. Kramer, L. S. Chumbley and R. W. McCallum, J. Mat. Sci. 25, 1978 (1990).

6. W. J. Nellis, C. L. Seaman, M. B. Maple, E. A. Early, J. B. Holt, M. Kamegai, G. S. Smith, D. G. Hinks and B. Dabrowski, High Temperature Superconducting Compounds: Processing and Related Properties, Warrendale, PA: TMS Publications, 1989, pp. 249-264.

7. S. T. Weir, W. J. Nellis, C. L. Seaman, E. A. Early, M. B. Maple, M. J. Kramer, Y. Syono, M. Kikuchi, P. C. McCandless and W. F. Brocious, Shock-Wave and High-Strain-Rate Phenomena in Materials, New York: Dekker Press,1992, pp.795-808.

8. W. J. Nellis, S. T. Weir, N. A. Hinsey, U. Balachandran, M. J. Kramer and R. Raman, to be published in the proceedings of the AIRAPT/APS High Pressure conference, June 28-July 2, 1993, Colorado Springs.

9. C. F. Cline and R. W. Hopper, Scripta Met. 11, 1137 (1977).

10. W. H. Gourdin, J. Appl. Phys. 55, 172 (1984).

11. V. F. Nesterenko and A. V. Muzykantov, Sov. Combust. Explos. and Shock Waves 21, 730 (1985).

12. E. K. Beauchamp, M. J. Carr and R. A. Graham, J. Am. Ceram. Soc. 68, 696 (1985).

13. D. J. Steinberg and M. W. Guinan, J. Appl. Phys. 51, 1498, (1981).

14. LASL Shock Hugoniot Data, edited by S. P. Marsh, University of California Press, Berkeley, 1980.

15. D. J. Benson and W. J. Nellis, submitted, 1993.

16. D. J. Benson, Comp. Meth. Appl. Mech. Eng. 99, 235 (1992).

Microscopic Observations of Shock Compression in Powders

M. Yoshida

High Energy Density Laboratory
National Institute of Materials and Chemical Research
Tsukuba, Ibaraki 305, Japan

Abstract

Spherical copper powders of different sizes were shock compressed and their shock-wave fronts were microscopically observed. The recording system employed an electronic streak camera and a liquid-nitrogen cooled CCD camera. Standardised shocked argon light source was first recorded to calibrate the optical sensitivity of the recording system and the brightness temperature profile of the event was deduced. It was observed that coarse spherical powders yield very high temperature and very rapid cooling rate at the shock front. For spherical copper powders with diameter of 500 μm, maximum brightness temperature and temperature cooling rate of approximately 2.0×10^4 K and 10^{12} K/s, respectively, were observed at 43 GPa bulk shock pressure.

1. Introduction

Shock compression is inherently accompanied by heterogeneous energy deposition, resulting in non-equilibrium state at the shock front followed by relaxation processes during, and in some cases even after, compression. The existance of heterogeneity in shock compression has long and widely been recognized through many studies such as detonation initiation of explosives [1], recovery analyses of powder materials [2, 3], shock induced chemical reactions in organic substances [4, 5], molecular dynamic simulations [6], and so on.

In shock syntheses of diamond, this heterogeneous nature of shock compression has been fully utilized to increase the yield of diamond [7]. Graphite or graphite-like carbon was mixed with spherical copper powders and was shock compressed to 30 to 40 GPa. The yield of diamond exceeded 70 %. The same method has been extended successfully to shock syntheses of cubic boron nitride [8] and cubic BN-C solid solutions [9].

These shock synthesis studies have promoted a microscopic investigation of heterogeneous processes in shock compression of powders. Here we report our first preliminary experimental results on copper powders. Graphite or any other material was not mixed and pure copper powders were shock compressed and their shock wave fronts were observed by a streak camera.

2. Experimental

Spherical copper powders with purity of 99.9% were hand-tapped into a cylinder of 20 mm in diameter and formed a disk of 2 ~ 3 mm in thickness. Irregular shape copper powder was also used for comparison purpose. Table 1 lists copper powders employed in this study. The initial loading density geometrically measured was approximately 65 % of the solid.

An explosive plane-wave generator with effective planar area of 100 mm in diameter initiated a liquid explosive, nitromethane, to accelerate a 2 mm thick aluminum-alloy (6061) flyer plate. Target plate was the same 2 mm thick 6061 Al plate on which a sample disk of copper powder was attached. The flyer plate velocity was 3.7 km/s. This shock system was mainitained the same in all the powder compression experiments reported here.

Impact of the flyer plate generates 40 GPa shock pressure in a target plate. The shock pressure in the sample is estimated to be 43 GPa from impedance mismatch between 6061 Al and copper powder. When the shock wave reaches the interface between copper powder and the fused-quartz window, very strong light pulse can be observed followed by relatively weak light. The strong light is attributed to heterogeneous structure of the shock front in powders. The weak light is from equilibrated compressed state of the shocked powder and it endures until the rarefaction wave from the back surface of the flyer plate decreases the pressure and the temperature at the interface. The brightness of the weak light is usually two to three orders of magnitude smaller than the first strong light pulse and it is difficult to record both lights

simultaneously with sufficient accuracy. As the interest is in the heterogeneity at the shock front, only the strong light pulse is recorded by a recording system described in the followings.

An image converter camera (Imacon 700, Hadland Photonics Ltd.) with streak rate of 50 ns/mm resolved the events temporary. The streak image on the phospher screen of the streak camera was recorded by a liquid-nitrogen cooled CCD camera (Model 3200, Astromed Ltd.) with 1152 × 770 pixels and 16 bits resolution of photo-electrons in each pixel. Time resolution was typically 3 ~ 5 ns.

Two lens systems were employed. For a low magnification case a lens of 600 mm focal length formed an image on a photocathode of the image converter camera with magnification ratio of approximately 0.22. For a high magnification case, an objective – camera lens combination with maximum 12 times magnification ratio formed an microscopic image of powders. Spatial resolution as good as 3 to 4 μm was attained in this case.

The evaluation of spatial and temporal profiles of brightness of the events requires a standard light source to calibrate the optical sensitivity of the recording system. As the sensitivity depends on the streak rate, the standard light source is to be recorded with the same streak rate as the experiments. This disables the usage of a black–body furnace or a standard lamp because their brihghtness is usually a couple of orders of magnitudes weaker than the events. We employed an argon plasma generated by shock compression as a standard light source. The argon plasma is considered to be a black–body light source. Calibration of spectral brightness of shocked argon has been described previously [10] and will not be detailed here. The temperature can be controlled accurately in a range between 12,000 and more than 20,000 K and with accuracy of ±500 K by changing the shock wave velocity.

Before each shock compression observation, light emission of shock compressed argon plasma was recorded with a bandpass filter (420 ± 5 nm) and the same optical components. For the components to be replaced in each experiment, such as PMMA blast–proof window, mirrow and fused–quartz, materials from the same lot are employed.

3. Results and Discussion

A typical record at 420 ± 5 nm wavelength for low magnification case is shown in Fig. 1. Two samples were shock loaded simultaneously. Peak intensity at each spatial point was deduced to temperature by assuming black–body radiation and comparing the photo-electron counts to the counts obtained for the standard argon plasma light source with known brightness. Table 2 summerizes the results for low magnification observations. A 25 μm camera slit limits the spatial resolution to approximately 110 μm at powder/fused–quartz interface. This resolution did not allow us to resolve events microscopically for powders of 100 μmϕ or less. Obtained brightness temperatures for powders A and B are averaged over hot and cold areas as well. For the powder D, the spatial resolution is an order of magnitude smaller than the particle size, 1 mmϕ, and reflects well–resolved temperature profile of the event. The observed temperature, $(1.7 \pm 0.1) \times 10^4$ K is approximately four times of the calculated temperature.

To obtain better spatial resolution, an objective–lens and a camera–lens combination was employed. The focal lengths of the objective and the camera lenses were 50 and 600 mm, respectively. This lens system magnified the image to maximum 12 times. Spatial resolution was 3 to 4 μm and a little worse than the theoretically calculated value due possibly to optical qualities of a blast–proof PMMA window and other optical components. Figure 2 shows an observed streak camera image for a 500 μmϕ copper powder. The slit lies on a center of one copper powder. The maximum temperature was attained at the center of the powder and was $(2.0 \pm 0.2) \times 10^4$ K. Maximum quench rate was also at the center of the powder and was approximately 10^{12} K/s.

Although more experiments are required to extract a quantitative model for shock compression process in powders, there are two notable observations.

One is the rise time of the shock front. In many theoretical analyses [11, 12, 13, 14] of shock compression in powders, it is often assumed that the shock rise-up is rather smooth and the order of rise-up time is the shock transit time over the diameter length. The irregularity of the shock wave front roughly corresponds to the shock transit time over the diameter length. (Calculated transit time for 500 μm is 120 ns.) Fig. 2 exhibits that rise-up is approximately one third of the calculated value; light intensity reaches to the maximum in about a couple of tens of nanoseconds and then falls within time duration a little longer than the rise-up.

The other is the dependence of the maximum temperature value on powder diameter. As the specific internal and kinetic energies are independent to powder sizes and morphologies, the same amount of energy is to be deposited regardless to the size of the powder. If we assume that the energy deposition occurs mainly on the surface of the powders and the thickness of the layer of energy deposition does not depend on the size of the powder, the peak temperature should increase in proportion to the diameter of the powder because the specific surface area is inversely proportional to the diameter of the powder. However, this is inconsistent with observations. The observed maximum temperatures for 1 mmϕ and 500 μmϕ spherical copper powders are essentially the same within the experimental error. If we take the result of 100 μmϕ powder as a maximum temperature and compare that with the result of 1 mmϕ powder, the ratio of specific surface area of 10 produced only 1.7 times difference in temperature. The temperature difference will even be smaller as the result for 100 μm is averaged over hot and cold areas.

4. Conclusions

Shock compression in spherical copper powders is microscopically observed. The best spatial and temporal resolutions were 3 to 4 μm and 3 to 5 ns, respectively. Time resolved brightness temperature profiles were measured using standardized argon plasma light source at 420 nm. Maximum temperature between 1.2 and 2.0 $\times 10^4$ K were obtained for 100 μm to 1 mm diameter copper powders. The experiments are still to be evolved to various powders to obtain detailed understandings of heterogeneous nature of shock compression in powders.

References

[1] A.W.Campbell, W.C.Davis, J.B.Ramsay, and J.R.Travis, *Phys. Fluid* **4**, 498 (1961).

[2] R.A.Graham, B.Morosin, E.L.Venturini, and M.J.Carr, *Ann. Rev. Mater. Sci.* **16**, 315 (1986).

[3] N.N.Thadhani, *Progress in Materials Science* **37**, 117 (1993).

[4] A.N.Dremin and L.V.Babare, in *"Shock Waves in Condensed Matter — 1981"*, W.J.Nellis, L.Seaman, R.A.Graham eds., American Institute of Physics, p. 657 (1982).

[5] D.D.Dlott and M.D.Fayer, *J. Chem. Phys.* **92**, 3798 (1990).

[6] D.W.Brenner, in *"Shock Compression of Condensed Matter 1991"*, S.C.Schmidt, R.D.Dick, J.W.Forbes, and D.G.Tasker eds., Elsevier Science Publishers B. V., Amsterdam, p. 115 (1992).

[7] S.Fujihara, K.Narita, Y.Saito, K.Tatsumoto, S.Fujiwara, M.Yoshida, K.Aoki, Y.Kakudate, S.Usuba, and H.Yamawaki, in *"Shock Waves"*, K.Takayama ed., Springer-Verlag, Berlin, p. 367 (1992).

[8] M.Yoshida, S.Fujiwara, and S.Fujihara, New Diamond **30**, 30 (1993).

[9] Y.Kakudate, M.Yoshida, S.Usuba, H.Yokoi, S.Fujiwara, M.Kawaguchi, K.Sako, and T.Sawai, in *"Proceedings of Third IUMRS Int. Conf. Adv. Mater. "*, in press.

[10] Y.Nakayama, M.Yoshida, Y.Kakudate, S.Usuba, H.Yamawaki, K.Aoki, K.Tanaka, and S.Fujiwara, in *"Proceedings of International Workshop on Strong Shock Waves"*, p. 77 (1991).

[11] D.G.Morris, *Metal Sci.* **16**, 457 (1982).

[12] W.H.Gourdin, *J. Appl. Phys.* **55**, 172 (1984).

[13] R.B.Schwarz, P.Kasiraj, T.Vreeland Jr., and T.J.Ahrens, *Acta Metal.* **32**, 1243 (1984).

[14] K.Kondo and S.Sawai, *J. Am. Ceram. Soc.* **73**, 1983 (1990).

Table 1

Copper powders

Powder	Diameter	Remarks
A	$< 100 \mu m$	irregular
B	$100 \mu m$	spherical
C	$500 \mu m$	spherical
D	1 mm	spherical

Table 2

Results of peak temperature measurements
(at 420 ± 5 nm)

Powder	Temperature (10^3 K)
A ($< 100 \mu m$, irregular)	7 ± 0.5
B ($100 \mu m \phi$, spherical)	12 ± 0.3
D ($1 mm \phi$, spherical)	17 ± 1
(Calculated)	4.0
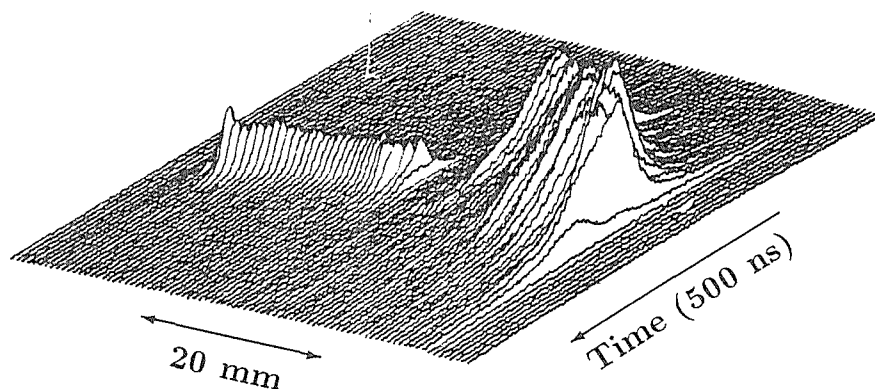
Fig. 1　A typical streak record of the shock wave front in 100 $\mu m \phi$ (left) and 1 mmϕ (right) powders.
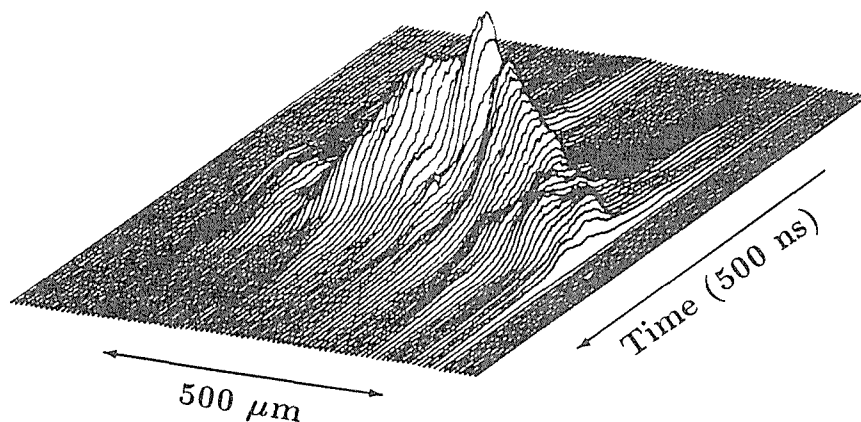
Fig. 2　A streak record of the shock front structure for a maginified 500 $\mu m \phi$ copper spherical particle.

Super Diamond Project at NIRIM

Yusuke Moriyoshi

National Institute for Research in Inorganic Materials, 1-1 Namiki, Tsukuba, Ibaraki 305, Japan

In 1993, a new research project, "Super Diamond", began at NIRIM. This five year project is devoted to producing cubic BN films and single crystal diamond films by CVD and PVD. To obtain our objectives first, we are developing CVD, PVD, and other methods to synthesize the films. Secondly, we will investigate chemical, physical, and electrical properties of the films to understand the growth mechanisms of the synthesis and to optimize the processes. In this paper, results on the recent advances on cubic BN and diamond research at NIRIM are briefly discussed.

1. Introduction

Diamond with outstanding physico-chemical properties can be considered as one of the most important materials for applications such as mechanical, optical, thermal, and electronic devices. Among them, the most attractive application of diamond would be a semiconductor for high temperature and high power electronic devices originated from the very large band gaps of 5.5 eV. So diamond is considered to be a future semiconductor in place of silicon semiconductors, 'a basic material for today's microelectronics'. For this, however, we must overcome mainly two hurdles in the following.

One is the production of single crystal diamond films suitable for electronic devices such as diodes and transistors without grain boundaries. Lattice imperfections such as non-stoichiometry, lattice defects, and solute segregation-precipitation at grain boundaries make polycrystal diamond films unsuitable for semiconductors. So, single crystal diamond films is particularly requested. The other is the production of n-type semiconductor of diamond. A p-type semiconductor of diamond has been synthesized by using boron as a dopant, however the synthesis of a n-type semiconductor has not been reported. Nitrogen is adjacent to carbon in the periodic table and it is small enough to incorporate in the carbon site, however, extra electrons are strongly bound to nitrogen with 1.7 eV. So the electrons are difficult to move freely in a diamond crystal. So nitrogen is not suitable for a n-type dopant. The other dopants, however, are too large to incorporate in the diamond lattice.

On the other hand, cubic BN with similar physico-chemical properties to those of diamond and the very large band gaps of 6.4 eV can be made into both n- and p-type semiconductors when suitable impurities are used(1). However, reliably reproducible methods for growing cubic BN films have been not yet developed. So, basic research for growing cubic BN films with reliability should be carried out. Needless to say, one of the most important

objectives in this super diamond project is to develop various methods for growing both cubic BN films and single crystal diamond films.

2. Super diamond research at NIRIM
2. 1. Synthesis of Cubic BN

The synthesis of cubic BN films has been mainly carried out by PVD methods such as reactive sputtering(2-4), reactive pulse plasma(5), ion beam deposition(6-9), activated reactive evaporation(10), ion plating(11), and others(12-18). These processes have been carried out by a combination of an electron beam evaporator and a post ionization system. The resultant ionized species are accelerated with bias voltages of 50-3000V in the substrates(NaCl, MgO, Si, Glass, Si_3N_4, WC,---), on which the species deposit to form a film at the growth rate of about 0.5-3 nm/sec.

The films obtained have been characterized by SEM inspection, electron diffraction patterns, chemical analysis, and mainly IR absorption spectra. They have high internal-stress and consist of very small crystals of diameter about 10 nm. That is, grain boundaries per unit volume are very high. Low temperature phases of h-BN are present at grain boundaries. Since the low temperature phases at grain boundaries are easily attacked by atmospheric moisture when they are exposed to air(19), they tend easily to peel off from a substrate. Therefore, the synthesis of cubic BN films without low temperature phases is strongly required. One of another problems is that IR absorption peaks used for detecting the cubic BN films obtained from PVD are very diverse from 1020 to 1200 cm^{-1}. Perhaps this may be related to impurities and nonstoichiometry in the composition. The synthetic methods for growing cubic BN films to be able to control the impurity levels and stoichiometry of the films are required.

Recently Komatsu et al at NIRIM(20) found that the growth reaction of boron from B_2H_6 in plasma CVD, such that $BH^*_2 = B(s) + H_2$, where BH^*_2 is a BH_2 chemisorbed to a site for growth and B(s) is a boron atom incorporated into the film structure, is enhanced or activated photochemically by simultaneous pulse laser irradiation on the film surface at 193 nm with a sufficiently weak laser-pulse energy of 170-200 $mJcm^{-2}$. They have also obtained a result indicating photo induced migration of BH_n(n = 1,2,3) in the above system (21). They accordingly employed the laser assisted plasma CVD method to the synthesis of cBN films in which, they thought, the growth reactions and the migration of the precursor radicals can be enhanced photochemically in order to improve the crystallinity. That is, in an inductively-coupled plasma in $BCl_3 + NH_3 + H_2 + Ar$ at 2.8 torr and substrate temperature of 500-900°C, they (22) irradiated the growing film surface with an ArF excimer laser operated at 25 Hz with 10 ns pulses in order to activate the surface processes favorable for the growth of cubic BN. The energy density at the substrate position was 18-24 $mJcm^{-2}$ per pulse, under which the heating effect of the irradiation on the surface was estimated to be negligible. The substrate was a silicon wafer with (100) plane. The substrate temperature was kept constant

independent of the plasma and laser conditions by using a PID controller. Fig. 1 shows a typical SEM micrograph of a sample prepared at 500°C and 3kW; by virtue of laser irradiation, the nucleation of the crystal grains has been initiated that they form a "stone circle". It appears here that the (100) plane of the cubic phase is developed in parallel with the substrate. Isolated grains with similar morphology were also found at 600°C and 3kW. No similar crystal grains have been found in the samples prepared under the corresponding conditions without the irradiation; this indicated the critical role of the laser irradiation in the formation of these cubic BN grains. They reported that the observed lattice parameters are in quite good agreement with those of cubic BN and they concluded that the observed IR absorption at $1105cm^{-1}$ and probably also that at $1561cm^{-1}$ corresponded to the cubic phase contained in their sample.

The formation of a p-n junction diode of cubic BN was reported by Mishima et al(23-24) at NIRIM. They firstly made a p-n junction diode of cubic BN by growing a Si doped n-type crystal epitaxially on a Be doped p-type seed crystal at a pressure of 55 kilobars and a temperature of about 1700°C by using a temperature-difference solvent method. The junction obtained was clearly confirmed at 1 bar by rectification characteristics and by existence of a space charge layer at the junction as observed by electron beam induced current measurement. Fig. 2 shows typical results of the electric measurement up to 650°C. As can be seen in the figure, the same rectification characteristics were always observed when the current passed through the junction. The reproducible rectification characteristics of the diode were observed up to a temperature of 650°C. Luminescence ranging mainly from an ultraviolet of -215nm to a blue region was clearly observed at the n-type side along the p-n junction only when a forward current passed through the junction.

It is well known that plasma generating devices play very important role in many processings of vapor deposition. Fortunately we have so far developed various kinds of plasma generators for a cold plasma and a thermal plasma in power levels from a few kW to 100 kW with variable frequencies. Among them, one of the most interesting plasma generators is a center-injection RF plasma-torch. It is very useful to produce a materials with high purity and a very high temperature plasma, in which we can introduce reactant materials for evaporation and ionization in order to make chemical species with high energy for the deposition of films. Also a reciprocal-type plasma torch developed is very stable and useful for growing cubic BN films in combination with a excimer laser.

Based upon the above research, we intend to synthesize cubic BN films with high quality mainly by the following methods,
(1) Plasma CVD, laser-enhanced CVD, and a combination of laser and plasma CVD.
(2) PVD such as sputtering and ion beams, a combination of PVD and CVD.

(3) Molecular beams and chemical beams in high vacuum.
(4) Other methods.
The fundamental concept in this research is that we plan to activate the surface processes favorable for the growth reaction of cubic BN films by the above methods . Actually we will investigate and optimize the experimental conditions such as reaction gases, plasma power, laser power, laser wave length, and others favorable for the growth reaction of cubic BN films. Also studies on the growth mechanisms of cubic BN films are being carried out to obtain appropriate information for growing the films with high quality.

2. 2. Synthesis of single crystal diamond films
The synthesis of diamond at lower pressure than 1 atm was firstly considered by Eversole[25] in USA, Angus et al[26] in USA, and Derjaguin et al[27-28] in CSI. However, the growth rate is very low, angstroms per hour, and the simultaneous codeposition of graphite was always a problem. In the early 1980s, the synthesis of diamond by CVD methods was dramatically developed by a research group in NIRIM, that is, Matsumoto et al[29-30] reported so called hot-filament method on the synthesis of diamond particles from the mixture of CH_4 and H_2, Kamo et al[31] reported a microwave plasma method to activate CH_4 and H_2 to grow crystalline diamonds, and also Matsumoto et al[32-33] developed radio-frequency glow and arc plasma methods on diamond growth. In this way, our Institute has achieved remarkable results in diamond research.

As mentioned before, one of the most important problems in the application of diamond films to electronic devices is to produce single crystal diamond films with high quality.   One method to make single crystal diamond films uses a single crystal substrate of a material whose crystal structure and lattice spacing are approximately equal to those of diamond. Matsumoto et al[34] firstly grow epitaxial diamond films to several micron on a natural diamond substrate. They found that the films were nearly transparent in visible and IR regions and the absorbtion edge was about 225nm(5.5eV). They also found cracks along <110> due to the presence of internal stress, when the films grew thick.   Kamo et al[35-36] later carried out epitaxial growth of diamond films on (111), (110), and (100) planes of natural diamonds by using a microwave plasma method. They deposited epitaxial films on the (111) and (110) planes at 820-950°C, and on the (100) plane at 820°C. They indicated that the hydrogen concentration of the epitaxial films is estimated to be similar to that in a natural diamond and that the contamination from a substrate holder used can not be neglected.   Just recently Aizawa and coworkers[37] studied (111) and (100) diamond surfaces grown epitaxically on natural diamond substrates by high resolution electron energy loss spectroscopy. As a result, they found that only one sp^3 hybridized bonding existed on both surfaces and hydrogen terminated (111) surface as CH_3 and (100) surface as CH. They also obtained two types of C-H stretching modes on (111) surface corresponding to symmetric and asymmetric vibrations and only one C-H stretching mode on (100) surface.

A research group in U. S. A. has tried to develop an alternative technique to be able to grow single crystal diamond films(38). They employed an array of small seed crystals of diamonds in pyramid pits etched into a Si wafer, in which all the crystals have the same crystallographic orientation each other. Diamond deposited on top of the seeds with the orientation to form a single crystal diamond film. However, we do not know whether the film is a single crystal or not.

Single crystal diamonds prepared by a conventional high pressure growth method have always rough surfaces due to the presence of dendritic patterns, which are considered to result in the precipitation of carbons from a metal solvent during cooling. Recently Kanda and Ohsawa(39) developed a new solvent of Ni-5%Si for a high pressure diamond-growth. By using it, they successfully synthesized single crystal diamonds with the mirror surfaces of {111} and {100} planes. The single crystals obtained may be particularly useful as substrates both for the heteroepitaxial growth of cubic BN films and for homoepitaxial growth of diamond films. They are also useful as heat sinks for electronic devices.

Recently, many workers have tried to deposit heteroepitaxial diamond films on various substrates. For instance, Koizumi et al(40) grew heteroepitaxially diamond films on cubic BN{111} and indicated the epitaxial relation of the films as {111}diamond // {111}cubic BN by an electron diffraction. They suggested from the Raman peak shift toward lower wave number in the diamond film deposited that the tensile stress involved in the film was present. Sato et al(41-42) deposited diamonds on nickel substrates from CH_4-H_2 mixtures in a microwave plasma reactor. Resultantly they found epitaxial relationship between a diamond and the substrate when diamonds grew both on (111) and (100) planes of nickel at CH_4 concentrations lower than 0.9% at a substrate temperature from 700- 1000°C. Also the possibility has been shown that the coalescence of diamond crystals deposited can take place to form a single crystal film. However, they found at CH_4 concentration higher than 1.0 % that the substrate was covered with disordered graphite. Stoner and Glass(43) tried to deposit diamond films on a ß-SiC substrate by a bias pretreatment followed by standard microwave plasma CVD. As a result, they could successfully grow epitaxial diamond particles on (001) ß-SiC, and they suggested that the diamond nucleation was enhanced by biasing the substrate. Wolter et al(44) deposited ordered diamond films ({100}diamond // {100}Si and <110> diamond // <110> Si) on single crystal Si substrates via an in situ carbonization followed by bias-enhanced nucleation in microwave plasma reactor. It is speculated that the in situ carbonization forms an epitaxial SiC conversion layer on which diamond films deposits epitaxially. On the other hand, Jiang et al (45) carried out the growth of epitaxial (001) diamond film on mirror-polished single-crystal (001) Si substrates by using microwave plasma CVD from a CH_4-H_2 gas mixture. As a result, they suggested that no interfacial layer for mismatch compensation was formed within the detection limits of X-ray and Raman analysis. Argoitia et al(46)

deposited diamond films on the basal plane of BeO with the epitaxial relationship {111}diamond // {0001}BeO and <110>diamond rotated by less than °6 with respect to <1120>BeO. They grew also diamond on (1120) prism plane of BeO and observed small particles of beryllium carbide(Be_2C) during diamond deposition on (1120)BeO plane.

Based upon the above research results, the following studies are mainly being planned.

1) We will attempt to develop CVD and PVD methods of producing single crystal diamond films by using various substrate such as Ni, Co, Cu, Si, SiC, diamond and others.

2) We will attempt to produce various substrates for homo- and heteroepitaxy by high-pressure processes and conventional processes.

3) We will attempt to produce diamond semiconductors by doping impurities during the CVD and PVD processes.

4) We will attempt to study physico-chemical properties of diamond films. In summary in a word, we will carry out systematically in the following three developments.

(1) Synthesis of cubic BN films
(2) Synthesis of single crystal diamond films
(3) Characterization of physico-chemical properties in the films
The outline of the research is briefly listed in Table 1.

References
1) R. H. Wentorf, Jr., J. Chem. Phys., **36**,1990(1962).
2) B. N. Gaschtold, Electr. Technol., USSR, **12** ,58(1970).
3) N. Ohmae, J. Vac. Sci. Technol., **13**, 82(1976).
4) M. Mieno and T. Yoshida, Japan J. Appl. Phys. ,**29**,   L1175(1990).
5) M. Sokolowski, J. Cryst. Growth, **46**, 136(1980).
6) C. Weissmantel et al, Thin Solid Films, **72**, 19(1980).
7) C. Weissmantel, J. Vac. Sci. Technol., **18**, 179(1981).
8) S. Shanfield and R. Wolfson, ibid., A1, 323(1983).
9) M. Satou and F. Fujimoto, Japan J. Appl. Phys., **22**, L171(1983).
10) K. L. Chopra et al, Thin Solid Films, **126**, 307(1985).
11) M. Murakawa et at, Surface and Coating Technology, 1, 55(1990).
12) K. Inagawa, K. Watanabe, H. Ohsone, K. Saitoh, and A. Itoh, J. Vac. Sci. Technol., **A5**, 2696(1987).
13) G. Kessler, H-D. Bauer, W. Pompe, and H-J. Scheibe, Thin Solid Films, **147**, L45(1987).
14) S. Mineta, M. Kohata, N. Yasunaga, and Y. Kikuta, ibid., **189**, 125(1990).
15) Y. Ichinose, H. Saitoh, and Y. Hirotsu, Surf. Coating Technol., **43/44**, 116(1990).
16) G. L. Doll, J. A. Sell, C. A. Taylor, and R. Clarke, Phys. Rev., **B43**, 6816(1991).
17) Y. Osaka et al, Materials Science Forum, **54/55**, 277(1990).
18) Y. Osaka et al, Mat. Res. Soc. Symp. Proc., **223**, 81(1991).
19) M. J. Rand and J. F. Roberts, J. Electrochem. Soc., **115**, 423(1968).

20) S. Komatsu, M. Kasamatsu, K. Yamada, and Y. Moriyoshi, Appl. Phys. Lett., 64, 1879(1988).

21) S. Komatsu, Y. Moriyoshi, K. Kasamatsu, and K. Yamada, J. Phys. D: Appl. Phys., 24, 1687(1991).

22) S. Komatsu, Y. Moriyoshi, K. Kasamatsu, and K. Yamada, J. Appl. Phys., 70, 7078(1991).

23) O. Mishima, J. Tanaka, S. Yamaoka, and O. Fukunaga, Science, 238, 181(1987).

24) O. Mishima, K. Era, J. Tanaka, and S. Yamaoka, Appl. Phys. Lett., 53, 962(1988).

25) W. G. Eversole, "Synthesis of Diamond" U.S. Pat. No.3030188 Apr. 17, (1962).

26) J. C. Angus, H. A. Will, and W. S. Stanko, J. Appl. Phys., 44, 1423(1968).

27) B. V. Derjaguin, D. V. Fedoseev, and K. S. Uspenckaya, Zh. Fiz. Khim., 47, 24(1973).

28) B. V. Spitsyn, L. L. Builov, and B. V. Derjaguin, J. Cryst. Growth, 52, 219(1981).

29) S. Matsumoto, Y. Sato, M. Tsutsumi, and N. Setaka, J. Mater. Sci., 17, 3106(1982).

30) S. Matsumoto, Y. Sato, M. Kamo, and N. Setaka, Japan J. Appl. Phys., 21, L183(1982).

31) M. Kamo, Y. Sato, S. Matsumoto, and N. Setaka, J. Cryst. Growth, 62, 642(1983).

32) S. Matsumoto, J. Mater. Sci. Lett., 4, 600(1985).

33) S. Matsumoto, T. Kobayashi, M. Hino, T. Ishigaki, and Y. Moriyoshi, Proc. of the 8th Inter. Symp. Plasma Chem. Ed. K. Akashi and A. Kinbara, Vol4, P.2458(1987).

34) S. Matsumoto, Y. Sato, M. Kamo, J. Tanaka, and N. Setaka, Proc. 7th Inter. Conf. Vacuum Metallurgy, Ed. M. Inoue, p.386(1982), Tokyo.

35) M. Kamo, H. Yurimoto, and Y. Sato, Appl. Surf. Sci., 33/34, 553(1988)

36) M. Kamo and Y. Sato, Prog. Crystal Growth and Charact., 23, 1(1991).

37) T. Aiawa, T. Ando, M. Kamo, and Y. Sato, Phys. Review B, 48, 18348(1993).

38) M. W. Geis and J. C. Angus, Scientific American, October, 64(1992).

39) S. Kanda and T. Ohsawa, The Review of High Pressure Science and Technology, 2, 192(1993) in Japanese.

40) S. Koizumi, T. Murakami, T. Inuzuka, and K. Suzuki, Appl. Phys. Lett., 57, 563(1990).

41) Y. Sato, H. Fujita, T. Ando, and M. Kamo, Epitaxial growth of diamond from the gas phase. In Proc. 2nd Int. Conf. New Diamond Science and Technology, Ed. R. Messier, J. T. Glass, J. E. Butler, R. Roy, p. 371(1991), Pittsburgh: Materials Research Society.

42) Y. Sato, H. Fujita, T. Ando, T. Tanaka, and M. Kamo, Phil. Trans. R. Soc. Lond. A 342, 225(1993).

43) B. R. Stoner and J. T. Glass, Appl. Phys. Lett., 60, 698(1992).

44) S. D. Wolter, B. R. Stoner, J. T. Glass, P. J. Ellis, D. S. Buhaenko, C. E. Jenkins, and P. Southworth, ibid., 62, 1215(1993).

45) X. Jiang , C. P. Klages, R. Zachai, M. Hartweg, and H. J. Fusser, ibid., **62**, 3438(1993).
46) A. Argoitia, J. C. Angus, L.Wang, X. I. Ning, and P. Pirouz, J. Appl. Phys., **73**, 4305(1993).

Table 1 Super Diamond Research

	1993	1994	1995	1996	1997
1. Synthesis Technology of Cubic BN films					
(1) Synthesis of cubic BN through the control of the structure at atomic level	Synthesis of cubic BN films by surface activated methods		Synthesis of cubic BN films through the control of the structure at atomic level	Study synthesis of semiconductors	
(2) Synthesis of substrates	Synthesis of high-quality substrates		Synthesis of large-area substrates		
2. Synthesis Technology of Single Crystal Diamond films					
(1) Epitaxial growth of singl crystal diamond films		Epitaxial growth of single crystal diamond films		Study synthesis of semiconductors	
(2) Control impurities		Epitaxial growth of single crystal diamond films through the control of impurities		Study synthesis of optoelectronic materials	
3. Property Analysis					
(1) Characterization of defects and structural properties		Analysis of structural, chemical, electrical defects, and other properties			
(2) Characterization of electrical and optical properties		Analysis of electrical, optical, and other properties			

Nucleation and Growth of Diamond: Factors Influencing Quality and Growth Rates

J.C. Angus, A. Argoitia, L. Wang, C.S. Kovach, U. Landau, W.R.L. Lambrecht, P. Pirouz,
B. Segall and C. Lee

Case Western Reserve University, Cleveland, OH 44106, U.S.A.

1 Introduction

Much attention has been paid to the mechanisms of atom attachment during the growth of diamond by chemical vapor deposition. This work is the subject of two excellent recent reviews [1,2]. Detailed knowledge of mechanisms will likely be necessary for understanding the relationship between diamond growth rate and quality; however, at the present time the experimental support for any mechanism is limited and somewhat ambiguous. Even less consideration has been given to the mechanisms for the *de novo* nucleation of diamond from the gas phase [3-5]. Control of secondary nucleation and morphological stability are both essential for achieving growth of large diamond single crystals. In this paper we discuss these issues.

2 Nucleation of Diamond

2.1 *de novo* Nucleation of Diamond

There is experimental evidence from several sources that sp^2 or graphitic material is formed before diamond nucleation occurs [3, 6-8]. Also, diamond grows epitaxially on graphite [9] with the orientation: diamond(111) // graphite(0001) and diamond[110] // graphite[1120]. This epitaxial relationship corresponds to a continuation of the flat hexagonal network of the graphite (0001) planes into the buckled hexagonal network of the diamond (111) planes. The C-C bond length in graphite (0.142 nm) is only 2% smaller than the projected C-C bond length onto the diamond (111) planes (0.145 nm). Also, the ratio of the density of diamond (3.515 g cm^{-3}) to the density of graphite (2.26 g cm^{-3}) is very close to 3/2. Therefore, the simplest interface with low strain energy will have three diamond (111) bi-layers joined to two graphite (0001) layers [4,5]. See Fig. 1.

Based on these arguments we have suggested that diamond nucleation is initiated by the condensation of graphite (or graphitic structures) [3-5]. Once graphite has formed from the gas phase, its prism edges are hydrogenated by the atomic hydrogen. These hydrogenated prism faces present a surface that is geometrically and energetically favorable for diamond growth.

Figure 1. Model of one realization of a diamond/graphite interface with the orientation: diamond (111) // graphite (0001) and diamond [110] // graphite [1120]. From reference [5].
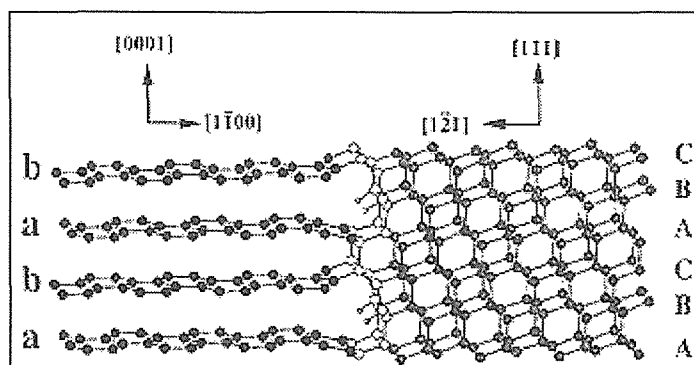
We have presented calculations that support this mechanism [5]. Variable metric static energy minimization calculations were made using the Tersoff semi-empirical many-body potential. The calculations were made for three-dimensional slab models with two-dimensional periodicity.

The calculated interfacial energies ($\sim$1.7 J m^{-2}) are significantly lower than the corresponding free surface energies ($\sim$6 J m^{-2}). This implies that the adhesion energies between diamond and graphite with this interface are large.

The mechanism described above for diamond nucleation does not preclude other mechanisms, for example, on pre-existing diamond seed particles or on closely related structures such as c-BN or SiC.

2.2 Heteroepitaxial Nucleation of Diamond on Foreign Substrates

Cubic boron nitride (c-BN) is the most obvious substrate for diamond heteroepitaxy. Diamond and c-BN are both tetrahedrally bonded cubic solids and the lattice mismatch is only 1.4%. However, large single crystals of c-BN are not available. Beryllium oxide (BeO) has the wurtzite structure; its nearest neighbor configuration is tetrahedral, the same as in diamond. The bond length mismatch between diamond and BeO is 7%, which is the next smallest among the tetrahedrally bonded solids. Single crystals of BeO can be grown. First principles calculations of the bonding at the diamond/c-BN, diamond/BeO, and diamond/Cu interfaces suggest that the former two should be superior substrates for diamond heteroepitaxy [10]. Experimental progress towards heteroepitaxy on BeO [11] and demonstration of heteroepitaxy of diamond on c-BN have been reported [12-17]. Heteroepitaxy of diamond is favored on the cationic surfaces of c-BN and BeO, i.e., on the boron and beryllium terminated faces.

Evidence that diamond nucleates coherently on c-BN is obtained from high resolution and scanning electron microscopy [17]. See Figs. 2 and 3.

Figure 2. High resolution transmission electron micrograph of diamond grown on the boron terminated (111) face of cubic boron nitride by hot-filament assisted CVD [17]. An edge dislocation is within the indicated area.
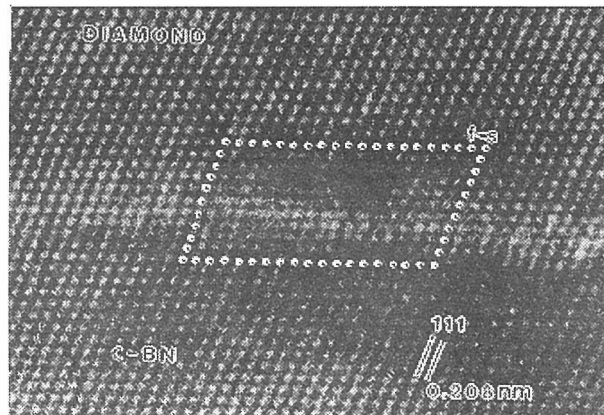
2.3 Influence of Stacking Faults and Twins on Nucleation and Growth

The intersection of twins with the surface of a diamond-cubic crystal gives re-entrant corners that provide favorable sites for atom attachment. Figure 4 shows diamond crystals in the early stages of growth by microwave assisted chemical vapor deposition [18]. The small hexagonally shaped crystals arise from a singly twinned nucleus. The re-entrant corner along the periphery of the crystal is visible in the right hand figure. Subsequent twinning on other {111} planes gives rise to a more complex, three-dimensional morphology. This is clearly shown in the larger crystals in Fig. 4, which exhibit twinning and re-entrant surfaces.

The original twinned nucleus may arise from a graphite precursor. It was shown by Lambrecht *et al.* [5] that a stacking error in a graphite precursor will lead to a stacking fault in the diamond that is nucleated on it. The diamond nucleus with the stacking fault will grow faster than an un-twinned diamond and should therefore be a particularly efficent starting point for diamond growth.
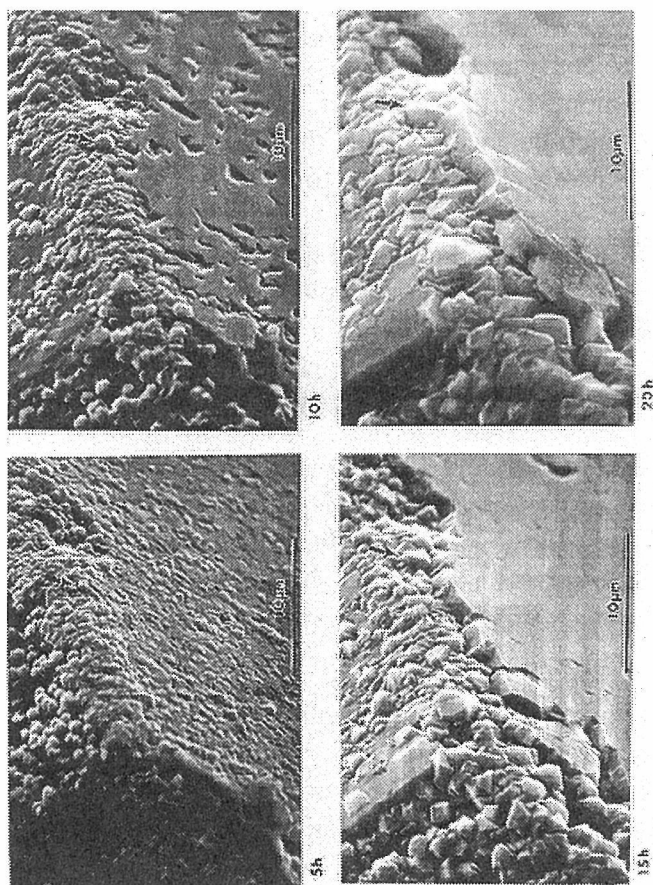
Figure 3. Progressive growth of diamond on a boron terminated (111) face of cubic boron nitride.

Scanning electron micrographs taken of the same point on the surface at 5, 10, 15 and 20 hours. Note that the figure is rotated 90°. The arrow indicates the same position on the surface. The growth appears to start by the formation of isolated three-dimensional nuclei that grow together to form a continuous, smooth single crystal diamond film. The linear dimensions of the single crystal film were approximately 400 x 400 microns.

Figure 4. Hexagonal diamond platelets formed during the early stages of microwave assisted diamond growth [18]. Scanning electon micrographs by S. Sahaida. G indicates re-entrant grooves.
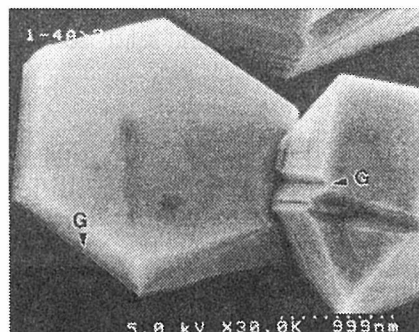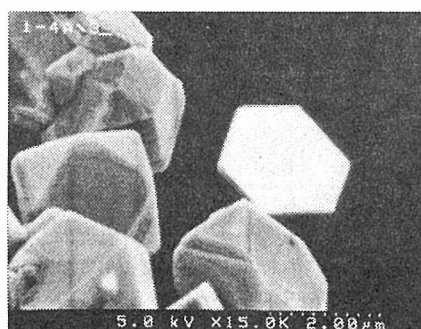
3 Mechanisms of Diamond Growth
3.1 Attachment Kinetics

Detailed models for the attachment of carbon atoms to a growing diamond surface have been presented by many authors and are reviewed elsewhere [1, 2]. We note here only that experimental support for any detailed mechanism is rather limited.

Most kinetic models of diamond growth assume that the surface is tetrahedrally coordinated and stabilized by chemisorbed hydrogen. However, Fallon and Brown have recently presented evidence that amorphous, dominantly sp^2, surface layers may be present during growth [19]. This observation is consistent with the results of Zhu *et al.* who found graphitic material in the grain boundaries of diamond grown by microwave assisted plasma CVD [20]. Also, there is a recent report of sp^2 material at the interface between diamond and a silicon substrate [21]. These observations are also consistent with other indirect evidence, e.g., the presence of conducting layers on the surface of diamond after growth.

If sp^2 layers are indeed present on the surface of diamond during growth, then alternative mechanisms for carbon attachment kinetics must be considered. One possibility is the continuous transformation of an sp^2 conversion layer into diamond by the action of atomic hydrogen. This model is consistent with the observation from microbalance studies that site limited surface processes may play a role in diamond growth [8]. It also is closely related to the recent proposals for the mechanism of diamond nucleation [4, 5].

Reduced reaction sets may be used to describe the overall diamond growth mechanism in the absence of detailed knowledge of mechanisms [8, 22]. One can use a simple reduced reaction set to describe possible growth mechanisms for diamond through conversion of a surface layer. Assume, for example, that the active growth species is C_xH_y. It can add to a surface site, S, to form an adsorbed intermediate, X, which in turn can react with atomic hydrogen to form diamond, D, or with more C_xH_y to form non-diamond carbon, Y.

$$C_xH_y + S \rightarrow X$$
$$C_xH_y + X \rightarrow Y$$
$$X + H \rightarrow D + S$$
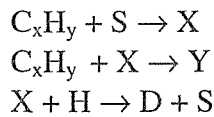
The above reaction set is closely related to the set proposed by Wang and Angus [8] to rationalize their microbalance results and by Goodwin [22] to relate defect concentrations to growth rates. Simple kinetic expressions can be derived from these reduced mechanisms by using the steady state approximation together with assumptions about the nature of the growth process. For example, if the concentrations of surface sites, [S], and adsorbed species, [X], obey the relation

$$[S] + [X] = 1,$$

one obtains Langmuir-Hinshelwood type rate expressions characteristic of site-limited growth. Much more detailed study of the diamond surface during growth will be necessary before any conclusions about growth mechanisms can be made; however, simple mechanisms such as the one illustrated here can lead to rate expressions that agree in broad outline with the available observations.

3.2 Morphological Instabilities

Morphological instabilities arise when local perturbations of the growth surface are amplified rather than damped out. The simplest example with relevance for diamond chemical vapor deposition occurs when the growth rate is limited, at least in part, by mass transport of species to the surface. When a portion of the crystal protrudes into the gas phase, the flux at this site will increase, leading to increased local growth rate. The enhanced growth rate leads to still further extension of the protrusion. Detailed treatments of this effect are given by Palmer and Gordon [23] and Sekerka [24]. Processes acting to damp out perturbations include surface diffusion and re-vaporization of the perturbation. Because of the very strong bonding in diamond, both of these processes are likely to be slow. Therefore, diamond may be particularly susceptible to instabilities.

The Thiele modulus, $m_T = kL/D$, provides a simple, heuristic criterion for growth uniformity. Here, k is a first order rate constant for surface attachment of carbon atoms, L is a characteristic length, and D is the diffusion coefficient of the growth species in the gas phase. Uniform growth is expected when $m_T = kL/D \ll 1$.

Ravi [25] and Kovach et al. [26] have reported experimental evidence of morphological instabilities during combustion growth of diamond. Kovach et al. also reported numerical simulations which supported the conclusion that morphological instabilities were present [26]. Figure 5 shows a striking example of the development of morphological instabilities along the edge of a diamond window on which new diamond has been grown by the combustion method.
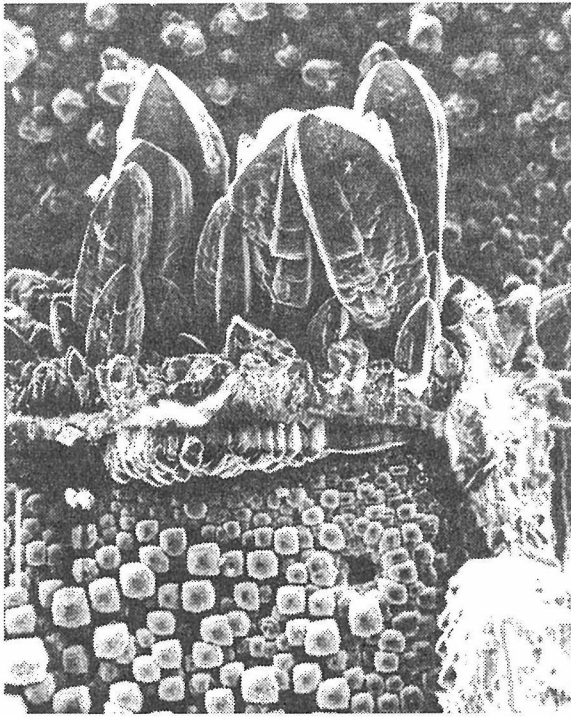
Figure 5. Example of morphological instability during the combustion growth of diamond [26]. Diamond was grown on a 1x1x0.25 mm (100) diamond window. The vertical white mark on the left hand side is 100 microns. The blade shaped crystals at the upper part of the microphotograph formed at the leading edge of the substrate. These crystals grew into the direction of the incoming gas stream. As they grow they receive additional flux and eventually the growth surface moves out of the zone in the flame where diamond is formed. Compare these crystals to the highly oriented crystals visible in the lower part of the Figure that grew on the flat (100) surface of the substrate.

We have performed further simulations of both the torch and hot-filament growth environments. The simulations, shown in Fig. 6, were performed using a modified finite difference method capable of simulating curved and moving boundaries [27]. The growth surface was constantly updated during the simulation. Parameters believed to be typical for combustion growth

a) ten time increments of Δt = 1 min; m_T = 0.5

d) nine time increments of Δt = 0.033 min; m_T = 10

b) ten time increments of Δt = 1 min; m_T = 0.05

e) nine time increments of Δt = 0.05 min; m_T = 1

c) ten time increments of Δt = 6 min; m_T = 0.0005

f) nine time increments of Δt = 0.1 min; m_T = 0.1
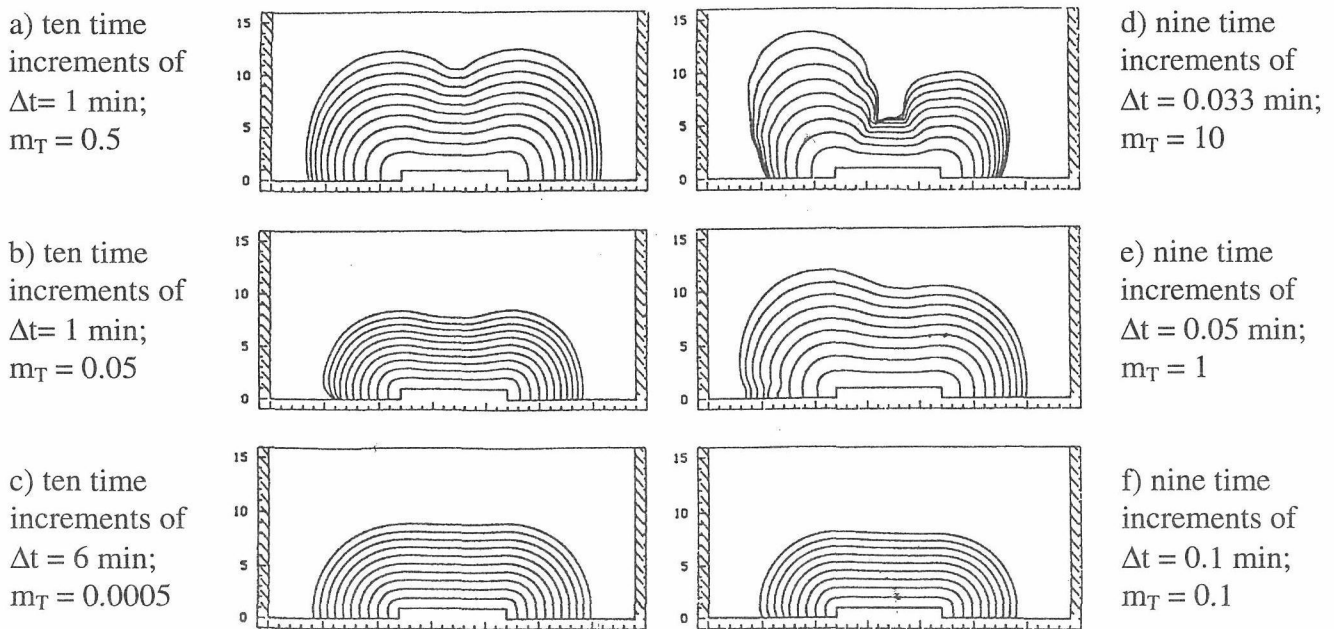
Figure 6. Simulated surface profiles of growing diamond. The lines show the profile at consecutive time intervals, Δt. Figs. 6a, b and c show surface evolution during simulated hot-filament growth; Figs. 6d, e and f show surface evolution during simulated combustion synthesis. Each grid spacing corresponds to 0.1 micron; each starting substrate was 1 micron wide and 0.1 microns high. In Figs. 6d, e and f the combustion gases were incident on the substrate downward from the left at 45°.

and hot-filament assisted deposition were used. The parameters for the simulation were chosen by using pressures of 20 torr and 1 atm respectively for the hot-filament and combustion reactors. Gas phase concentrations of active species far from the substrate were estimated from literature sources. The value of the surface rate constant, k, was varied to provide a range of growth rates corresponding to experiments. The average simulated growth rates can be estimated from the Figures. For example, in Fig. 6c the surface has grown approximately 0.8 microns (8 grid spaces) during ten time increments of 6 minutes each for an average linear growth rate of 0.8 microns per hour. In Fig. 6e the surface grew approximately 1 micron (10 grid spaces) during 9 time increments of 0.05 minutes each for an average growth rate of 133 microns per hour.

Compare Figs. 6d and 6e with Fig. 5. Note that the uniformity decreases as the growth rate and the value of the Thiele modulus, m_T, increase. (In estimating the magnitude of the Thiele modulus a characteristic length, L, of 1 micron, the width of the substrate, was assumed.)

4 Acknowledgements

5 References

[1] F.G. Celii and J.E. Butler, *Ann. Rev. Phys. Chem.* **42**, 643 (1991)

[2] J.E. Butler, *Phil. Trans.Roy. Soc. A* **342**, 209 (1993);

[3] J.C. Angus, A. Argoitia, R. Gat, Z. Li, M. Sunkara, L. Wang and Y. Wang, *Phil. Trans. Roy. Soc. A* **342**, 195 (1993)

[4] J.C. Angus, Z. Li, M. Sunkara, C. Lee, W.R.L. Lambrecht and B. Segall, Proceedings 3rd Symposium on Diamond Materials, Honolulu, May, 1993; p. 128, Proceedings Volume 93-17, p. 128, Electrochemical Society, Pennington, NJ, 1993

[5] W.R.L. Lambrecht, C.H. Lee, B. Segall, J.C. Angus, Z. Li and M. Sunkara, *Nature* **364**, 607 (1993)

[6] D.N. Belton and S.J. Schmieg, *Surface Science* **233**, 131 (1990)

[7] M.M. Waite and S.I. Shah, *Appl. Phys. Lett.* **60**, 2344 (1992)

[8] Y. Wang and J.C. Angus, Proceedings 3rd Symposium on Diamond Materials, Honolulu, May, 1993; p. 249, Proceedings Volume 93-17, Electrochemical Society, Pennington, NJ, 1993

[9] Z. Li, L. Wang, T. Suzuki, A. Argoitia, P. Pirouz and J.C. Angus, *J. Appl. Phys.* **73**, 711 (1993)

[10] W.R.L. Lambrecht and B. Segall, "Bonding of Diamond to Semiconductors and Metals," Electrochem. Symp. Series, "Diamond Materials," Electrochemical Society, Pennington, NJ, 1991

[11] A. Argoitia, J.C. Angus, L. Wang, X. Ning and P. Pirouz, *J. Appl. Phys.* **73**, 4305 (1993)

[12] R. Haubner, *Refrac. Metals and Hard Mater.* **38**, 1316 (1990)

[13] S. Koizumi, T. Murakami, T. Inuzuka and K. Suzuki, *Appl. Phys. Lett.* **57**, 563 (1990)

[14] M. Yoshikawa, H. Ishida, A. Ishitani, T. Murakami, S. Koizumi and T. Inuzuka, *Appl. Phys. Lett.* **57**, 428 (1990)

[15] M. Yoshikawa, H. Ishida, A. Ishitani, S. Koizumi and T. Inuzuka, *Appl. Phys. Lett.* **58**, 1387 (1991)

[16] T. Inuzuka, S. Koizumi and K. Suzuki, *Diamond and Related Materials* **1**, 175 (1992)

[17] L. Wang, P.Pirouz, A. Argoitia, J.S. Ma and J.C. Angus, *Appl. Phys. Lett.* **63**, 1336 (1993)

[18] J.C. Angus, M. Sunkara, S.R. Sahaida and J.T. Glass, *J. Mater. Res.* **7**, 3001 (1992)

[19] P.J. Fallon and L.M. Brown, *Diamond and Related Materials,* **2**, 1004 (1993)

[20] W. Zhu, C.A. Randall, A.R. Badzian and R. Messier, *J. Vac. Sci. Tech. A* **7**, 2315 (1989)

[21] D.A. Muller, Y. Tzou, R. Raj and J. Silcox, *Nature* **366**, 725 (1993)

[22] D.G. Goodwin, *J. Appl. Phys.* **74**, 6888 (1993)

[23] B.J. Palmer and R.G. Gordon, *Thin Solid Films* **158**, 313 (1988)

[24] R.F. Sekerka, *J. Cryst. Growth* **128**, 1 (1993)

[25] K. Ravi, *J. Mater. Res.* **7**, 384 (1992)

[26] C.S. Kovach, B. Roozbehani, T. Suzuki and J.C. Angus, Proc. 2nd Int. Conf. on the Applications of Diamond Films and Related Materials, M. Yoshikawa, M. Murakawa, Y. Tzeng and W.A. Yarbrough, Eds., MYU, Tokyo, 1993

[27] CELL DESIGN, L-Chem. Inc., PO Box 20003, Shaker Heights, OH, 44120, USA

General Approach to the Generation of Diamond Nuclei by the Bias-Pretreatment Method

S. Yugo

University of Electro-Communications, 1-5-1, Chofugaoka, Chofu-shi, Tokyo 182, Japan

Abstract

We have presented a nucleation model suggesting the mechanisms for the enhancement by energetic ions in plasma chemical vapor deposition. The application of a negative bias collects carbon ions at higher rates onto the silicon surface, and increases their bond strength with the surface owing to ion mixing.

This enhances the formation of carbon clusters overcoming re-evaporation and diffusion. The impinging energetic ions destroy the weak sp^2 structure and increases the sp^3 structure, leading to the formation of diamond nuclei precursors. The contribution of hydrogen to generation of diamond nuclei is large. Hydrogen ions inhibit the formation of sp^2 plane carbon bonds and enhance the formation of sp^3 tetrahedral bonds.

Introduction

Chemical vapor deposition (CVD) of diamond is carried out in a hydrogen plasma, which makes difficult the nuclei generation on a mirror-polished silicon surface because of strong etching of carbon atoms by the hydrogen plasma. (a) Formation of nucleation sites, (b) increase in the carbon content in the hydrogen plasma ,(c) reinforcement of the bonds between nuclei and a substrate may enhance the nuclei generation. As for (a), we have shown that the scratching of the substrate surface with the powder by ultrasonic vibration was very effective[1,2]. This method, however, seems to make randomly oriented nucleation sites, which would make the growth of highly oriented diamond crystallites or the epitaxial growth of diamond films very difficult.

Recently we have proposed a new method dealing with the items (b) and (c)[3,4]. It is a pretreatment process of the substrate surface in a microwave hydrogen plasma with a high methane content and the application of negative dc bias on the substrate surface. For instance, a 5 minutes pretreatment of a silicon surface in 40%CH_4/H_2 microwave plasma at a substrate bias of -100V, and the following diamond growth under a normal growth condition (lower methane content and without bias) resulted in the formation of the nucleation density as high as 10^{10}/cm^2.

This new method is expected, in addition to the formation of high density diamond nuclei, to open a path to a basic research on the epitaxial growth of diamond films in respect to the control of carbon supersaturation, the removal of amorphous carbon, the formation of nuclei precursors due to ion impinging, the reinforcement of bonds between nuclei and substrates, and the role of hydrogen plasma. This reports deals with a basic study on these problems.

Experimental procedure and results

Mirror polished silicon (100) of 1~5 Ω-cm and Mo meshes were used as substrate. The pretreatment process was a microwave plasma CVD in a hydrogen plasma with a methane content much larger than in the plasma for the normal CVD diamond growth and with the application of a negative DC bias. The shematic diagram and the process detail on pretreatment method are described elsewhere[3,4].

These results are shown in Figs.1~4.

Discussion

It has been reported that the application of positive bias during diamond CVD growth enhanced the generation of diamond nucleus owing to an electron shower effect [5] and that the application of a negative bias improved the crystal quality[6] and crystal orientation[7~9] owing to an ion shower effect. These bias effects will also affect the nucleus generation during the pretreatment process, owing to the activation of reactive species and the reaction enhancement between them.

Many reports on the formation of i-carbon and diamond like carbon[10~12] indicate that the impinging ion energy is in a narrow range from 50 to 200 eV. In addition, the effectiveness of hydrogen on the preferential formation of sp^3 bonds has also been recognized. These results agree very well with the present optimum pretreatment conditions. The agreement indicates that the mechanisms for the transformation from sp^2 to sp^3 structure and the formation of diamond nuclei are in principle identical in the growth of any kinds of diamond structures.

Effect of ion impinging on the nuclei generation

The energy of ions impinging on the substrate surface is a function of the ratio of the sheath width to the mean free path. The mean free path of ions is about 5 μm for the gas pressure of 2000 Pa used in the pretreatment, and it is nearly equal to the ion sheath width obtained from the dark space distance. Therefore, the energy of ions in electron Volts impinging on the substrate surface can be assumed to be nearly equal to the bias voltage. The number of displaced atoms due to impinging ions is given by the Kinchin-Peace equation[13] : $n = E_p/2E_d$ where E_p is the energy of ions and E_d is the threshold energy for displacement. Using the values of $E_d = 14eV$ for Si,

25eV for graphite and 80eV for diamond, the average number of atoms displaced by 100 eV impinging ion is 3.5 for Si, 2 for graphite and 0.5 for diamond, respectively. The value for graphite is about 4 times larger, and it is the main reason for preferential etching of graphite compared to diamond in the pretreatment process at a high methane content.

Carbon atoms landing on the substrate surface from the vapor phase tend to become clusters to develop diamond nuclei, but re-evaporation and diffusion retards the clustering process. The pretreatment process can overcome these difficulties. Carbon clusters may contain more sp^2 components than sp^3 components if no bias is applied. The application of negative d.c. bias of an optimum magnitude can only dissolve weakly bonded sp^2 carbon clusters by the collision of impinging ions, leaving more strongly bonded sp^3 structures[14,15]. In this way, clusters of sp^3 structure develop preferentially. These clusters are precursors for the diamond nuclei. At the same time, impinging ions effects an implantation of sp^3 clusters into the subsurface region of the substrate.

C ions of 100 eV penetrate into Si to a depth of approximately 0.6 nm with a deviation of approximately 0.3 nm. Although the implantation depth is shallow, ion mixing of C atoms with Si atoms can occur, and the bond strength between sp^3 clusters and Si substrates increases[16]. This may lead to the suppression of re-evaporation of sp^3 clusters and help the development of diamond nuclei.

Effect of hydrogen on nuclei generation

Enhancement of nuclei generation by the pretratment in CH_4/Ar was also observed, but at a much lesser density. This means that the chemical effect of hydrogen as well as the ion energy are very important. The chemical etching rate by hydrogen at around 600~800K is 1.5×10^{-1} for a-C:H, 1×10^{-1} for graphite and 5×10^{-2} for diamond which is about a half that of the former two. However, physical etching of graphite at around 700~1000K by energetic hydrogen ions produces 5×10^{-2} CH_4/H^+ for 50 eV H^+, 2×10^{-2} for 100 eV H^+[17]. These data indicate that the preferential removal of sp^2 component is greatly affected by the energy of the hydrogen ions as well as by their chemical etching effect.

Another important role of hydrogen is to terminate dangling bonds of carbon, prevents the formation of carbon sp^2 bonds. Muranaka et al.[18] reported that sp^2 component was easily prevented from C_1 and C_2 fragments, but the addition of hydrogen suppressed the formation of C_1 and C_2 fragments and increased sp^3 component. In the present pretreatment, it is speculated that hydrogen ions may terminate carbon dangling bonds when carbon clusters are decomposed by impinging ions, and that the formation of sp^2 bonds is prevented.

Nucleation Model

We explain the above results with a model. A high concentration of methane and the preferential etching of sp^2 components by hydrogen ions increase the degree of carbon supersaturation, which enhances the clustering of carbon atoms by overcoming reevaporation and diffusion. The ion impinging of carbon ions onto the substrate surface, on the other hand, causes mixing of carbon with substrate silicon and helps the formation of carbon clusters. Through the formed clusters are subjected to the ion impinging and decomposition, weakly bonded sp^2 structures are preferentially destroyed but strongly bonded sp^3 structures are increased by setting the ion energy at an optimum value, leading to the enhanced formation of nuclei precursors.

The role of hydrogen ions is to adjust the degree of carbon over saturation as well as to remove amorphous carbon. They also terminate C dangling bonds, suppress the formation of sp^2 bonds and support the formation of sp^3 bonds.

References

1 S. Yugo, T. Kimura and H. Kanai, Proc. 1st Int. Conf., New diamond Science and Technology, KTK, Scientific Publishers, Tokyo, 1990, p. 119.

2 S. Yugo, A. Izumi, T. Kanai, T. Muto and T. Kimura, Proc. 2nd Int. Conf., New diamond Science and Technology, Materials Research Society, Pittsburgh, 1991, p. 385

3 S. Yugo, T. Kanai, T. Kimura and T. Muto S. Yugo, Appl. Phys. Lett. 58, (1991) 1038.

4 S. Yugo, T. Kanai and T. Kimura, Diamond and Related Materials, 1, (1992) 388.

5 S. Yugo, T. Kimura and T. Muto, Vacuum, 41, (1990) 1364.

6 G-H. M. Ma, Y. H. Lee and J. T. Glass, J. Mater. Res., 5, (1990) 2367.

7 S. D. Wolter, B. R. Stoner and J. T. Glass, Appl. Phys. Lett., 62, (1993) 1215.

8 X. Jiang and C. P. Klages, Diamond and Related Mater., 2, (1993) 1112.

9 P. Koidl, C. Wild, R. Locher and R. Kohl, 2nd Int. Conf. Appl. Diamond Films and Related Materials, (MYU, Tokyo, 1993) 87.

10 S. Aisenberg and R. Chabot, J. Appl. Phys., 42, (1971) 2953.

11 S. R. Kasi, H. Kang and J. W. Rabalais, J. Vac. Sci. Technol., A6, (1988) 1788

12 P. Koidl, C. Wild, D. Dischler, J. Wagner and M. Ramsteiner, Materials Science Forum Vols. 52 and 53, Trans, Tech. Public, Switzerland, 1989, p41.

13 G. H. Kinchin and Peace, Report Prog. Phys., 18, (1955) 1.

14 W. Moller, Appl. Phys. Lett., 59, (1991) 2391.

15 Y. Lifshitz, S. R. Kasi and J. W. Rabalais, Phys. Rev. Lett., 62, (1989) 1290.

16 D. M. Mattox, J. Vac. Sci. Technol., A7, (1989) 1105.

17 W. L. Hsu, J. Vac. Sci. Technol., A6, (1988) 1803

18 Y. Muranaka, H. Yamashita, K. Sato and H. Miyadera, J. Appl. Phys., 67, (1990) 6247.
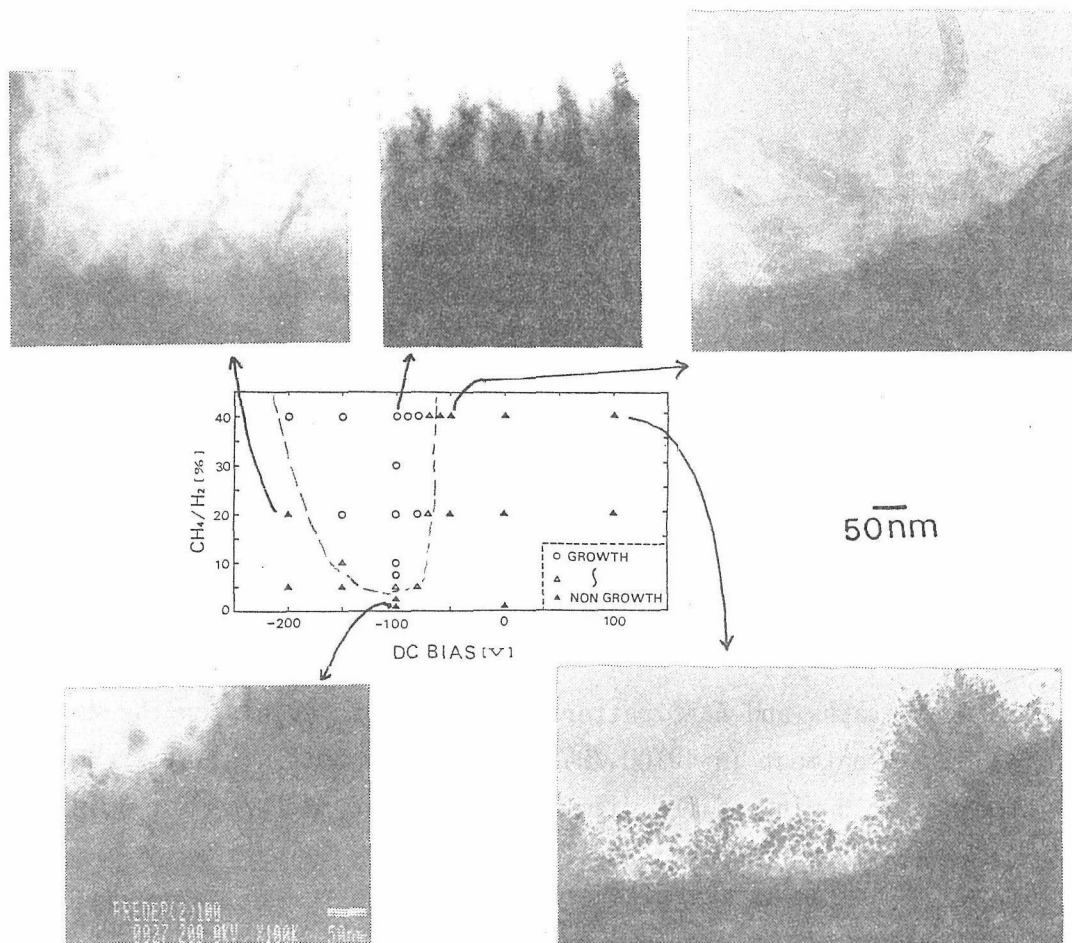
Fig.1 A figure showing a generation region of diamond nuclei as a function of DC
bias voltage and methane content, and TEM photographs of growth product on Mo
mesh by various bias-treatment condition.
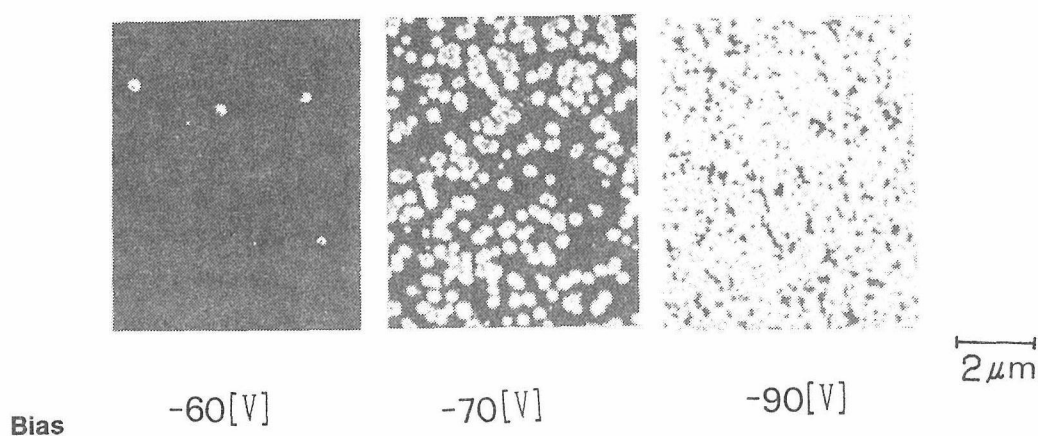
Fig.2 SEM photograghs of grown diamond in 0.5%CH₄/H₂ for 30 min. on the bias-treated
Si substrates in 40%CH₄/H₂ for 2min.
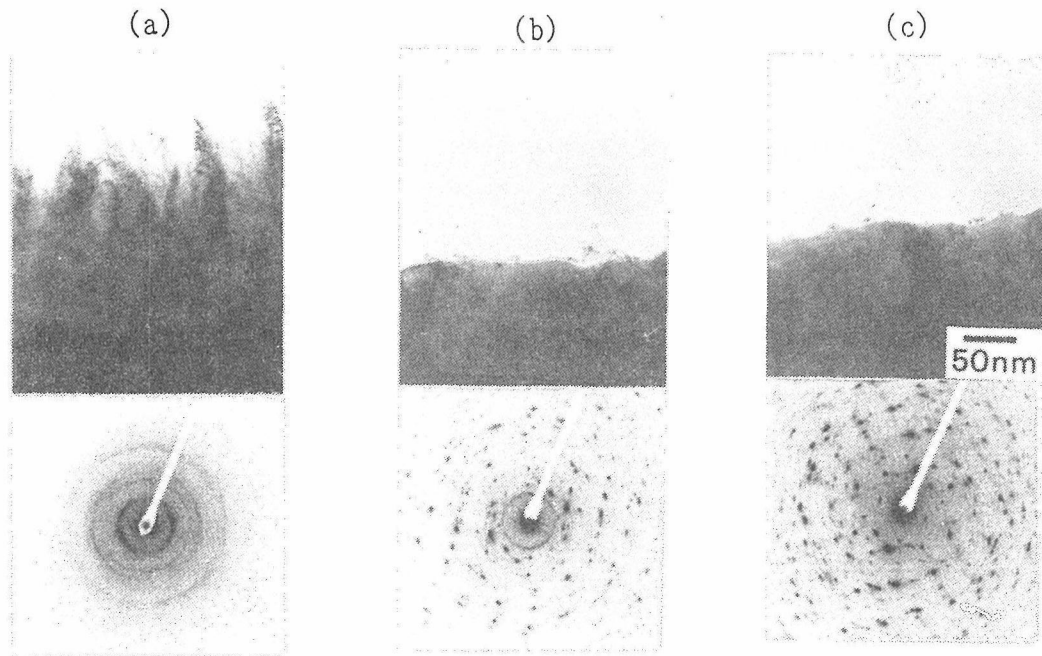
Fig.3 TEM photographs and SAED patterns of growth materials on the Mo meshes,
(a) bias-treatment in 40%CH_4/H_2 at -100V for 5min. (b) after H_2 plasma
etching for 5 min and (c) diamond growth in 0.5%CH_4/H_2 for 3min.

graphite-(002) W-Ring
Si-(111)   Spot
3C-SiC-(110)   W-Spot
diamond-(111)   S-Ring
Si-(220)   W-Spot
diamond-(220)   W-Ring

diamond-(111)
diamond-(220)
diamond-(311)
diamond-(400)
diamond-(331)
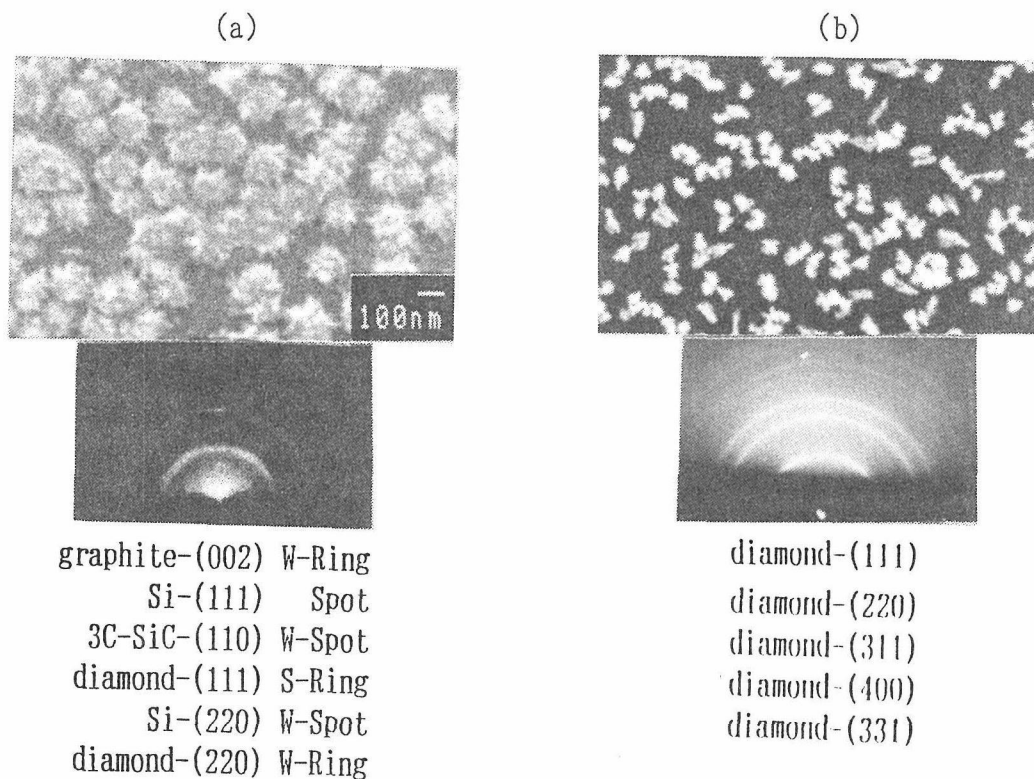
Fig.4 SEM photograpgs and RHEED patterns of growth materials on the Si substrates,
(a) bias-treatment in 40%CH_4/H_2 at -100V for 5min. and (b) after H_2 plasma
etching for 5 min.